

JARNO REUNA

Advanced Functional Antireflection Coatings for Broadband Multijunction Solar Cells

JARNO REUNA

Advanced Functional Antireflection Coatings
for Broadband Multijunction Solar Cells

ACADEMIC DISSERTATION

To be presented, with the permission of
the Faculty of Engineering and Natural Sciences
of Tampere University,
for public discussion in the SA203 S2 auditorium
of the Sähköotalo, Korkeakoulunkatu 3, Tampere,
on 2 December 2022, at 12 o'clock.

ACADEMIC DISSERTATION

Tampere University, Faculty of Engineering and Natural Sciences
Finland

<i>Responsible supervisor or and Custos</i>	Professor Mircea Guina Tampere University Finland	
<i>Supervisor</i>	Doctor Arto Aho Tampere University Finland	
<i>Pre-examiners</i>	Professor Matthieu Roussey University of Eastern Finland Finland	Doctor Guilhem Almuneau LAAS-CNRS France
<i>Opponent</i>	Emeritus Professor Jouko Korppi-Tommola University of Jyväskylä Finland	

The originality of this thesis has been checked using the Turnitin OriginalityCheck service.

Copyright ©2022 Jarno Reuna

Cover design: Roihu Inc.

ISBN 978-952-03-2646-3 (print)

ISBN 978-952-03-2647-0 (pdf)

ISSN 2489-9860 (print)

ISSN 2490-0028 (pdf)

<http://urn.fi/URN:ISBN:978-952-03-2647-0>



ClimateClic CC-000025FI
PunaMusta Printing

Carbon dioxide emissions from printing Tampere University dissertations have been compensated.

PunaMusta Oy – Yliopistopaino
Joensuu 2022

PREFACE

This work was carried out at the Optoelectronics Research Centre (ORC) at Tampere University, former Tampere University of Technology, and was funded by the AMETIST project (ERC #695116). During the years 2017-2022 both the university and ORC have seen quite a few changes and there have been occasional turbulence along the road. Especially the last few years have been globally and personally quite exceptional, but finally the PhD journey that started as a side task along the laboratory upkeep position is now finished by this dissertation.

I would like to express my sincere gratitude to my supervisor Prof. Mircea Guina who provided the opportunity to continue research alongside the cleanroom upkeep duties and for the privilege to work at ORC in the first place. Similarly, I thank my former supervisors at the laboratory side Ilkka Hirvonen, Antti Nuottajärvi, and Dr. Pekka Savolainen for allowing me to venture this path. I would like to thank the seniors of the solar cell team Dr. Antti Tukiainen, Dr. Arto Aho, and Dr. Ville Polojärvi for being the backbone of the team. I thank Dr. Timo Aho, Marianna Vuorinen, and Elina Anttola for processing all the solar cells in the thesis and for the joyful banter along the way. Many thanks for characterizing the final devices and being a great office mate goes to Arttu Hietalahti. I also thank Riku Isoaho for the excellent epitaxy and furthermore being a peer in the same boat. Together with Dr. Eero Koivusalo, and Dr. Marcelo Rizzo Piton you have provided the most enjoyable company both at work and at the extracurricular activities. All in all, there are numerous people who have contributed to the working atmosphere of ORC and made the day-to-day activities that much better, so thanks for each and every one of you! In addition, I thank all the co-authors that made the publications possible. Furthermore, my sincere gratitude goes to the pre-examiners Prof. Matthieu Roussey and Dr. Guilhelm Almuneau for the constructive feedback that made the thesis even better. I also want to thank my opponent Emer. Prof. Jouko Korppi-Tommola for the interest towards the concluded research and providing me an opportunity to publicly defend my work.

Finally, I want to thank my family and especially my wife Susanna for their support and understanding. It is good to know you are there for me.

Valkeakoski, October 31, 2022

Jarno Reuna

ABSTRACT

High efficiency III–V semiconductor multijunction solar cells hold the record of the highest achieved conversion efficiency. Solar cells based on new materials enabling more than 4-junction architectures will most likely push the highest efficiency above 50% within the next decade. To be able to achieve this goal, every aspect of the solar cell structure needs to be designed and fabricated spot on, minimizing any possible optical and electrical losses. To this end, broadband antireflection coatings are instrumental for suppressing the amount of reflected light from the surface of the solar cell. This work contributes to the development of broadband antireflection coatings for primary use in connection with high efficiency multijunction solar cells. As the bandwidth of the utilized solar irradiation is getting increasingly wider, the antireflection coatings based on standard planar structures become harder to optimize, requiring fabrication of more complex films. On the other hand, there is a need to deploy simple and cost effective fabrication techniques to enable economical deployment of new photovoltaic technologies.

This work focuses on developing multilayer antireflection coatings that utilize a nanostructured top layer to surpass the limitations of the conventional planar structures. As a first strand of work, material properties and their relation to the fabrication processes are investigated for low refractive index MgF_2 films deposited by electron beam evaporation and the high refractive index Ta_2O_5 films deposited by ion beam sputtering. The second major part is related to the investigation of a novel technique to fabricate nanostructures with antireflective properties employing a simple de-ionized water treatment. The process is applied to form randomly distributed nanostructures on thin planar amorphous Al_2O_3 layer. A key result introduced in this work is the novel integration of the alumina nanostructuring with an underlying multilayer antireflection coating, specifically aimed to be used in lattice-matched III–V semiconductor multijunction solar cells. The performance of the nanostructured coating was assessed in practical III-V multijunction solar cells, revealing its suitability for practical application. Finally, the stability and durability of the nanostructure has been improved using a hydrophobicity treatment based on fluoropolymerization, and evaluated under atmospheric icing conditions.

TIIVISTELMÄ

Tähänastisesti korkein aurinkokennolla saavutettu hyötysuhde on tuotettu III–V puolijohteisiin perustuvilla korkean hyötysuhteen moniliitoskennoilla. Nämä uusiin materiaaleihin pohjautuvat aurinkokennot mahdollistavat yli neljän kennoliitoksen rakenteet, joilla todennäköisesti ylitetään 50 %:n hyötysuhde vuosikymmenen loppuun mennessä. Tällöin koko aurinkokennon pitää olla loppuun asti optimoitu ja valmistettu, jotta vältetään ylimääräisiltä optisilta ja sähköisiltä häviöiltä. Tavoitteen saavuttaminen vaatii soveltuvia laajakaistaisia heijastuksenestopinnoitteita erilaisille moniliitosrakenteille estämään hyödyllisen auringonvalon heijastuminen kennon pinnalta. Tässä työssä on keskitytty kehittämään heijastuksenestopinnoitteita korkean hyötysuhteen moniliitoskennoille.

Mitä leveämpi kaista auringonvaloa hyödynnetään, sitä vaikeammaksi tasomaisten pinnoitteiden optimointi käy. Halutun pinnoitteen täytyisi laajakaistaisuuden lisäksi olla yksinkertainen valmistaa toistettavasti erilaisille uusille aurinkokennoratkaisuille. Potentiaalisena ratkaisuna vaatimuksille on käyttää tasomaisten kerrosten lisäksi nanokuvioitua pintaa, jota hyödyntämällä voidaan suhteellisen yksinkertaisesti minimoida heijastus laajalta auringonvalon kaistalta.

Työssä tutkittiin pinnoitteiden kerrosmateriaaleina matalan taitekertoimen magnesiumfluoridia ja korkean taitekertoimen tantaalipentoksidia. Näiden lisäksi tutkittiin uuden nanopinnoitusmenetelmän soveltamista monikerroksisiin heijastuksenestopinnoitteisiin. Menetelmässä alumiinioksidikerroksesta muokataan satunnainen nanokuvioitu pinta de-ionisoidussa vesihauteessa. Pinnoitetta käytettiin hilasovitetuille III–V moniliitoskennoille, sen toimivuutta tarkasteltiin normaaleissa käyttöolosuhteissa, ja nanokuvion säilyvyyttä tutkittiin syklisen jäädyttämisen alaisena. Nanorakenteen kestävyuden parantamiseksi testattiin myös hydrofobisuus käsittelyä päällystämällä pinnoite ohuella fluoropolymeeri-kerroksella.

CONTENTS

1	Introduction.....	1
1.1	Scope and Objectives.....	5
1.2	Outline.....	8
2	Coating Design and Fabrication Methods	9
2.1	Broadband Antireflection Coatings	13
2.2	Thin Film Deposition and Processing.....	20
2.2.1	Electron Beam Evaporation.....	20
2.2.2	Rapid Thermal Annealing.....	23
2.2.3	Reactive Ion Beam Sputtering.....	23
2.2.4	Numerical Modeling of Sputtering	25
2.2.5	Nanostructuring Alumina	26
2.2.6	Hydrophobicity Treatment of the Nanostructure	27
2.3	Basics of Multijunction Solar Cells	28
3	Thin Film Characterization	32
3.1	Microscopy.....	32
3.1.1	Atomic Force Microscopy	33
3.1.2	Scanning Electron Microscopy.....	34
3.2	Optical Assessment Techniques	36
3.2.1	Ellipsometry.....	36
3.2.2	Spectrophotometry.....	38
3.2.3	Photoluminescence Spectroscopy.....	39
3.3	Other Characterization Techniques.....	41
3.3.1	Light-biased Current-Voltage Measurements	41
3.3.2	External Quantum Efficiency	44
3.3.3	Icing and Ice Adhesion Tests	46
3.3.4	Contact Angle Measurements.....	47
4	Results and Discussion.....	49
4.1	Annealing Low Refractive Index Magnesium Fluoride	49
4.2	Optimizing Ion Beam Sputtering Process of Ta ₂ O ₅ for III–V Materials.....	58
4.3	Utilizing Nanostructured Alumina Coatings.....	67
4.3.1	Achieving Broadband Antireflection.....	67
4.3.2	Nano-ARC Performance on Multijunction Solar Cells.....	73
4.3.3	Improving Environmental and Temporal Stability	79
5	Summary and Conclusions	88
6	Bibliography.....	92

ABBREVIATIONS AND SYMBOLS

III–V	Elemental Groups III and V
$A\%$	Absorbance
ACA	Advancing Contact Angle
AFM	Atomic force microscopy
ALD	Atomic Layer Deposition
AlGaAs	Aluminum Gallium Arsenide
AlInP	Aluminum Indium Phosphide
Al ₂ O ₃	Aluminum Oxide/Alumina
AM0	Extraterrestrial Irradiation
AM1.5D	Air Mass 1.5 Direct Irradiation
Ar	Argon
ARC	Antireflection Coating
B	Bandwidth
CA	Contact Angle
CAT	Centrifugal Ice Adhesion Test
CVD	Chemical Vapor Deposition
CW	Continuous Wave
D	Refractive Index Contrast
d	Physical Thickness
Δ	Phase Difference Angle
ϵ_i	Dielectric Constant
η	Conversion Efficiency
E_c	Conduction Band Energy
E_g	Bandgap Energy
E_{proj}	Kinetic Energy of Projectile
E_{sca}	Kinetic Energy of Scattered Particle
E_{spu}	Kinetic Energy of Sputtered Particle
E_{th}	Sputtering Threshold
E_v	Valence Band Energy

E-beam	Electron Beam
EMA	Effective Medium Approximation
EQE	External quantum efficiency
f	Multiplier Coefficient
f_i	Volume Fraction
FF	Fill Factor
GaAs	Gallium Arsenide
GaInP	Gallium Indium Phosphide
IBS	Ion Beam Sputtering
IMM	Inverted Metamorphic
IR	Infrared
IWT	Icing Wind Tunnel
J_m	Maximum Current Density
J_{sc}	Short-circuit Current Density
k	Extinction Coefficient
λ	Wavelength
LM	Lattice-matched
LIV	Light-biased Current-Voltage
M	Characteristic Matrix
M_i	Transfer Matrix of i :th Layer
MBE	Molecular beam epitaxy
MgF ₂	Magnesium fluoride
MJSC	Multijunction Solar Cell
ML	Multilayer
n_i	Refractive Index
N ₂	Nitrogen
nano-ARC	Multilayer ARC with the Alumina Nanostructure
NIST	National Institute of Standards and Technology
p	parallel
p	Packing Density
P_{opt}	Optical Power of Incident Light
PL	Photoluminescence
Ψ	Relative Amplitude Change
PVD	Physical Vapor Deposition
QWOT	Quarter Wavelength of Optical Thickness

$R\%$	Reflectance
R_{ave}	Average Roughness
r_i	Reflection Coefficient
R_{rms}	Root Mean Square Roughness
RCA	Receding Contact Angle
RF	Radiofrequency
ρ	Complex Reflectance Ratio
RTA	Rapid Thermal Annealing
s	perpendicular
Si	Silicon
SC	Solar Cell
SCA	Static Contact Angle
SEM	Scanning Electron Microscope
SiO ₂	Silicon dioxide/Silica
T	Total Optical Thickness
$T\%$	Transmittance
T_a	Annealing Temperature
T_s	Deposition Temperature
θ_i	Incidence Angle
Ta	Tantalum
TMM	Transfer Matrix Method
Ta ₂ O ₅	Tantalum pentoxide/Tantala
TiO ₂	Titanium dioxide/Titania
UHV	Ultra High Vacuum
U_{sb}	Surface Binding Energy
UV	Ultraviolet
V_m	Maximum Voltage
V_{oc}	Open-Circuit Voltage

ORIGINAL PUBLICATIONS

- Publication I **J. Reuna**, V. Polojärvi, P. Pääkkönen, K. Lahtonen, M. Raappana, T. Aho, R. Isoaho, A. Aho, M. Valden, and M. Guina, “Influence of ex-situ annealing on the properties of MgF₂ thin films deposited by electron beam evaporation”, *Optical Materials (Amst)*, vol. 96, p. 109326, October 2019, doi: 10.1016/j.optmat.2019.109326.
- Publication II **J. Reuna**, M. Vuorinen, R. Isoaho, A. Aho, S. Mäkelä, A. Hietalahti E. Anttola, A. Tukiainen, M. Guina, “Optimization of Reactive Ion Beam Sputtered Ta₂O₅ for III–V Compounds”, *Thin Solid Films*, (submitted)
- Publication III **J. Reuna**, A. Aho, R. Isoaho, M. Raappana, T. Aho, E. Anttola, A. Hietalahti, A. Tukiainen and M. Guina, “Use of nanostructured alumina thin films in multilayer anti-reflective coatings”, *Nanotechnology*, vol. 32, no. 21, p. 215602, March 2021, doi: 10.1088/1361-6528/abe747.
- Publication IV **J. Reuna**, A. Hietalahti, A. Aho, R. Isoaho, T. Aho, M. Vuorinen, A. Tukiainen, E. Anttola and M. Guina, “Optical Performance Assessment of Nanostructured Alumina Multilayer Antireflective Coatings used in III–V Multijunction Solar Cells”, *ACS Applied Energy Materials*, vol. 5, no. 5, p. 5804-5810, April 2022, doi: <https://doi.org/10.1021/acsaem.2c00133>.
- Publication V **J. Reuna**, R. Kanter, N. Kandelin, K. Kiuru, H. Koivuluoto and M. Guina, “Ice Resistance of Hydrophobic Fluoropolymerized Nanostructured Alumina Films for Antireflective Coatings”, (submitted to focused issue “Nano-Enabled Anti-Icing”, *Nano Express*)

AUTHOR'S CONTRIBUTIONS

The results included in this thesis were obtained as teamwork. The author, Jarno Reuna, conducted the design, growth, and parametrization of the optical coatings, scanning electron microscopy, atomic force microscope mapping, spectroscopic reflectance and transmittance measurements, and the monochromatic ellipsometer measurements. All authors contributed to the writing of the manuscripts. The additional details of the author's contribution in each of the publications are listed below:

[P1] The author was responsible for planning the experiments with Ville Polojärvi and conducting the fabrication and processing of the MgF_2 films. Pertti Pääkkönen measured the dispersion of the films by spectroscopic ellipsometry and analyzed the data. Kimmo Lahtonen made the X-ray photoelectron spectroscopy measurements and the related result analysis. The solar cell designs and growths were done by Arto Aho and Riku Isoaho. Solar cell fabrication was done by Timo Aho and Marianna Raappana. The author was the main person responsible for writing the manuscript, performing calculations, finalizing figures, and interpreting the overall results.

[P2] The author was responsible for planning the experiments together with Arto Aho, Marianna Vuorinen and Riku Isoaho, and conducting the fabrication and processing of the Ta_2O_5 films. The solar cell designs and growths were done by Arto Aho, Riku Isoaho, and Antti Tukiainen. Solar cell fabrication was done by Marianna Vuorinen and Elina Anttola. Photoluminescence was measured by Severi Mäkelä and the light-biased current-voltage by Arttu Hietalahti. The author was the main person responsible for writing the manuscript, performing calculations and simulations, finalizing figures, and interpreting the overall results.

[P3] The author was responsible for planning the experiments together with Arto Aho and Riku Isoaho and conducting the fabrication and processing of the nanostructured Al_2O_3 films. The solar cell designs and growths were done by Arto Aho, Riku Isoaho, and Antti Tukiainen. Solar cell fabrication was done by Marianna

Raappana, Timo Aho, and Elina Anttola. The light-biased current-voltage was measured by Arttu Hietalahti. The author was the main person responsible for writing the manuscript, finalizing figures, and interpreting the overall results.

[P4] The author was responsible for planning the experiments together with Arto Aho and conducting the fabrication and processing of the nanostructured Al_2O_3 coatings. The solar cell designs and growths were done by Arto Aho, Riku Isoaho, and Antti Tukiainen. Solar cell fabrication was done by Marianna Vuorinen, Timo Aho, and Elina Anttola. The external quantum efficiency and the light-biased current-voltage measurements were done by Arttu Hietalahti. The author was the main person responsible for writing the manuscript, performing calculations and simulations, finalizing figures, and interpreting the overall results.

[P5] The author was responsible for planning the experiments together with Mircea Guina, and Heli Koivuluoto, and conducting the fabrication and processing of the nanostructured Al_2O_3 coatings. Raul Kanter and Niklas Kandelin performed the icing and ice adhesion testing. Kaisa Kiuru made the contact angle measurements. The author was the main person responsible for writing the manuscript, finalizing figures, and interpreting the overall results.

1 INTRODUCTION

Antireflection coatings (ARC) have been around for a quite long time [1], [2]. They are key components of every optics system starting from simple eye glass lenses [3] and ranging to industrial lasers [4]–[6], and high-efficient solar cells [7]–[9]. Out of all optical coatings market, that is estimated to reach USD 37.5 billion by 2030, about one third is covered by antireflection coatings [10]. Although ARCs have been around for a while, they are still under active research. A simple Google Scholar search for “antireflection coating”, limited only to the year 2021, yields ~8400 results, so the amount of available information about the topic is vast. In comparison, similar search for “multijunction solar cell” yields only 2780 results. Combining the search phrases shows 1030 results and it is there where this thesis aims to contribute to by developing improved and more practical broadband ARC solutions for the high efficiency III–V multijunction solar cells.

A key material group for the optoelectronics is the III–V compound semiconductors, that can be used both for light-sources, such as lasers [11], [12], and optical receivers, including detectors and solar cells [13]–[16]. The III–V optoelectronics have enabled vast wavelength coverage in lasing wavelengths from ultraviolet (UV) [17]–[19] to infrared (IR) [12], [20], [21] and similarly extended the solar cell efficiencies as high as 47.1% [15] via utilization of a broader spectrum of solar irradiation (270-1770 nm) [14], [22] than the conventional silicon solar cells (270-1100 nm) [23], [24]. Lattice-matched III–V heterostructures grown by molecular beam epitaxy is one of the approaches used to fabricate multijunction solar cells (MJSC) that aim to exceed 50% conversion efficiency [25]–[27]. The high efficiency III–V MJSCs are mainly used in space photovoltaics and terrestrial

concentrator systems [28], [29]. In space the solar cell is capsulated under a cover glass that protects the MJSC from UV light, atomic oxygen, and electron and proton radiation, together with providing thermal and mechanical protection [30], [31]. Similarly, the MJSC is housed behind a concentration lens(es) in concentrated photovoltaics and is not usually in direct contact with the environment [32]. For these applications, the higher fabrication costs are affordable owing to the need for high efficiency and reduced size of active III-V materials when solar concentrators are used. Besides deploying new absorbing heterostructures, these MJSCs require broadband ARC solutions that can maintain their current-balancing requirements and enable as low optical losses as possible [9], [33]–[36].

The term “coating” refers to a thin film structure applied on a surface. Similarly, the item with the target surface is called a substrate. **Figure 1** presents an illustration of a coating on a substrate together with two common substrates for ARCs.

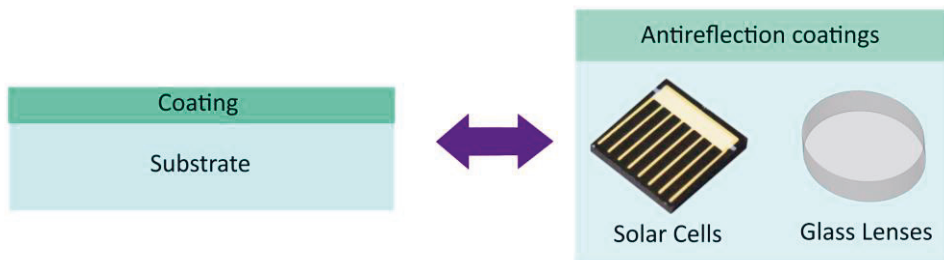


Figure 1 A coating is an overlaying thin film structure applied on a substrate. Typical substrates for antireflection coatings include solar cells and glass lenses.

From the perspective of ARCs, the key distinction between solar cells and glass is the atomic structure of these solids. Glasses are mostly amorphous materials, whereas most of the semiconductor solar cells are crystalline with a periodic order of the constituent atoms. Glasses are also chemically an inert material group, but the semiconductor surfaces readily react with the surrounding atmospheric oxygen and moisture [37]–[39] that alters their properties in unwanted ways. For glass substrates,

the functionality is conventionally provided by the refractive index of the material and the shape of the component, for example concave or convex lenses, but with the semiconductors the electronic properties defined by the atomic structure play a major part of the device performance. Therefore, applying antireflection coatings using established coating methods optimized for glass onto the III–V optoelectronics is not a trivial task.

Antireflection coatings are usually made out of transparent, dielectric materials, such as trans-metal oxides [40]–[43]. In this work, I have focused on materials deposited by physical vapor deposition (PVD), regularly used for coating optoelectronics as well as glasses. The advantages of these materials are the high transparency and the wide selection of available refractive indices [40], [42]. The challenge, and the focus of this thesis, lies in finding the optimal procedures, materials, and coating parameters for achieving seamless functionality for both the underlying semiconductor MJSC and the antireflection coating on top of it. **Figure 2** a) shows how optimal process conditions provide repeatable and uniform antireflection coatings, whereas b) and c) demonstrate the challenges of coating III–V materials.

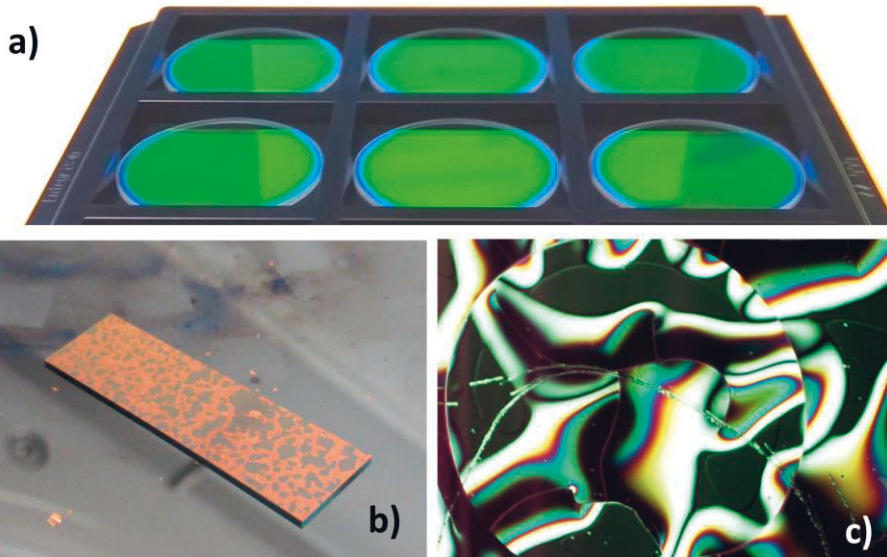


Figure 2 a) Uniform ARCs on glass substrates without any visible flaws. b) A thermal processed coating on a semiconductor slab that flakes off. c) A top view of a shattered mirror coating broken by the strain in the structure.

In the published reports of the high efficiency III–V MJSCs [15], [44]–[47] the focus usually lies in the MJSC structure and materials, so the development, fabrication methods, and constituents of the used ARC are sometimes neglected. All the record efficiency III–V MJSCs, out of those that mention the ARC at all, use planar coatings, and the most frequently used high and low refractive index material pair is MgF_2 and ZnS [15], [45], [46], [48]. Despite the fact that the optimal utilization of the solar spectrum would require going beyond the typical two-layer ARC structure [9], [33]–[36], it is still the most common approach due to its simplicity and established fabrication procedures [16], [33], [47]–[49]. Ongoing research addresses the use of both multilayer (ML) ARCs [50]–[52] as well as nanostructure based approaches for MJSC ARCs [53]–[60], but amongst the publications reporting the highest efficiencies there are only a few mentions about four-layer MgF_2/ZnS -ARCs [15], [61]. Therefore, the need for developing practical and efficient ML ARC fabrication approaches matching the ever-increasing requirements for broadband

operation and simplicity is evident. Thus, the generic requirements for such an ARC can be divided into two subgroups:

1. **Functionality:** The ARC needs to be easily **repeatable**, so that each deposition run provides the same good results. It needs to provide the needed **broadband low reflectance**. The deposition process for the ARC should be **unharmful for the MJSC** itself, as the gain by reducing optical losses can be easily mitigated by generating additional electrical losses. And lastly, it should **provide current-matched operation** for the MJSC in question. In practical sense, it needs to match with the specific MJSC and that there is no possibility of drifting of the reflectance minima.
2. **Durability:** The ARC should remain ideally the same from the moment it is deposited to the end of the life cycle of the solar cell. The **temporal stability** is easy to overlook, but with some materials and designs the change due to time in performance can be significant. In addition to time, the ARC should be able to **withstand the environment** it is used in. And finally, no matter how good the ARC optically is, it needs to stick on the substrate. Peeled-off coatings, as in **Figure 1 b)** and c), are the worst kind of failure in any deposition process. So, the ARC needs to have **good adhesion** to the sample.

With the laid-out requirements we can set the scope and objectives for the thesis.

1.1 Scope and Objectives

The scope and the main objective of the thesis is to progress the development of ARCs used for broadband MJSCs. **Figure 3** presents the direction lines of the thesis, starting from known ARCs [15], [61], i.e. the ARC structure we have previously used (status quo). The ultimate target of the thesis is to have a working broadband ML ARC with a nanostructured top layer that can be utilized on III–V MJSCs.

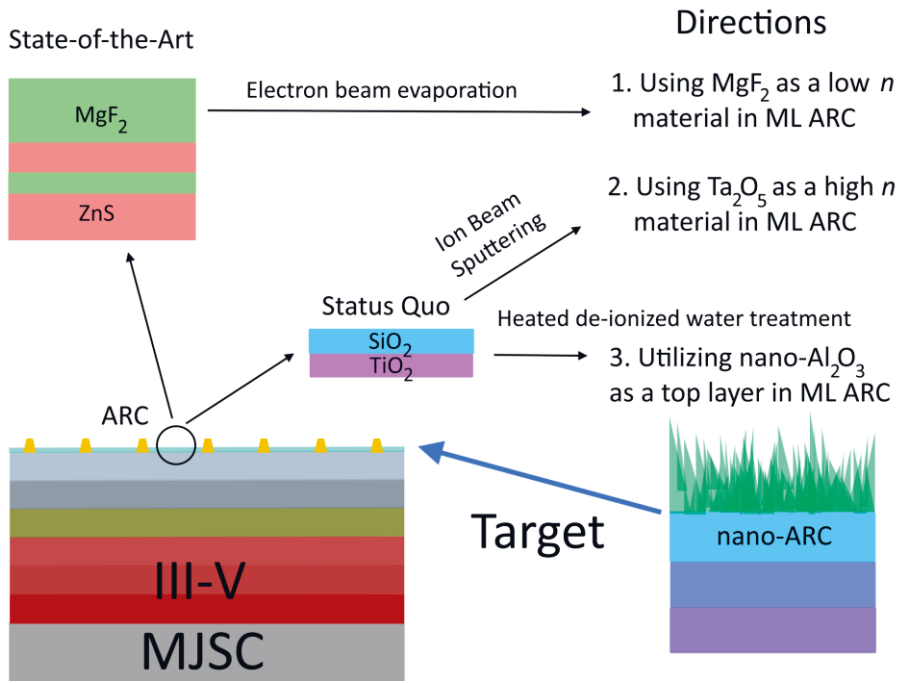


Figure 3 Starting point of the ARC development together with the research objectives, and the final target of utilizing a ML ARC with nanostructure on top for the III–V MJSCs.

The five publications included in this thesis have aimed to contribute to the development of a practical and efficient ML ARC for MJSCs by looking into the material properties of MgF₂ and Ta₂O₅, their processing requirements, and investigating nanostructured Al₂O₃ integrated into a new kind of ML ARC (nano-ARC).

Table 1 summarizes the research questions for each of the publications and the specific aspects that were considered in the studies.

Table 1 Research questions for the articles (P1-P5) included in the thesis and the key aspects studied for each publication

Research Question		Aspects
P1	Could post-deposition annealing for electron beam evaporated MgF_2 be beneficial when using MgF_2 as a low refractive index material for MJSC ARC?	<ul style="list-style-type: none"> • Process parameters • Material properties • Temporal stability • Influence of post-deposition thermal treatment
P2	Can reactive ion beam sputtered Ta_2O_5 be successfully utilized as a high refractive index material for MJSC ARC?	<ul style="list-style-type: none"> • Process parameters • Material properties • Understanding the physics of sputtering • Influence on MJSC performance
P3	Can nanostructuring process of Al_2O_3 be used with electron beam evaporated and ion beam sputtered materials to achieve broadband ML ARCs?	<ul style="list-style-type: none"> • Process comparison of electron beam evaporated, and ion beam sputtered oxides • Properties of the nanostructured Al_2O_3 • Proof-of-concept ML ARCs
P4	How does the nano-ARC perform on III–V MJSC?	<ul style="list-style-type: none"> • Angle-dependent properties, EQE • Electrical properties of the MJSC, LIV • Reflectance reduction in contrast to the current-balance and subjunction bandwidths
P5	How can the nano-ARC endure harsh conditions?	<ul style="list-style-type: none"> • Atmospheric icing • Hydrophobicity treatment • Durability and performance

The next subchapter presents the structure for the rest of the thesis and how the background and the results of the publications are addressed in this work.

1.2 Outline

The 2nd chapter of this thesis will introduce the basic concepts and requirements for designing and fabricating an ARC for a MJSC. The chapter goes through the thin film fabrication methods used in the study. The 3rd chapter presents a selection of characterization methods important for assessing the quality of the coatings. The 4th chapter will introduce the key results of the thesis and is divided into three sub-chapters, as one for annealing low refractive index MgF_2 , the second for reactive ion beam sputtering of high refractive index Ta_2O_5 , and the third for the nanostructured Al_2O_3 ML ARCs. The 5th and the final chapter summarizes the work of the thesis and presents a development outlook for future work.

2 COATING DESIGN AND FABRICATION METHODS

It all starts with a design. Fortunately, the long history of optical coatings provides numerous tools and tips to use for designing an antireflection coating [62]–[66].

A basic starting point for any coating optimization is usually a quarter wavelength optically thick (QWOT) layer, that equals a physical thickness of:

$$\text{QWOT} = \frac{\lambda}{4 n_{\text{film}}} \quad (1)$$

in which λ is the wavelength in consideration and n_{film} is the refractive index of the material at that wavelength. At the design wavelength QWOT layer produces the strongest interference effect. Adding another QWOT of the same material leads to a half wavelength optically thick layer which returns the intensity back to its original value at the given wavelength. As it is rarely enough to consider just a single wavelength or to be able to reach your target value with just one layer, QWOT offers just a reasonable starting point for a design optimization. The thin film interference principle on a substrate is elaborated in **Figure 4**.

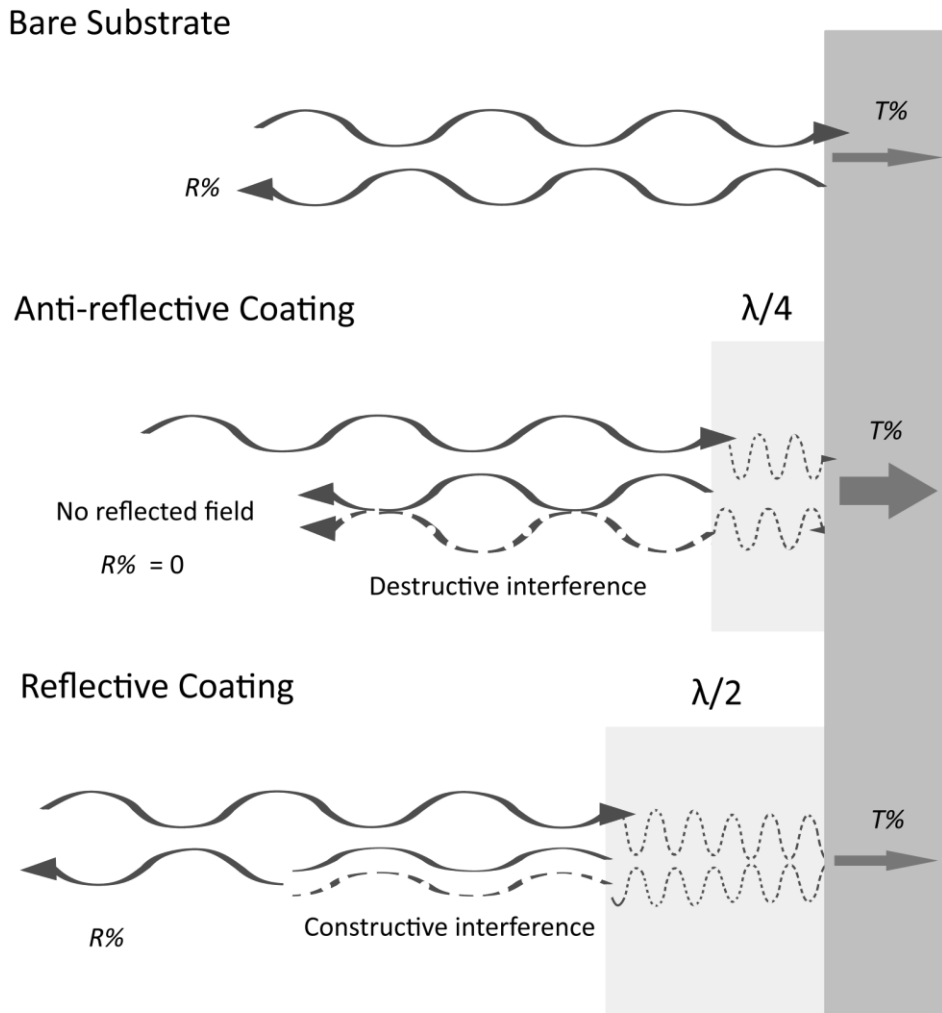


Figure 4 The interference principle of having an optimal QWOT ARC on a substrate or a half wavelength optically thick layer.

The optimal refractive index for a single-layer ARC for a certain wavelength on any known substrate with air/vacuum ($n_{\text{air}} \approx 1$) as an incident medium can be calculated as:

$$n_{\text{film}} = \sqrt{n_{\text{air}} n_{\text{substrate}}}. \quad (2)$$

The optimal layer thickness would be a QWOT at that wavelength. Eq. 2 does not usually yield a realistic solution, as the refractive index of the thin film is limited by the availability of materials. For example, matching the refractive index of glass to air requires a material with $n_{\text{film}} = 1.22$ which cannot be matched with the conventional homogeneous dielectric materials. Nowadays, as glass is one of the most abundant substrate material and air is the most common incident medium, there are available workarounds such as nanostructured layers [67], [68] and metamaterials [69]. Nevertheless, when designing ARCs, one should keep in mind that the material properties cannot usually be arbitrarily selected and optimize the design within the limits of practicality.

The logical next step for a design improvement after considering a single-layer design is to add another layer material and see where that gets you. How to appropriately choose the layer materials for an optimal 2-layer ARC can be broken down into a few ground rules that will also apply to ML ARCs. Optimizing ARCs for variable substrates and bandwidths has a long history that gives useful limitations and considerations to take into account [7], [9], [52], [70], [71] and have been narrowed down by Ronald Willey and his team [66] into an experimentally fitted equation for the minimum achievable average reflection as a function of the bandwidth (B), the lowest refractive index (n_L) used in the design, the optical thickness of the complete coating (T), and the difference between the highest and the lowest refractive index (D) which can also be called the refractive index contrast:

$$R_{\text{ave}}(B, n_L, T, D) = \frac{4.378}{D} T^{-0.31} [e^{(B-1.4)} - 1] (n_L - 1)^{3.5}. \quad (3)$$

The bandwidth is calculated here as the ratio of the limiting longest and shortest wavelengths, as $B = \frac{\lambda_{\text{long}}}{\lambda_{\text{short}}}$. As the optical thickness, and refractive indices, due to the dispersion, are dependent on the wavelength, these values are calculated at the geometric mean of the bandwidth ($\lambda_{\text{mean}} = \sqrt{\lambda_{\text{long}} \lambda_{\text{short}}}$). The optical thickness T is defined as:

$$T(\lambda) = \frac{d \cdot n(\lambda)}{\lambda}, \quad (4)$$

where d is the physical thickness of a layer and $n(\lambda)$ is its refractive index at the design wavelength λ . To get the total optical thickness of a coating, one needs to sum up all the individual optical thicknesses of the layers in the design. Eq. 3 is an experimental derivation that does not provide an exact solution for any certain case of an ARC optimization. However, it is extremely useful in presenting the relations between the chosen materials and the design targets and helps to quantify the key rules of an ARC design. For instance, it is seen that the refractive index of the lowest index material is proportional to the average minimum reflectance, so that the closer the value is to 1, the smaller the average reflectance. Similarly, if the bandwidth increases, so does the minimum achievable average reflectance. On the other hand, the minimum average reflectance decreases as the contrast increases. Only the quantity T , the total optical thickness, is not as straightforwardly interpreted as it seems in Eq. 3. There it shows that the thicker the ARC the smaller the minimum average reflectance. Mathematically that holds true, but such designs might not be practical or even manufacturable in some cases. Main issues rise from the arbitrarily thin layers and the large total number of layers required to achieve the calculational minimum average reflection. Too thick coatings may also increase fabrication costs, while simultaneously decrease the yield of acceptable coating runs and generally result in poor long-term stability and delamination issues. So, the rule of thumb for thickness is to keep the design simple. From these principles the ground rules for searching an optimal ARC can be listed as:

- I. The low refractive index material should have as close refractive index to air as possible.
- II. The refractive index contrast between the highest and the lowest index materials should be as high as possible.
- III. The bandwidth for the ARC should not be any wider than strictly necessary.
- IV. The total thickness should be kept within reasonable limits.

Additionally, the used materials should exhibit little to no absorption within the bandwidth of interest when it is as important to have high transmittance through the coating as it is to reduce the reflectivity. Rule IV is not so precisely limiting, but thinner and simpler usually produces better results. Eq. 3 does not mention anything about the number of layers or the effect of the substrate refractive index. Namely, because mathematically they do not matter. In practice, one should also consider the substrate refractive index when choosing a starting layer material for an ARC. Too close refractive index does not produce enough index contrast in the first interface and too large does the opposite. Unless a fully graded-index profile from $n_{\text{substrate}}$ to n_{air} is possible, this also plays a role in the overall design quality. Moreover, the probability of observing long term degradation and delamination issues increases with the number of layers owing to different thermal expansion coefficients between different materials and surface strain.

2.1 Broadband Antireflection Coatings

For solar cells a single-layer ARC is mostly an outdated solution, but due to its simplicity and passivation properties, single-layer SiN_x ARCs can still be seen both in experimental research as well as in commercial silicon solar cells [72]–[76]. The bandwidth of a single-layer ARC is quite limited as is shown in **Figure 5 a)** for a simulated SiN_x ARC on silicon. For MJSCs that narrow bandwidth would not suffice and even the simplest MJSC ARCs are made of double-layer structures. The basic high refractive and low refractive index material pair can have two effective ARC constructions: a V-ARC and a W-ARC [62]. The letters V and W refer to the shape of the reflectance band as is demonstrated in **Figure 5 b)**, that shows two simulated $\text{TiO}_2/\text{SiO}_2$ ARCs on GaAs. Out of these two structures, the V-ARC has lower reflectance at the design wavelength, but the W-ARC has a wider bandwidth with its double minima and is thus more suitable for MJSC applications.

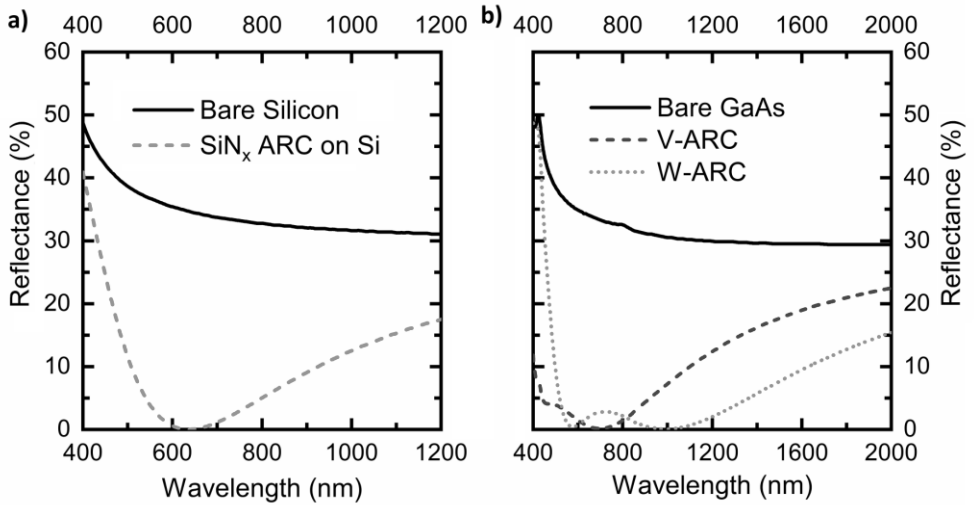


Figure 5 a) Simulated reflectance of silicon and a single-layer silicon nitride (SiN_x) ARC on silicon. b) Simulated reflectance of bare GaAs, and GaAs with 2-layer $\text{TiO}_2/\text{SiO}_2$ V- and W-ARCs.

From **Figure 5 b)** is seen that the $\text{TiO}_2/\text{SiO}_2$ W-ARC is already a good starting point for a III–V MJSC ARC, having a suitably low reflectance with a bandwidth of 500 nm to 1200 nm. For that reason it has been the standard solution used in our prior works [16], [77]–[79] and presents a benchmark for the comparison of the developed ML ARCs. Using Eq. 3 we can calculate for that bandwidth the minimum achievable average reflectance for $\text{TiO}_2/\text{SiO}_2$ ARC which is 0.63%. By switching silica to lower refractive index MgF_2 the minimum average reflectance could be lowered to 0.32%. Similar calculation for Ta_2O_5 and MgF_2 ARC shows achievable average minimum reflectance as low as 0.44%. Additionally, tantalum has lower absorption at the UV range than TiO_2 [80], [81]. In these calculations the optical thickness was fixed to $T = 0.5$. Eq. 3 shows the potential for the material combinations, but reaching the minimum average reflectance requires optimal multilayer structures that should be numerically evaluated during the design phase. If we expand the bandwidth to 300–1800 nm range, which the most developed MJSC

architectures utilize, we quickly notice that the achievable average minimum reflectance rises quite high, even if we raise the optical thickness to $T = 2.5$ (equals 5 high/low refractive index QWOT layer pairs). The corresponding reflectance values for the material pairs $\text{TiO}_2/\text{SiO}_2$, $\text{TiO}_2/\text{MgF}_2$, and $\text{Ta}_2\text{O}_5/\text{MgF}_2$ are 21.7%, 11.1%, and 15.1%, respectively. Although the high reflectance at the edges of the defined bandwidth, as is seen in **Figure 5 b)**, raise the average reflectance without necessarily affecting the current balancing of the MJSC, it is clear that the higher achievable average minimum reflectance values indicate that the planar layer designs will not fulfill the more advanced needs for MJSC ARCs required to operate from UV to beyond 1600 nm.

In terms of design tools, evaluating the complete thin film coating performance is commonly done using a transfer matrix method (TMM) [82]–[84] by calculating the reflectance and transmittance of the coating over the relevant bandwidth. In the case, where all the light comes from the direction of the incidence medium, i.e. no incoming light from the substrate side, the TMM can be written as:

$$\begin{bmatrix} 1 \\ r \end{bmatrix} = \mathbf{M} \begin{bmatrix} t \\ 0 \end{bmatrix} \quad (5)$$

in which the \mathbf{M} is the characterization matrix of the multilayer structure, r the reflection coefficient, and t the transmission coefficient. For single interfaces the coefficients can be written for s-polarization as:

$$r_{i,i+1} = \frac{n_i \cos \theta_i - n_{i+1} \cos \theta_{i+1}}{n_i \cos \theta_i + n_{i+1} \cos \theta_{i+1}}, \quad t_{i,i+1} = \frac{2n_i \cos \theta_i}{n_i \cos \theta_i + n_{i+1} \cos \theta_{i+1}}, \quad (6)$$

and for p-polarization as

$$r_{i,i+1} = \frac{n_{i+1} \cos \theta_i - n_i \cos \theta_{i+1}}{n_{i+1} \cos \theta_i + n_i \cos \theta_{i+1}}, \quad t_{i,i+1} = \frac{2n_i \cos \theta_i}{n_{i+1} \cos \theta_i + n_i \cos \theta_{i+1}} \quad (7)$$

where θ_i is the incidence angle. \mathbf{M} is calculated as:

$$\mathbf{M} = \frac{1}{t_{0,1}} \begin{bmatrix} 1 & r_{0,1} \\ r_{0,1} & 1 \end{bmatrix} M_1 M_2 \dots M_{N-2} = \begin{bmatrix} \mathbf{M}_{00} & \mathbf{M}_{01} \\ \mathbf{M}_{10} & \mathbf{M}_{11} \end{bmatrix}, \quad (8)$$

where the suffixes indicate the layers for a total number of considered layers N (including the incidence medium = 0, and the substrate = $N-1$) and M_i is a transfer matrix of a layer i . M_i can be written as:

$$M_i = \begin{bmatrix} e^{-j\delta_i} & 0 \\ 0 & e^{j\delta_i} \end{bmatrix} \begin{bmatrix} 1 & r_{i,i+1} \\ r_{i,i+1} & 1 \end{bmatrix} \frac{1}{t_{i,i+1}}, \quad (9)$$

in which $\delta_i = \frac{2\pi}{\lambda} n_i d$ corresponding to a phase change of a layer with the thickness of d . For an arbitrary multilayer film structure, the r and t in Eq. 5 can be calculated as:

$$r = \frac{M_{10}}{M_{00}}, \quad \text{and} \quad t = \frac{1}{M_{00}}, \quad (10)$$

from where the reflectance and transmittance can be calculated as

$$R\% = |r|^2 \quad \text{and} \quad T\% = \frac{n_2 \cos \theta_2}{n_1 \cos \theta_1} |t|^2. \quad (11)$$

Although coding your own TMM script for basic coating calculations is not too hard, it is not strictly necessary as there are plenty of available software for the purpose. These include commercial programs like EssentialMacLeod [85], FilmStar [86], and OptiLayer [87], several freeware Python packages [88], [89], and a full free program OpenFilters [90]. They utilize effective optimization algorithms that combined with the ground rules of ARC design yield usually good results.

In the case of MJSC, where the aim is to convert as much solar irradiation to electrical power as possible, broadband can be defined as everything between 300 nm and the narrowest bandgap of the MJSC structure, which in theory extends up to 1800 nm with the germanium bandgap (0.7 eV). In practice, the infrared (IR) limit for the broadband ARC depends on the material combination used in the junction stack and, more importantly, needs to be matched to the overall design of the MJSC

to yield the highest performance. **Figure 6** presents a spectrum division for a possible 5-junction GaInP/GaAs/GaInNAsSb/GaInNAsSb/GaInNAsSb MJSC structure where the utilizable spectrum spans from 300 nm to the 1800 nm with the bandgaps of 1.9 eV/1.4 eV/1.2 eV/0.9 eV/0.7 eV, respectively. The extraterrestrial solar spectrum AM0 (ASTM E-490) and the direct illumination solar spectrum AM1.5D (ASTM G-173-03) [91] are both presented. AM0 is the standard used for space photovoltaics and AM1.5D is used for comparing the performance of III–V concentrator solar cell materials, because only direct sunlight can be efficiently concentrated.

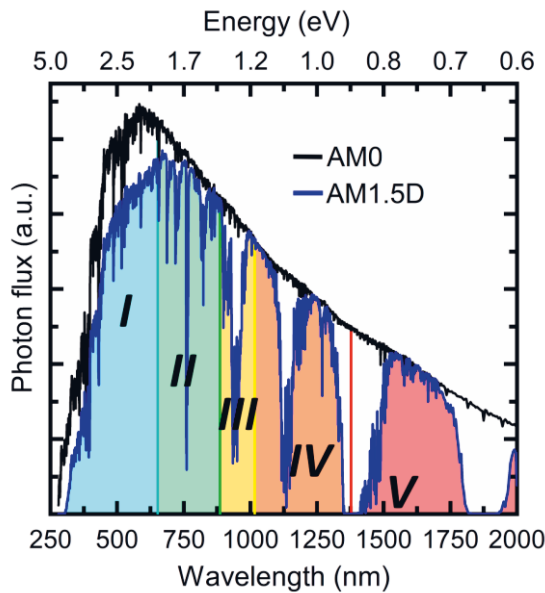


Figure 6 The solar spectra for AM0 and AM1.5D standards [91] divided into five hypothetical bandwidths of a MJSC design, as I to V referring to the subcells of the stack. [Adapted from P3]

Using only planar layers for reflectance reduction has its limits as it was shown using the average reflectance calculations with Eq. 3. As the utilizable spectrum spans over the 300-1800 nm bandwidth, it is essential to develop ARC that can cover the whole

range. To tackle the issue different types of nanostructured ARCs have been developed and tested on MJSCs [53]–[60], but they typically come with their drawbacks. Patterned semiconductor window layer causes additional losses in the UV region due to increased thickness of the window [55]–[57], direct patterning of the solar cell structure can cause increased recombination losses [58] and with patterned dielectric structure the refractive index contrast between the high index semiconductor material and the low index ARC is too large for efficient reduction of reflectance [53], [54]. Multilayer dielectric coatings combined with patterning [9], [59], [60] have so far been an effective but laborious solution due to multi-step fabrication processes required for the patterning. The approach chosen for this thesis is to combine a nanostructured alumina top layer with an underlying planar ML ARC. The method is simple, non-toxic, and low-cost and it is based on post-deposition treatment of planar amorphous alumina coatings with heated de-ionized water (DIW) [92], [93]. In addition, there is no need for lithography and surface etching for patterning. Thanks to its simplicity concerning the processing steps, the method is more suitable than the similar kind of hybrid broadband ARCs [59], [60] for real-life applications. The properties of the nanopattern can be controlled via film thickness and DIW treatment time [94] and the hydrophobicity of the film can be increased with post-process polymerization [95].

The main principle of using nanostructures as an antireflection coating is to have a gradual change in the refractive index between the substrate and the incident medium which is illustrated in **Figure 7**.

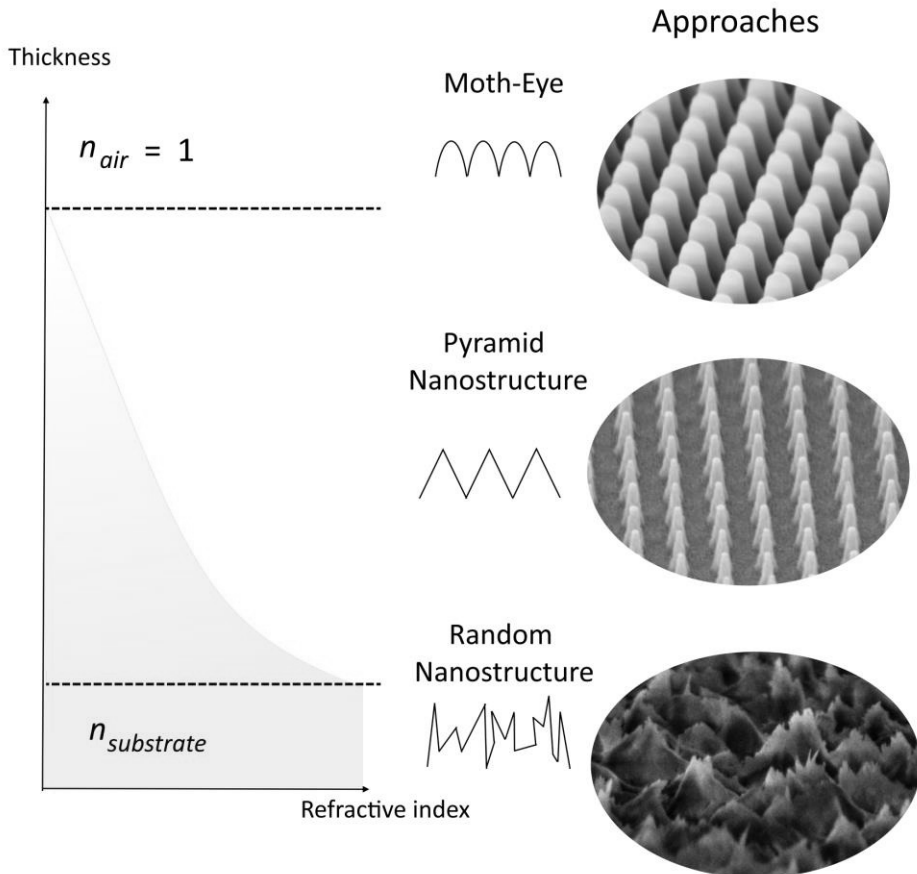


Figure 7 Utilizing a nanostructured surface in ARCs is based on the concept of gradual refractive index change from the refractive index of the substrate to the incidence medium refractive index. Different kinds of applied nanostructures include bio-inspired moth-eyes, pyramid-like nanostructures, and randomly distributed nanostructures. [Original moth-eye and pyramid SEM images by the courtesy of Dr. Juha Tommila]

Different kind of nanostructured ARC approaches include bio-inspired moth-eye structures [77], [96], [97], pyramid and nanocone structures [57], [98], [99], and random nanostructures [92], [100]. Our nanostructured alumina approach represents

the random structures that does not include any subwavelength periodicity like the other methods.

2.2 Thin Film Deposition and Processing

ARCs are fabricated using thin film deposition techniques. Generally, the two main classes of thin film deposition are divided into physical vapor deposition and chemical vapor deposition (CVD). In PVD the film constituents are produced into atomic/molecular state by heating or particle collisions and after traveling in vacuum the material forms a film on the substrate. In CVD there is usually at least two precursor gases that react on the substrate surface and form the film material as a reaction product. This work focuses on PVD and more precisely on electron beam (E-beam) evaporation and ion beam sputtering (IBS).

2.2.1 Electron Beam Evaporation

E-beam evaporation is based on melting the target material with current provided by an electron beam. The melted material emits its constituents, which in vacuum travel to the substrate, condense on the surface, and form a film. The electrons of the beam are generated with a tungsten filament and accelerated with a few kilovolts range voltage, which together with a magnetic field is used to guide the beam into a liner holding the raw material being evaporated. **Figure 8 a)** shows the glowing filament that in vacuum emits the electrons and **Figure 8 b)** presents variable materials that were used in the ARC development.

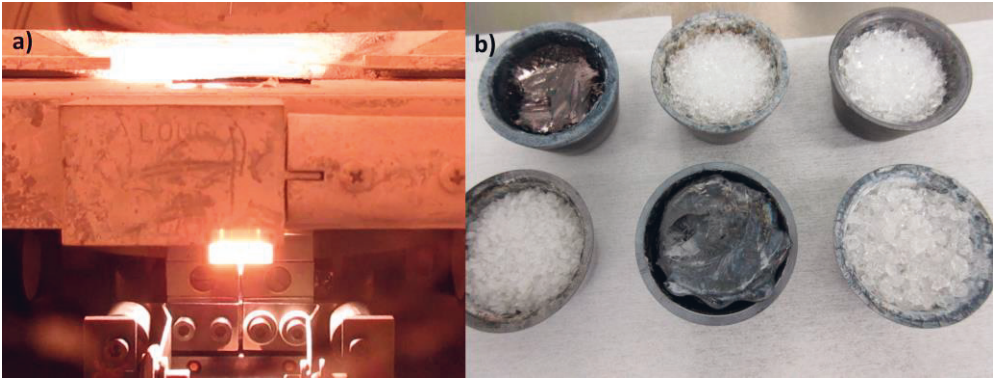


Figure 8 a) The tungsten filament of the electron source is producing the electron beam that is directed to the material cup above. b) A selection of e-beam evaporation starting materials used for thin film deposition. Starting from top left: TiO_2 , $2 \times \text{SiO}_2$, MgF_2 , Ta_2O_5 , and Al_2O_3 .

E-beam can be used to evaporate both metals and dielectrics. Metals usually require lower base pressure, but no additional heating. Dielectric materials can be evaporated in higher pressure range and often require additional background oxygen for reactive evaporation of oxides. They also require additional heating for the substrate, so that the forming film gets dense and forms necessary bonds to the substrate surface for good adhesion of the film. As dielectrics are insulators, the electron beam is not heating the raw material evenly and the material is usually subliming before melting. Due to these process properties (substrate heating, background pressure, uneven melting), evaporation of good quality dielectric films requires understanding of the overall material specific process and strict enough process control. The system used in the thesis has limited heating capacity ($< 250 \text{ }^\circ\text{C}$), relatively high base pressure of 1×10^{-5} mbar and is manually adjusted and controlled. For film thickness control the system uses a quartz crystal oscillator.

For MgF_2 studied in P1, we have assumed porous structure [101], [102]. As these pores can be filled either with air or water, depending on the humidity and exposure conditions, we utilized effective medium approximation (EMA) [103] to describe the

measured refractive indices of the annealed MgF₂ films. From EMA the ratios of air/MgF₂ in the films can be calculated when we assume that:

- 1) The pores contain only air right after the annealing procedure ($f_{\text{MgF}_2} + f_{\text{air}} = 1$).
- 2) The MgF₂ skeleton has a refractive index of the bulk material $n_{\text{MgF}_2} = 1.378$ [104].
- 3) The films are transparent, so the dielectric constant follows equation $\epsilon = n^2$.

The volume fractions (f_i) of the film constituents are given by EMA as:

$$f_{\text{MgF}_2} \frac{(\epsilon_{\text{eff}} - \epsilon_{\text{MgF}_2})}{(\epsilon_{\text{eff}} + \epsilon_{\text{MgF}_2})} + f_{\text{air}} \frac{(\epsilon_{\text{eff}} - \epsilon_{\text{air}})}{(\epsilon_{\text{eff}} + \epsilon_{\text{air}})} = 0 \quad (12)$$

which can be written as

$$f_{\text{air}}/f_{\text{MgF}_2} = - \left(\frac{(\epsilon_{\text{eff}} - \epsilon_{\text{MgF}_2})}{(\epsilon_{\text{eff}} + \epsilon_{\text{MgF}_2})} \right) / \left(\frac{(\epsilon_{\text{eff}} - \epsilon_{\text{air}})}{(\epsilon_{\text{eff}} + \epsilon_{\text{air}})} \right). \quad (13)$$

The dielectric constant ϵ_{eff} is the effective dielectric constant of the deposited film, ϵ_{MgF_2} is the MgF₂ bulk value, and ϵ_{air} is the dielectric constant of air. The fraction of pores in the film is given by Eq. 13 and can be used to calculate the packing density p of the MgF₂ film, as:

$$p = 1 - (f_{\text{air}}/f_{\text{MgF}_2}). \quad (14)$$

As packing density is a figure of merit for how densely the actual film material is constructed, the closer the value is 1 the better. Higher packing density indicates less porosity which straightforwardly reduces effects caused by adsorbed humidity in the films.

E-beam evaporation was used for thin film deposition in the publications P1 & P3 and the work was done by using a custom-built evaporator by Instrumentti Mattila Oy; having an electron source, a crucible, and sweep controls from Telemark Ltd, and a quartz monitoring from Intellemetrics Global Ltd.

2.2.2 Rapid Thermal Annealing

Aiming at reducing the porosity of the evaporated MgF_2 films, post-deposition annealing was done by using a rapid thermal annealing (RTA) process. In the annealing process the sample is exposed to heat to induce beneficial changes in the material, such as re-ordering of the atoms and removal of impurities. The test series in P1 utilized annealing temperatures (T_a) from 300 °C to 1000 °C with 100 °C intervals. Inert N_2 atmosphere was used during temperature ramping and a one-minute-long annealing at the constant temperature was performed in a vacuum. The RTA system used in this work was a JetFirst 100 from Jipelec Ltd.

2.2.3 Reactive Ion Beam Sputtering

Sputtering refers to a process where a kinetic particle, a projectile, knocks-out another particle from a solid. Commonly used projectiles are noble gas ions, such as argon, xenon, and neon, that are accelerated with an electric field to a target. In the IBS system used in this thesis, the projectiles include both argon and oxygen ions and the sputtered target materials are metallic. The ions are generated with alternating radiofrequency (RF) coil and accelerated and guided by three-gridded beam optics. To get transparent oxides out of the metallic targets, the system has a reactive oxygen atmosphere in addition to the oxygen fraction in the ion beam. Due to the oxidation process taking place at the targets and at the metallic sputtered species, the process is called reactive ion beam sputtering. **Figure 9** shows a simplified overview of the sputtering process of Ta_2O_5 . The sputtered oxide particles

form the film on the substrate and the process is optically monitored through a monitoring glass sample.

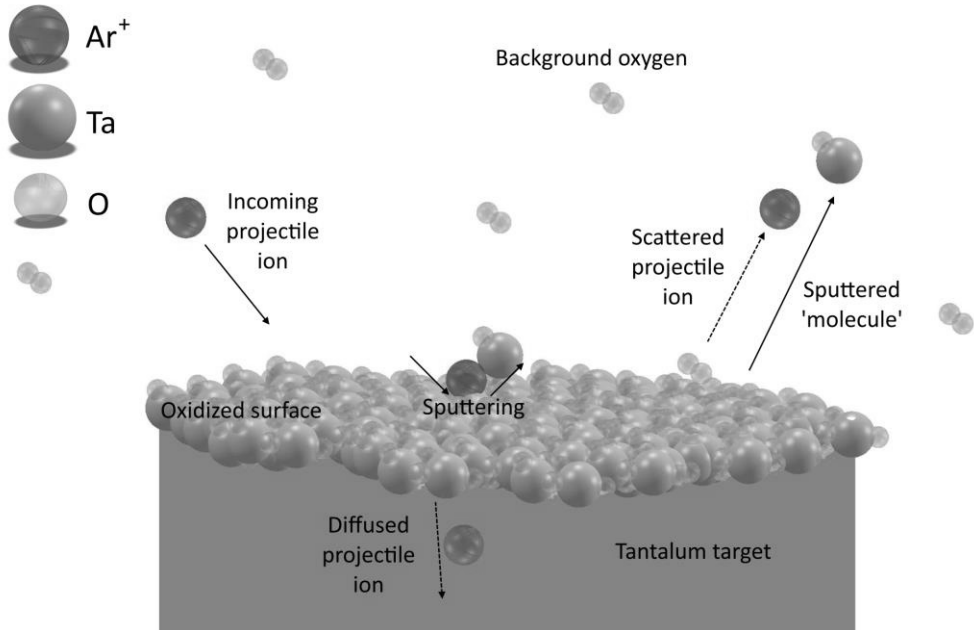


Figure 9 Ion beam sputtering utilizes a beam of accelerated ions to knock-out target particles which will then form the thin film on samples. In reactive IBS deposition, there is also a reactive background atmosphere, which is usually oxygen. Here is a schematic illustration of the process of sputtering Ta_2O_5 [P2].

IBS is known to produce high quality optical thin films with high laser damage threshold and environmentally stable optical constants [4], [105]. The high quality of the deposited films, even at the room temperature, is due to the energetics of the sputtering process [106]–[108]. The method is well established for coating optical filters on top of glass substrates [109] and due to its proven quality should provide excellent ARC deposition method for III–V MJSCs, which can fulfill the stability and reproducibility requirements.

Reactive ion beam sputtering was the main deposition method used in the publications P2-P5. The system used in this work was a Navigator 700 sputtering system from Cutting Edge Coatings GmbH.

2.2.4 Numerical Modeling of Sputtering

During the test growths of IBS deposited Ta_2O_5 , it became evident that the energetic process of reactive ion beam sputtering was not straightforwardly suitable for coating III–V materials. We noticed severe device degradation due to the coating which seemed to be linked mainly to the coating process. Analytical investigation of the process kinetics was required for which we used numerical simulation of the sputtering event that is presented in **Figure 9**. We used Sigmund’s linear cascade collision model [110] in the form of the semi-empirical sputtering equations reported by Seah *et al.* [111] with the recommended values used by Matsunami *et al.* [112]. These provide a simplistic, yet proven and efficient model for sputtering compounds [113]. The approach of Yamamura *et al.* [114] was used for oblique incident angle calculations. Detailed description of the used equations is given in the Appendix A of P2.

Based on previous studies we assume Ta target to be oxidized [80], [115] and that the molecular species being sputtered is Ta_2O_5 . Demiryont *et al.* [80] have shown that when the ion beam oxygen fraction exceeds 37.5% the sputtered Ta_2O_5 film is stoichiometric. The oxygen fraction for the ion beam used in this work is 38.5% and there is a constant 80 sccm O_2 flow directed to the target plate which according to Ohno *et al.* [115] already induces several nanometers thick oxide layer on the target.

In addition to the sputtering of Ta_2O_5 , we numerically examined the secondary sputtering effects at the semiconductor surface by the scattered Ar^+ ions and the TaO primary particles. The secondary particle energies are calculated assuming

elastic two particle collisions [116]–[118]. The semiconductor sputtering calculations follow Seah’s compound equations [113] and Malherbe’s review on sputtering semiconductors [119]. The energy distribution of sputtered TaO particles is calculated with the flux equations introduced by Thompson [120]. The sputtering yields are calculated for GaAs, $\text{Al}_{0.53}\text{In}_{0.47}\text{P}$ and $\text{Al}_{0.4}\text{Ga}_{0.6}\text{As}$ compositions and their properties are assumed to be linearly constructed by the properties of their binary compounds. Such simplification omits any element preferential effects and might not represent the actual sputtering process of these compounds [113], [119], but fits with the experimental data of GaAs and Ta_2O_5 [113].

2.2.5 Nanostructuring Alumina

Amorphous thin film Al_2O_3 is known to form a porous structure when treated with heated DIW [92], [93]. Similar nanostructures have successfully been utilized in advanced ARCs, where they have enabled broadband operation and very low average reflectivity [53], [56], [98], [121]–[123]. For developing the ML ARC with nanostructure on top, the DIW treatment was tested and utilized for e-beam and IBS deposited alumina and other oxide materials. The DIW process is described in **Figure 10**.

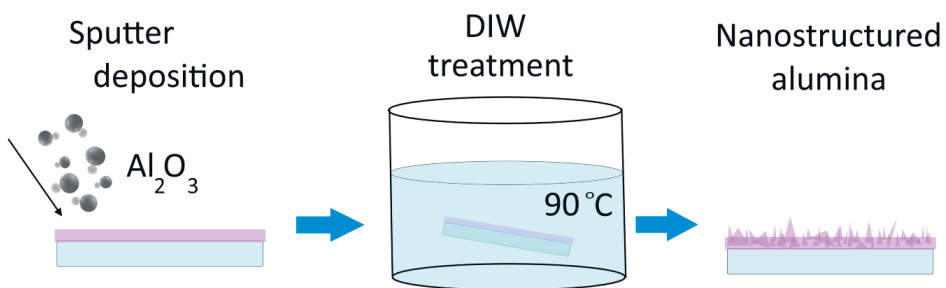


Figure 10 Alumina thin film is deposited by reactive ion beam sputtering on a substrate and then the sample is treated with hot de-ionized water bath to create nanostructured alumina coating [Adapted from P5].

The DIW had a resistivity of 18.4 M Ω and was pre-heated to the temperature of 90 °C on a hotplate before sample immersion. The temperature of the solution was constantly monitored during the treatment and no agitation was used. Treatment time was kept constant at 30 minutes.

A distinct advantage of the DIW nanostructuring compared to the lithography processes is the reduced number of fabrication steps [59], [60]. Also, using reactive ion etching (RIE) for patterning can cause losses via plasma damage and byproducts, if the process is not carefully optimized for the MJSC materials [124]–[128]. The properties of the alumina nanopattern can be controlled via the original planar film thickness and the DIW treatment time [94].

Nanostructured alumina layers were used in three manuscripts, i.e. P3-P5.

2.2.6 Hydrophobicity Treatment of the Nanostructure

Bare nanostructures can be prone to water adsorption and mechanical damage due time. To prevent these, superhydrophobicity treatments are often applied to achieve omniphobic properties [129]–[135]. Treating a nanostructure with an additional low surface energy polymer, such as organosilane [129], [131], fluoropolymer [129], [133], [136], or polydimethylsiloxane [130], [135] usually provides hydrophobicity. For the nanostructured alumina, a fluoropolymerization by CHF₃ plasma is known to produce superhydrophobic properties [95].

As P5 aimed to improve the stability of the ML ARC having nanostructured alumina on top, a fluoropolymerization by a RIE system with a polymerization process of CHF₃ plasma (50 sccm, 100 mTorr, 50 W) was applied for 7 minutes. The used system was Plasmalab 100 by Oxford Instruments Plasma Technology GmbH. The polymerization process is presented in **Figure 11**.

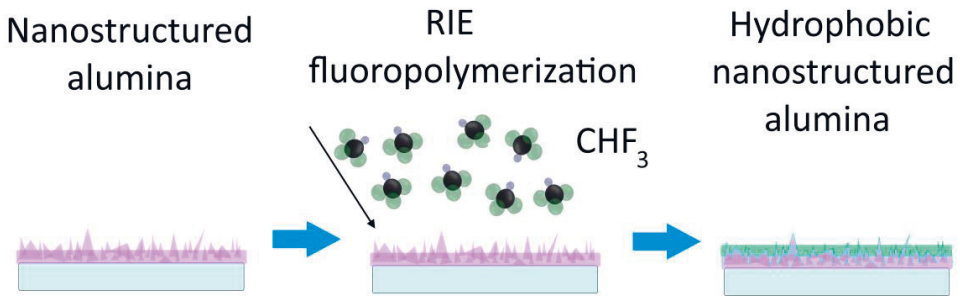


Figure 11 Fluoropolymerization of nanostructured alumina by CHF_3 plasma treatment leads to hydrophobic properties for the film [Adapted from P5].

The functionality of the hydrophobicity treatment was compared against the bare nanostructured alumina and planar alumina coatings. All three coatings were exposed in atmospheric icing for durability assessment and the properties before and after the exposure were characterized.

Hydrophobicity treatment was utilized in the P5 manuscript.

2.3 Basics of Multijunction Solar Cells

There are different ways to fabricate III–V MJSC architectures most important of which are inverted metamorphic (IMM) [15], [48], [137], [138], wafer-bonded [47], [139], and lattice-matched (LM) [16], [26], [35], [140] approaches. The MJSCs in this thesis are all monolithically grown and lattice-matched to GaAs. The used growth method, molecular beam epitaxy (MBE), is based on evaporating a suitable III–V mixture on a seed crystal, in our case an epitaxial grade GaAs wafer, on which the grown compound material replicates the crystalline structure of the substrate. Lattice-matching requires the grown materials to have close enough lattice constant compared to the substrate material. Pros of the LM MBE are its excellent crystal

quality and low amount of used material when compared to i.e. IMM. Cons include high cost and relatively low growth rates. **Figure 12 a)** shows a simplified schematic of a MBE system for III–V growths. MBE systems are operated under ultra-high vacuum (UHV) conditions, as the epitaxial growth requires the precursor molecules to have a clear line of sight from the effusion cells to the substrate. MBE is mainly done at the pressure range of 10^{-8} - 10^{-9} mbar, which corresponds to a mean free path in order of meters or dozens of meters. In addition to the base pressure of the system, the most important physical parameters affecting to the film growth are the amount/ratio of the arriving molecules and the temperature of the substrate. The MJSCs of this thesis were grown as bottom-up structures, in which the growth starts from the substrate with the bottommost layer and is proceeded layer by layer by alternating the material fluxes with shutters, until the complete MJSC structure is complete.

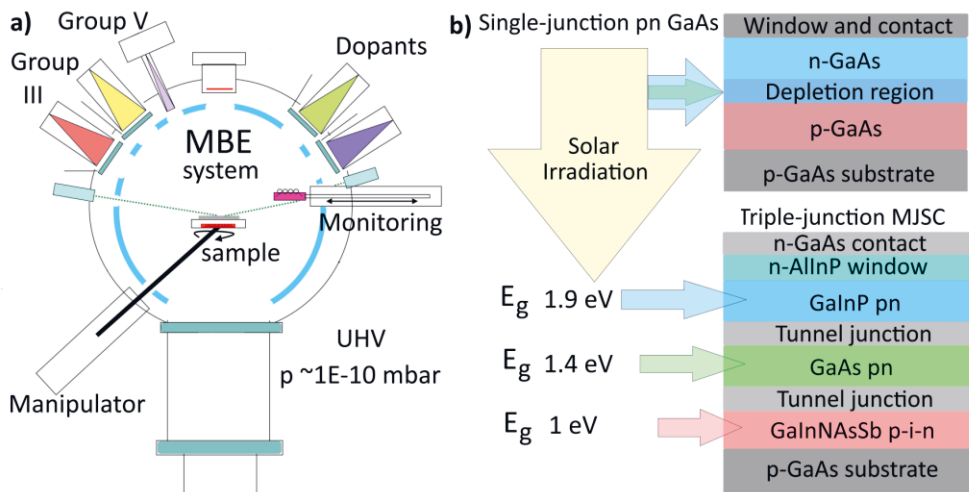


Figure 12 a) A simplified illustration of a molecular beam epitaxy system for growing III–V semiconductors. **b)** A single-junction GaAs pn-junction and a triple-junction GaInP/GaAs/GaInNAsSb MJSC and the principle of how the fractions of the solar irradiation are utilized by the structures.

A single-junction semiconductor solar cell consists typically two main layers doped with different types of impurities. Such a structure for a GaAs single-junction SC is shown in **Figure 12 b)**. The layer that is doped with electron donor atoms is referred as n-type material and the layer that is doped with electron acceptor atoms is called p-type material. The number of impurities is small compared to the number of main semiconductor atoms, so the defining difference between the layers is the number of electrons. In the n-type layer there is an excess of electrons that are free to operate as negative charge carriers. In the p-type material there is similarly a certain number of electron vacancies, which are referred as holes, that can act as positive charge carriers. A simplified operating principle of a semiconductor solar cell is that when illuminated with light the electrons in the doped layers absorb the incident photons and the photogenerated minority carriers are transported to the depletion region. The strong electric field and the fixed space charge of the junction separates the collected minority carriers and the generated charge difference creates a potential across the cell and produces electrical power. [141]

A MJSC is basically a collection of single-junction SCs, stacked together in some of the methods mentioned in the beginning of this subchapter. Monolithic LM MJSCs require tunnel junctions in between the subcells to enable a series connection of the structure [22], [142]. Tunnel junctions need to have low electrical resistivity and high optical transmissivity. Because of the high doping, a small positive voltage applied to the junction is enough for the charge carriers to tunnel through the barrier, which enables high current density flows at low voltages. **Figure 12 b)** shows a triple-junction GaInP/GaAs/GaInNAsSb MJSC with the associated bandgaps of the subcells. Owing to the different bandgaps of the junctions a MJSC can utilize a wider spectrum of the solar irradiation than a single-junction device. As the solar cells in LM MJSC structure are series connected, the least current producing junction sets the limit for the current production capability of the complete stack. Any excess current produced by the other junctions will be mitigated by losses, such as

thermalization. Therefore, all the junctions in an optimized LM MJSC structure should produce close to the same current. This principle is referred as current-matching.

The current-matching requirement for the MJSC structures sets additional limitations for the design of a broadband ARC. The average reflectance plays a smaller role than the overall balancing of the structure, while the interference of the multilayer structure makes it challenging to have both suitably low and broadband reflectance [33], [143]. A conventional double-layer ARC structure can be an efficient solution up to three junctions [16], [33], [49], but achieving optimal reflectance reduction with more junctions requires additional ARC layers [9], [33] and/or nanostructuring [53]–[60]. Even the state-of-the-art triple-junction solar cell utilizes a four-layer design as its ARC [61]. Therefore, the thesis aims to develop nanostructured ML ARC to match all the requirements set by the MJSC designs.

This work was carried out with lattice-matched triple-junction GaInP/GaAs/GaInNAsSb and AlGaAs/GaAs/GaInNAsSb MJSCs and four-junction GaInP/GaAs/GaInNAsSb/GaInNAsSb MJSCs. All the studied III–V MJSC structures were grown in-house using a Veeco GEN20 MBE system.

3 THIN FILM CHARACTERIZATION

Optical thin film is defined as a film with a thickness that still produces recognizable interference effect on a substrate. Such films usually have a physical thickness ranging from nanometers to micrometers depending on the optical properties, namely refractive index (n) and extinction coefficient (k) of the material, and the specific wavelength in question. Thicker films are considered as bulk-like material. Despite the nanoscale dimensions, thin films can be characterized versatily and there are multiple ways to categorize the different methods. Here, the characterization techniques are divided in microscopy for structural characterization, optical techniques for assessing optical properties of the films, and other section that covers the rest of the used characterization methods.

3.1 Microscopy

Optical thin films usually produce a visible effect on the substrate but based on the mere outlook it is difficult to estimate the actual surface quality of the coatings. Their physical dimensions are small, ranging from nanometers to micrometers, so accurate evaluation requires microscopy. Optical microscopes can easily provide a magnification of 100 times the original size, but to reach the nanometer range, beyond the diffraction limit, requires $\sim 50k-100k$ times magnification. Such precision can be provided by atomic force microscope (AFM) and scanning electron microscope (SEM).

3.1.1 Atomic Force Microscopy

Atomic force microscopy is used to map the surface potential variations (linked to Van der Waals force, dipole-dipole interaction, and other electrostatic forces) along a sample surface, yielding a topographical representation of the surface features. In this work we used a Veeco Dimension™ 3100 AFM in the so called tapping mode, where the oscillation variations of the tip provide the feedback from the surface. The used tip model was a PPP-NCH-50 silicon probe by Nanosensors™. **Figure 13 a)** shows an exemplary surface topography map for MgF₂ surface and **Figure 13 b)** presents the tapping mode working principle.

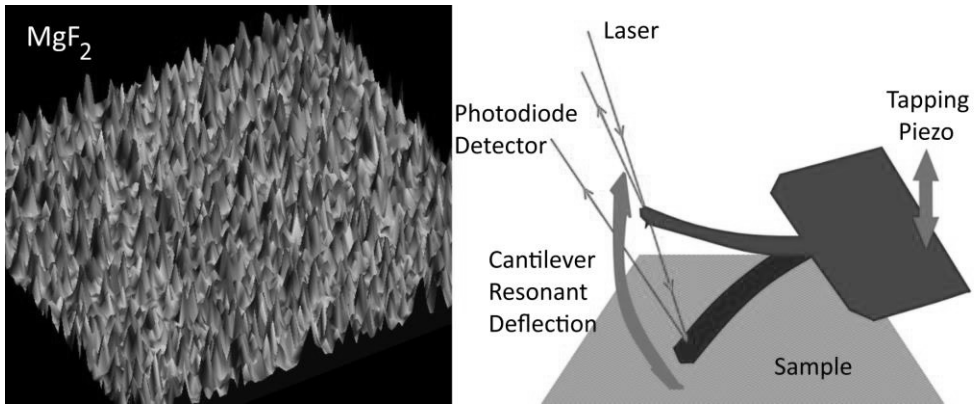


Figure 13 a) A 3D-presented AFM surface topography map of MgF₂ thin film. b) A representation of the working principle for the tapping mode imaging.

AFM utilizes electrical stepping motors and piezoelectric crystal to move the tip and scan the investigated sample. In the tapping mode the cantilever is driven to oscillate vertically near its resonance frequency by the piezoelectric element. The interacting forces change the elastic constant of the probe, while the feedback loop maintains a constant oscillation amplitude. The vertical position of the cantilever at each lateral measurement point is stored and used to form a topographic image of the sample surface. For the post-measurement image construction, a WSxM 5.0 Develop 8.2-

9.4 software was used [144]. From the topography data it is possible to extract statistical values that describe the sample surface in a comparable way. In this work, the three main statistical values examined were the root mean square roughness (R_{rms}), average roughness (R_{ave}) and average height. Although AFM can provide various kinds of accurate information about the surface being measured, its biggest downside is the relatively slow scanning procedure, which usually limits the scanning area from few to tens of micrometers.

3.1.2 Scanning Electron Microscopy

Nanosized features cannot be optically imaged with traditional microscopes due to the diffraction limit that basically restricts accurate imaging for features smaller than half the imaging wavelength. With visible light the lower limit is ~ 200 nm. Some metamaterial concepts, like super- and hyperlenses, utilizing negative refractive index materials are under investigation, but are so far beyond practical implementations for everyday imaging [145]–[147]. Instead of photons, one can use electrons for the imaging purposes. The method is called scanning electron microscopy, where the working principle is to sweep the imaged surface with a narrow beam of electrons and collect the emitted electrons from the surface with different kinds of detectors. The sweep line scans are collected and used to form an image of the surface. SEM can image features as small as 1 to 10 nm depending on the used system and the sample being imaged. SEM is able to picture 3D structures and enables detailed characterization of surface morphology and textures. Imaging is fast and the main sample requirement is to have a conducting surface [148]. **Figure 14** demonstrates how zooming into larger magnification reveals the surface nanostructure that is not detectable with the lower zoom.

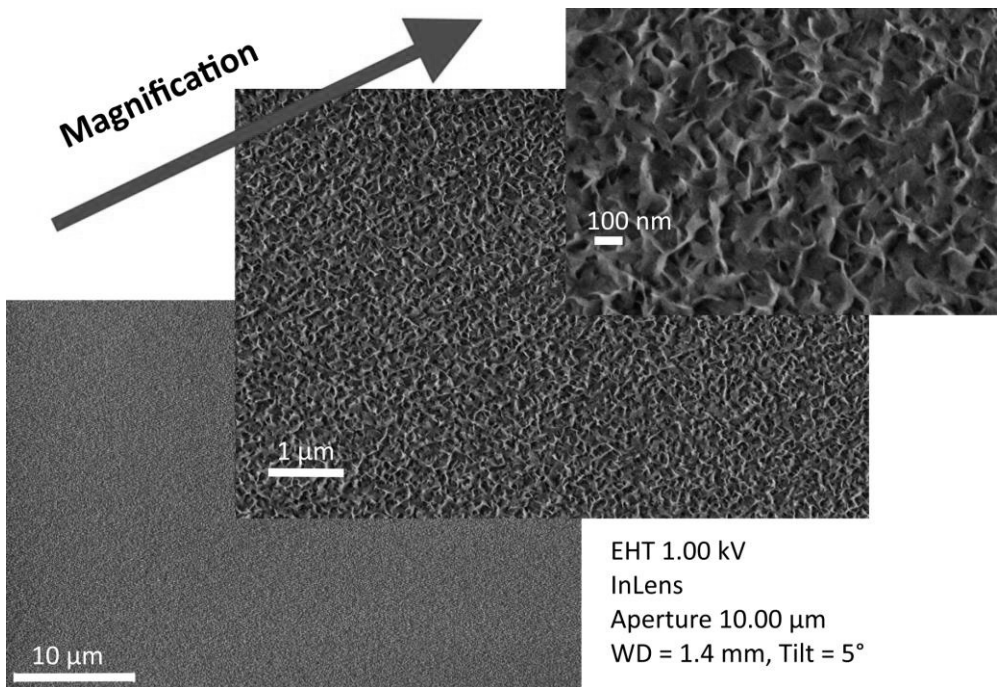


Figure 14 With a scanning electron microscope it is feasible to reach magnifications of ~few 100k times the original size, which enables examining nanosized features, such as the nanostructured alumina shown here.

As the ARCs are mainly dielectric materials, imaging their surface accurately with SEM can be difficult. Scanning for too long or with an intensive electron beam can lead to local charging of the surface causing distorted features and blurry images. Techniques to avoid the local charging include using a low acceleration voltage, a small aperture, and a slight tilt for the sample. All the SEM images were taken with a SIGMA™ FESEM operated with SmartSEM® software, both products of Carl Zeiss NTS Ltd.

3.2 Optical Assessment Techniques

As optical coatings are designed to manipulate light by the means of interference in the layered media, a natural way to characterize the films is to use variable optical techniques. The main methods used in this thesis and shortly presented in the following subchapters are ellipsometry, spectrophotometry and photoluminescence spectroscopy.

3.2.1 Ellipsometry

Ellipsometry refers to a technique, in which the change of the polarization of light when reflected from a surface, either bare or thin film coated, is measured. From the measurement, one can determine the reflectance ratio of the two linear polarizations, parallel to the incidence plane and perpendicular to the incidence plane, p- and s-polarization, respectively. This complex ratio ρ , can be presented with two angles Ψ and Δ as:

$$\rho = \frac{r_p}{r_s} = \tan \Psi e^{i\Delta}, \quad (15)$$

in which the r_p and r_s are the measured reflection coefficients for the polarizations [149]. With the angles Ψ , relative amplitude change, and Δ , phase difference, the optical constants n and k , and the physical thickness of the measured film can be fitted. Depending on the sample and the used measurement configuration, the fitting procedure can be tedious and non-conclusive, and in the least case requires a certain level of expertise. The results included in the thesis are either automatic calculations by the used measurement system or fits done by a specialized operator. **Figure 15** a) presents the electric field amplitude of elliptically polarized light propagating along z-axis with the relation of the angles Ψ and Δ . **Figure 15** b) shows how the Ψ and Δ

vary as a function of wavelength, that can be used for fitting optical constants of dispersive media.

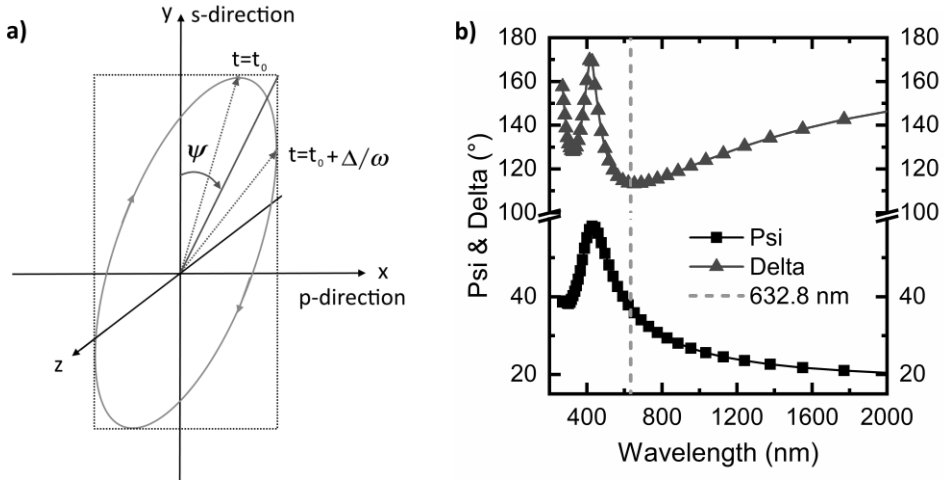


Figure 15 a) Polarization of light is defined by the amplitude variations in s- and p-directions along the propagation axis z. b) By measuring the changes in polarization as a function of wavelength by ellipsometry the thin film properties, namely refractive index, physical thickness, and extinction coefficient, can be calculated.

If Ψ and Δ are measured at a single wavelength, the setup is called a monochromatic ellipsometer and if the measurement is done across a bandwidth and with varying angles, the system is referred as spectroscopic ellipsometer. The monochromatic values used in this thesis are measured at $\lambda = 632.8$ nm.

The refractive index of the materials that were measured with spectroscopic ellipsometry are fitted with the Sellmeier dispersion formula [150]. For the materials that include absorption in the short wavelength region, namely TiO_2 and Ta_2O_5 , Tauc-Lorentz model [151] was applied. The monochromatic measurements were done in-house at Tampere University with a Rudolph AutoEL III Null ellipsometer equipped with a He/Ne laser at $\lambda = 632.8$ nm and the spectroscopic ellipsometry

measurements were done at the University of Eastern Finland with a J.A.Woollam VASE spectral ellipsometer. The presented uncertainty intervals for spectroscopic ellipsometry results are given by the WVASE32® Version 3.774 software according to the used models, which does not consider the possibility of a systematic error due to the cross-dependence of the material parameters and presumes a normal distribution for the uncertainties.

3.2.2 Spectrophotometry

In spectrophotometry one can measure three quantities: transmittance ($T\%$), reflectance ($R\%$), and absorbance ($A\%$). $T\%$ measures how much light is transmitted through the sample, $R\%$ how much of the incident light is reflected from the surface, and $A\%$ how much of the light is absorbed in the structure. With the ARCs we would like to avoid absorbing materials and have mainly measured $T\%$ and $R\%$, although the high refractive index materials can have some absorption at the UV range. As our substrate is very often a MJSC beneath the ARC, the reflectance is the key quantity compared between ARC designs, as the incident light that is not reflected should be absorbed in the MJSC. Transmittance measurements are mainly done on test ARCs on glass. The two measurement configurations, used for the spectrophotometry in the thesis, are an integrating sphere and a universal reflectance accessory (URA), latter of which is a trademark of PerkinElmer Inc. With the integrating sphere one can measure either transmittance or reflectance and the sphere should collect also diffused light. With URA only specular reflectance can be measured, and the smallest measurable angle is 8° . The operating principle of the integrating sphere is shown in **Figure 16** a) and the operating principle for URA in b).

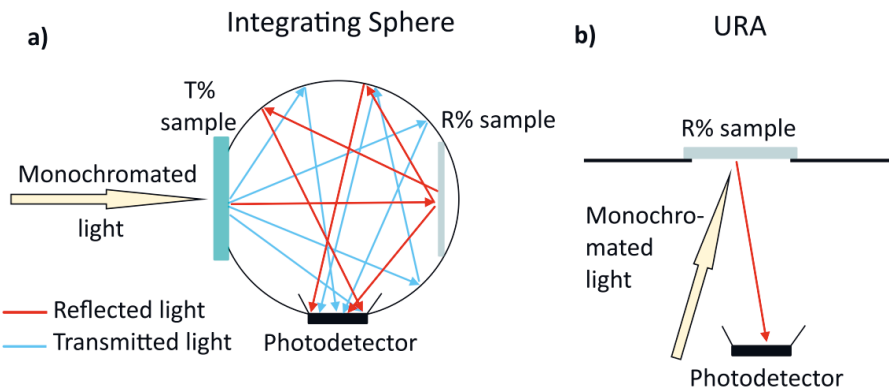


Figure 16 a) A simplified illustration of an integrating sphere used for both transmittance and reflectance measurement. The sample configuration with measurement settings define which quantity is measured. b) Universal reflectance accessory (URA) configuration for reflectance measurement.

The integrating sphere enables measurement at the normal incidence angle and gives more realistic picture of the ARC reflectance due to the included diffused components. URA module has been used when the sample size and focusing of the incident light of the integrating sphere have not been compatible with each other. The spectrophotometer measurements were done with a PerkinElmer Lambda 1050 UV/VIS/NIR spectrophotometer.

3.2.3 Photoluminescence Spectroscopy

In photoluminescence (PL) spectroscopy a sample is illuminated with monochromate incident light, usually with a laser, and the light generated by the illuminated structure is measured with a detector. The physical principle of photoluminescence is presented in **Figure 17** a). The photons provided by the incident light excite electrons from the valence band (E_v) to the conduction band (E_c) and produce an electron-hole pair. The pair is radiatively recombined when the

electron falls back to the valence band, which produces a new photon with energy matching the band gap (E_g) of the material. If the electrons would have only one possible state to be excited to, the produced light would be monochromatic. However, in a real material system there is a distribution of possible states, and the produced signal will match that. A photoluminescence spectrum for GaAs ($E_g \approx 1.42$ eV) is shown in **Figure 17 b**).

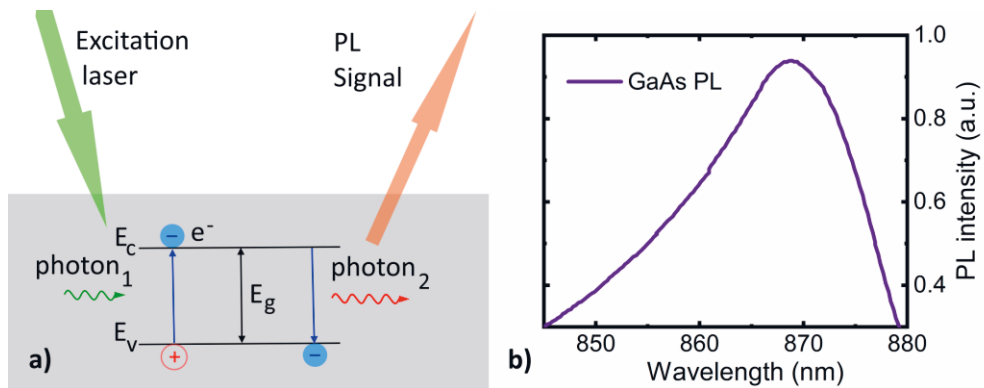


Figure 17 a) The principle of photoluminescence excitation and radiative recombination that produces PL signal. b) Example spectra of GaAs photoluminescence.

For characterizing MJSCs PL spectroscopy offers a non-invasive method, that allows versatile evaluation with variable excitation depths [152], [153]. In the thesis we compared mainly PL intensity changes that indicate effects of the ARC deposition process on the quality of surfaces, bulk and interfaces [154], [155].

PL measurements were used to probe the top and middle junctions of the MJSC structures in P2. The GaInP and AlGaAs top junctions were probed with 532 nm laser both in continuous wave (CW) and Q-switched modes using a 300 g/mm grating, a 570 nm high-pass filter, and a CCD detector. The effects on the GaAs junction were evaluated by measuring the PL with CW 785 nm excitation using a 300 g/mm grating, an 850 nm high-pass filter, and an InGaAs detector. The effects

of the reflectance changes due to the ARCs were corrected, by calculating the influence of reflectance at the pump and signal wavelengths on the PL intensity as:

$$I_{\text{PL},0} = \frac{I_{\text{meas}}}{(1-R_{\text{pump}})(1-R_{\text{PL}})}, \quad (16)$$

where $I_{\text{PL},0}$ is the reflectance corrected signal, I_{meas} the measured signal, R_{pump} reflectance at the pump wavelength, and R_{PL} reflectance at the signal wavelength. The reflectance corrected signal was then normalized according to the pre-deposition signal, so that prior the ARC the signal is 1. This way the intensities should be ≥ 1 for non-damaged samples after the deposition. The system used in this work was an Accent RPM2000 PL mapper.

3.3 Other Characterization Techniques

In addition to the microscopy and optical characterizations, a few other methods played key roles in the investigation of the coating properties and functionality. These are shortly presented in the following sections.

3.3.1 Light-biased Current-Voltage Measurements

When it comes to ARCs on MJSCs, the key merit for the functionality of the coating is how well it improves the operation of the solar cell compared to an uncoated cell. A realistic way to measure that would be to set up the solar cell under sunlight and measure the produced voltage and current. Problem with the real Sun is that it rarely shines from the exact same position with the exact same spectrum, which would make comparing the performance of an uncoated solar cell and the same solar cell after ARC deposition difficult. Instead, a solar simulator is used that produces repeatable conditions for the solar cell performance comparison that can be further verified with the known standards. The system used in this work was a 7 kW OAI

TriSol solar simulator calibrated for AM1.5D (1000 W/m^2) illumination. Such a measurement for a 4-junction MJSC is shown in **Figure 18**.

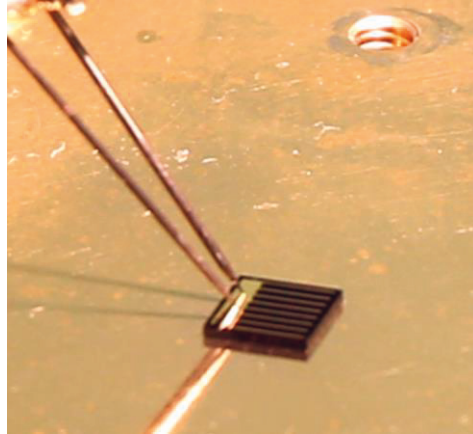


Figure 18 Measuring light-biased current-voltage of a 4-junction MJSC under a solar simulator. [Image by Dr. Antti Tukiainen]

The simulator system uses a high intensity Xenon lamp and filters to produce a solar like spectrum that is collimated to the measured solar cell. The produced light-biased current-voltage (LIV) values are recorded for comparison. **Figure 19** shows three different LIV curves and presents the main points used for performance evaluation.

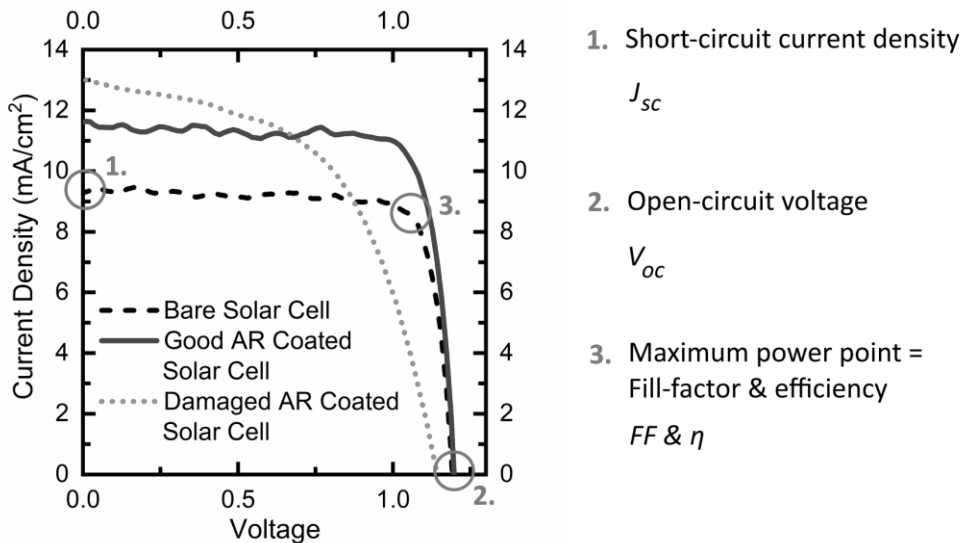


Figure 19 Light-biased current-voltage measurement shows the electrical quality of the solar cell and distinct differences at key performance points between a good and a defective component.

The short-circuit current density (J_{sc}) is the current density recorded when the back and front metal contact of the solar cell are short-circuited. The open-circuit voltage (V_{oc}), is similarly the maximum voltage that the solar cell can generate, which takes place when the terminals are not connected and the photogenerated carriers build up the voltage by charge diffusion. The maximum power generation is less than $J_{sc} \times V_{oc}$, as loss mechanisms such as recombination losses, shunt resistance and series resistance reduce the corresponding J_m and V_m . Even for an ideal SC the diode-like behavior prevents FF reaching 1, as the generated current is exponentially related to the voltage. The ratio between the maximum power point values and the product $J_{sc} \times V_{oc}$ is called the fill-factor as:

$$FF = \frac{J_m V_m}{J_{sc} V_{oc}}. \quad (17)$$

The fill-factor together with the short-circuit current ($I_{sc} = J_{sc} \times \text{cell area}$) and the open-circuit voltage can be used to calculate the conversion efficiency of the solar cell:

$$\eta = \frac{FF I_{sc} V_{oc}}{P_{opt}}, \quad (18)$$

in which P_{opt} is the power of the incident light. Generally, ARC should mainly affect the amount of light reaching the solar cell structure, which is directly linked to the current generation of the SC, namely J_{sc} . However, optimized ARC might also act as a passivation component reducing recombination losses, or in non-optimal case the opposite. If the ARC functions properly the shape of the LIV curve should remain the same and the produced current increase in proportion of the reduced reflectance, as is shown in **Figure 19** when the bare SC and the same SC with good ARC are compared. Significant improvements in V_{oc} and FF would imply reduced recombination losses. When recombination is increased or some of the junctions are shorted, due to the ARC process damaging the SC, the LIV curve shape is distorted, like the red dotted curve in **Figure 19**. LIV characteristics provide a straightforward quantity for the comparison of ARC quality, as it shows how much the ARC benefits the SC.

3.3.2 External Quantum Efficiency

Like the LIV, external quantum efficiency (EQE) gives a measure of the electrical quality of the solar cell, but also of the optical quality of the device. The EQE is a quantity that describes how many charge carrier pairs is generated per photon arrived at the solar cell. The more the photons are reflected from the solar cell, the smaller the EQE. Other variables affecting to the EQE values are transmission and

recombination losses. In an ideal case, in which every arriving photon produces an electron-hole pair, EQE equals 1. A good ARC should increase the EQE proportionally to the reduced reflectance, unless the deposition induces electrical losses in the SC. An example EQE for a top-junction GaInP solar cell with and without an ARC is presented in **Figure 20**.

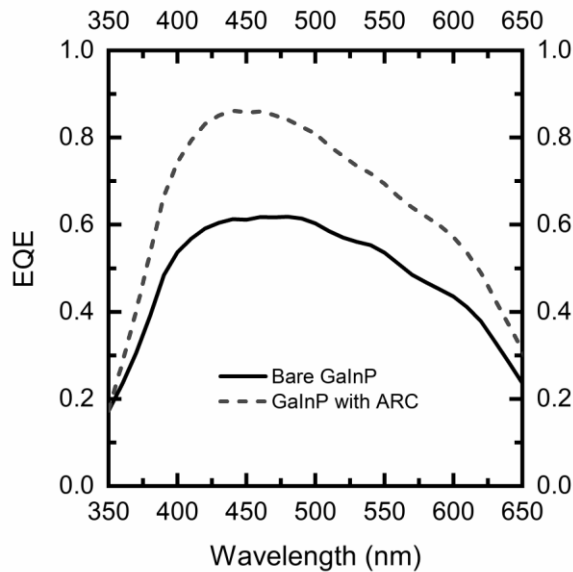


Figure 20 EQE of a bare GaInP top junction for MJSC configuration and the same solar cell with an ARC.

The EQEs in the thesis are measured with an in-house built monochromator-detector-based system which is adjusted using a NIST (National Institute of Standards and Technology) -calibrated Si reference cell at room temperature (22°C). For EQE derived current densities a python script based on May *et al.* integration tools [156] was used.

3.3.3 Icing and Ice Adhesion Tests

To assess the durability of the nano-ARC, with and without the hydrophobicity treatment, atmospheric icing tests were concluded. A mixed glaze type ice was accreted by using an icing wind tunnel (IWiT) at Tampere University Ice Laboratory. A centrifugal ice adhesion test (CAT) was used for ice adhesion measurements [157]. In IWiT supercooled water droplets are accelerated to and frozen onto the tested surfaces. The thickness of the accreted ice was ~10 mm. In CAT the iced sample is rotated with a constant acceleration speed until the ice layer detaches. The detachment moment is logged with an acceleration sensor, and the ice adhesion strength is calculated by dividing the centrifugal force with the iced area [157]–[160]. The following list presents the ice adhesion strength ranges for CAT values:

- Extreme low < 10 kPa
- Low 10-50 kPa
- Medium-Low 50-100 kPa
- Medium 100-150 kPa
- High > 150 kPa

Additional ice durability tests were done after CAT testing, where ice was accreted on the surface again in the IWiT. After the ice accretion, the samples were left to the cold conditions to freeze for one hour. Afterwards, the de-icing was done at the room temperature. In the de-icing, the samples were positioned vertically and held there until the ice was removed. This procedure was repeated four times, after which possible differences in the surface wetting behaviour were characterized.

As atmospheric icing is one of the harshest environmental conditions and can lead to extensive structural damage for the surfaces, it was chosen to be used as an accelerated aging and wear test for the nanostructured alumina coatings. It is expected that the hydrophobicity wears off due to cyclic icing [161]–[163] as the frost

formation via condensation will wear out the nanostructures on the surface [164]–[166]. However, the comparison reveals the differences between the coating types and shows if a hydrophobicity treatment is a must for this type of alumina nanostructures for long-term usage in MJSC ARCs.

3.3.4 Contact Angle Measurements

Water contact angle (CA) measurements are used to determine of what type of hydrophobicity/-philicity the coatings possess. Hydrophilic coatings have $CA < 90^\circ$ and hydrophobic have $CA > 90^\circ$. Superhydrophilic surfaces spread the droplet and superhydrophobic coating have $CA > 150^\circ$. **Figure 21** presents the CAs in accord to the hydrophobicity definitions.

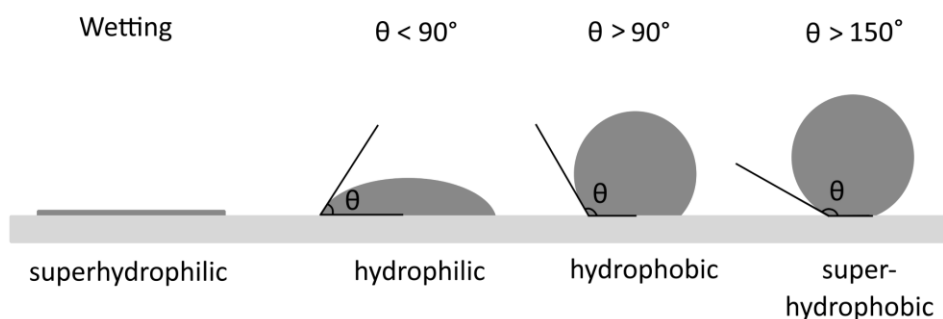


Figure 21 The static contact angle is used to describe hydrophobicity and hydrophilicity of a material based on the magnitude of the contact angle θ between the water droplet and the surface [167], [168] [Adapted from P5].

Although static contact angle (SCA) is typically used as the standard for hydrophobicity evaluation, also the receding contact angle (RCA) and advancing contact angle (ACA) were measured. RCA has been shown to be more directly linked

to the differentiation point (90°) between hydrophobicity and hydrophilicity [167], [169]. Generally, RCA measures the surface adhesion and ACA the surface wettability [167], [169]. CA hysteresis is the difference between RCA and ACA and is mostly due to chemical and topographical heterogeneity of the surface, or surface alteration by the solution [170], [171]. As RCA and ACA give the local maximum and minimum values that SCA can have on the surface, smaller hysteresis indicates more stable and uniform performance by the coating. In this work the contact angles were measured before icing tests, after CAT testing, and after cyclic icing-melting testing to investigate the durability of the bare alumina nanostructure, the hydrophobicity treated alumina nanostructure, and the planar alumina film. The contact angle changes allow to estimate the stability of each of the coating types and their suitability for long-term MJSC ARCs. The system used was a DSA100 from Krüss GmbH and the measurements were done with a 5 μL droplets of ultra-high purity water.

4 RESULTS AND DISCUSSION

This thesis approached the development of MJSC ARCs with three main tasks:

- I. Studying annealed e-beam evaporated MgF_2 as a low refractive index material.
- II. Studying IBS deposited Ta_2O_5 as a high refractive index material with low absorption.
- III. Developing and testing a multilayer ARC with a nanostructured alumina top layer.

All tasks aimed at an improved solution for a broadband and durable ML ARC for III–V MJSCs in space and terrestrial concentrated photovoltaics.

4.1 Annealing Low Refractive Index Magnesium Fluoride

Magnesium fluoride is the most commonly utilized low refractive index material in the ARCs of the reported high-efficiency III–V MJSCs [15], [45], [46], [172]. Its attractiveness is based on the 2nd lowest refractive index of usable natural thin film materials, being topped only by cryolite [173]–[175], and well established deposition processes. In the publication P1, we studied its temporal stability as well as the influence of deposition conditions and ex-situ rapid thermal annealing in hopes of reducing the film porosity and thus the effects of environmental variations on the coating performance.

The e-beam evaporated MgF_2 films had a set of different substrate temperatures (T_s) as 50 °C, 100 °C, 150 °C, 200 °C, and 240 °C. It is assumed that the films are either amorphous or polycrystalline in nature [176], as MgF_2 films reportedly

crystallize above 250 °C deposition temperatures [177]. The corresponding refractive indices measured by spectroscopic ellipsometer are shown in **Figure 22** a).

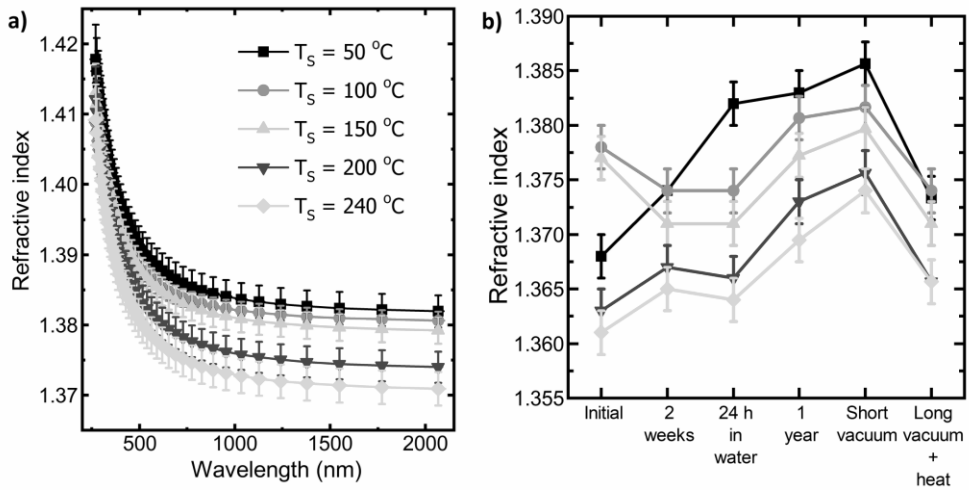


Figure 22 a) Dispersion of the MgF₂ films grown at different temperatures measured by spectroscopic ellipsometry. b) Refractive index at $\lambda = 632.8$ nm for the post-deposited MgF₂ films after varying conditions [Adapted from P1].

As the deposition temperature increases, the refractive index of MgF₂ seems to decrease. This can be attributed to the change of densely packed amorphous domains to polycrystalline phases, which leads to optically less dense structure. In the range of 30 °C to 150 °C the films should be amorphous and above temperatures of 150 °C the films shift to polycrystalline structure [176]. Reportedly, refractive index should start to increase with deposition temperatures higher than 250 °C [178]. As stated in chapter 2, the lower the refractive index of the lowest index material used in an ARC, the lower the achievable average minimum reflectance. So ideally, the films deposited at 200-240 °C should be suitable candidates for MJSC ARC, as they have clearly lower refractive index than the other films deposited at lower temperatures. However, the films should also endure time and environmental changes to actually work in a broadband ARC. **Figure 22** b) presents a measurement

series, where the stability of the MgF₂ films were monitored by their refractive index at $\lambda = 632.8$ nm. It is seen that none of the films maintain their refractive index as constant, but there is a shift for higher refractive index for each of the films after a year-long storage. This indicates that the films are somewhat porous and that the pores are filled by water due time. Following a procedure of heating in vacuum by Thornton and Harrison [101] the refractive indices were decreased and the relative difference between the films got smaller. The exposure of MgF₂ thin films to vacuum at 150 °C, should have caused a complete desorption of adsorbed water molecules [101]. Although the water adsorption seems to be a reversible process to some extent, the final refractive indices differ from the initial ones, which is not optimal when considering ARC design. The difference could be caused by some remaining hydroxyl groups on the surface of the film [101] or restructuring of the films due to the heat treatment.

In addition to optical stability, also the structural integrity of the films is important for real life applications. In **Figure 23** are shown SEM scans of the MgF₂ film surfaces after a year-long storage conditions.

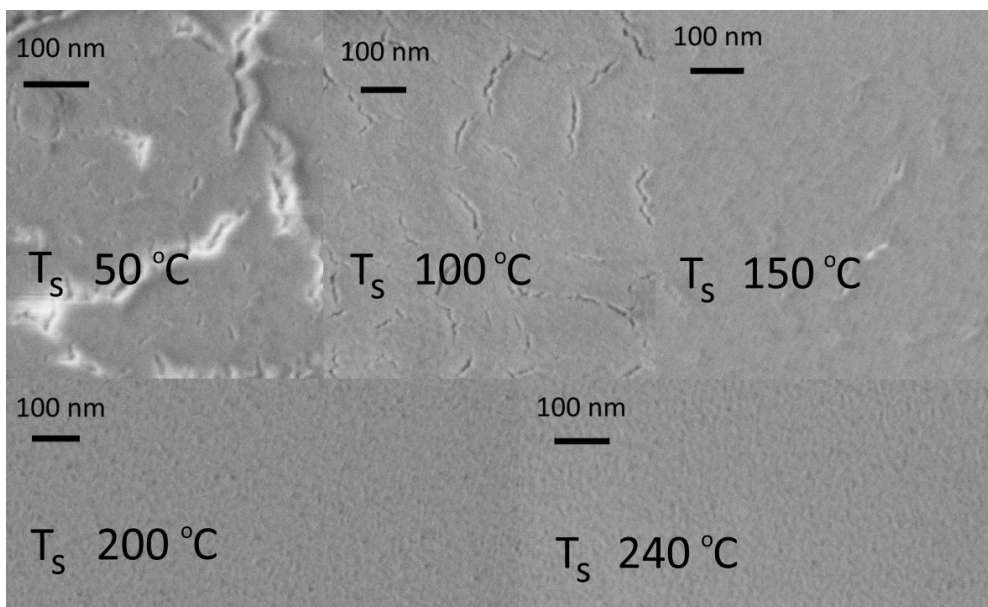


Figure 23 SEM surface scans of the growth temperature series reveals severe microcracking of the films grown at temperatures below 200 °C after a year-long exposure to atmospheric conditions [Adapted from P1].

One can see that the films deposited at temperatures 50-150 °C exhibited a large number of micro-cracks. The higher the T_s is, the smaller is the number of cracks, and with the temperatures 200 °C and 240 °C there are no noticeable cracks on the films. The cracking influences the optical and mechanical properties of the film, as it offers more sites for water vapor adsorption, and decreases both the abrasion resistance and the adhesion between the film and the substrate surface. Using such MgF₂ films evaporated at low temperatures in ML ARC would be problematic because micro-cracking could result in off-peeling of the coatings.

Aiming at reducing the porosity, an ex-situ RTA treatment was applied for the MgF₂ films, with the annealing temperature T_a varying from 300 °C to 1000 °C with 100 °C intervals. As annealing is known to roughen up the surface structure of the films [177], which then again affects the adhesion between thin films [179] and increases

surface scattering [180], we measured the initial deposition series surface roughness with AFM. The root-mean square roughness and average roughness for the film surfaces are shown in **Table 2**.

Table 2 Surface roughness of the MgF₂ films measured by AFM, as the root-mean-square roughness (R_{rms}) and the average roughness (R_{ave}).

Sample	R_{rms} [nm]	R_{ave} [nm]
$T_s = 50$ °C	0.48	0.38
$T_s = 100$ °C	0.48	0.38
$T_s = 150$ °C	0.44	0.35
$T_s = 200$ °C	0.57	0.44
$T_s = 240$ °C	0.56	0.44

A small increase in the surface roughness of the films is caused by higher deposition temperature, but all the values are still very small. In comparison, at room temperature e-beam deposited MgF₂ film has been reported to have a R_{rms} of 2.276 nm [177]. It would be preferable to maintain at least the order of roughness presented for the room temperature deposited MgF₂, which already is one order of magnitude coarser than our deposition series initially is.

The refractive indices of the annealed films are shown in **Figure 24 a**). The refractive index of films evaporated at $T_s = 200$ °C and 240 °C do not change much when compared to their as deposited values. However, the samples deposited below $T_s = 200$ °C have significantly lower refractive index values after the RTA treatments, that would indicate decreased amount of adsorbed water in the films. The refractive indices decrease as the voids of air have smaller refractive index ($n_{\text{air}} = 1.00$) than the adsorbed water ($n_{\text{water}} = 1.33$). At 600 °C the relative difference of refractive index is the smallest among the datasets. Above 600 °C the trend of decreasing refractive index changes rapidly and starts growing above 700 °C. We estimate the

change to be attributed to the lateral shrinkage of the films [181], which would also explain the rapid thickness increase shown in P1.

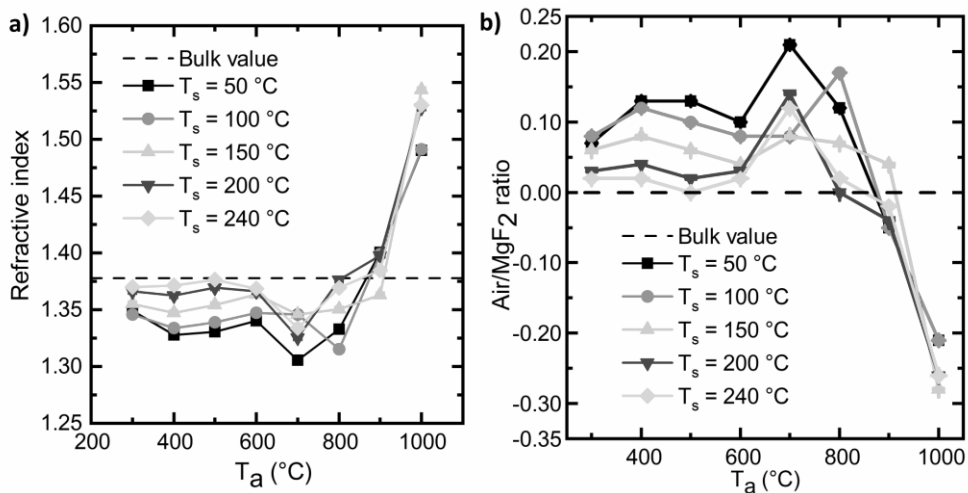


Figure 24 a) Refractive index at $\lambda = 632.8$ nm for post-deposition RTA processed MgF_2 films. b) Air/ MgF_2 ratios for the RTA treated films calculated with the EMA [Adapted from P1].

The air/ MgF_2 ratios calculated with Eq. 13 are shown in **Figure 24** b). The closer the ratio is to 0 the closer the packing density is to 1, as was shown in Eq. 14. For the films $T_s = 200$ °C and 240 °C the most beneficial treatment would be $T_a = 500$ °C, as their p closes to 1. For $T_s = 150$ °C treatment with $T_a = 600$ °C would be better. Above $T_a = 600$ °C the treatments clearly have negative effects on the film quality, as the porosity increases. We can state that the assumptions made for EMA calculations are no longer valid when the calculations yield negative values for air content.

As the RTA treatment affected the films deposited at different temperatures very similarly, the films deposited at $T_s = 200$ °C and annealed at $T_a = 300$ °C, 700 °C,

and 900 °C were chosen to be characterized with AFM. The surface topography maps of these AFM measurements are shown in **Figure 25**.

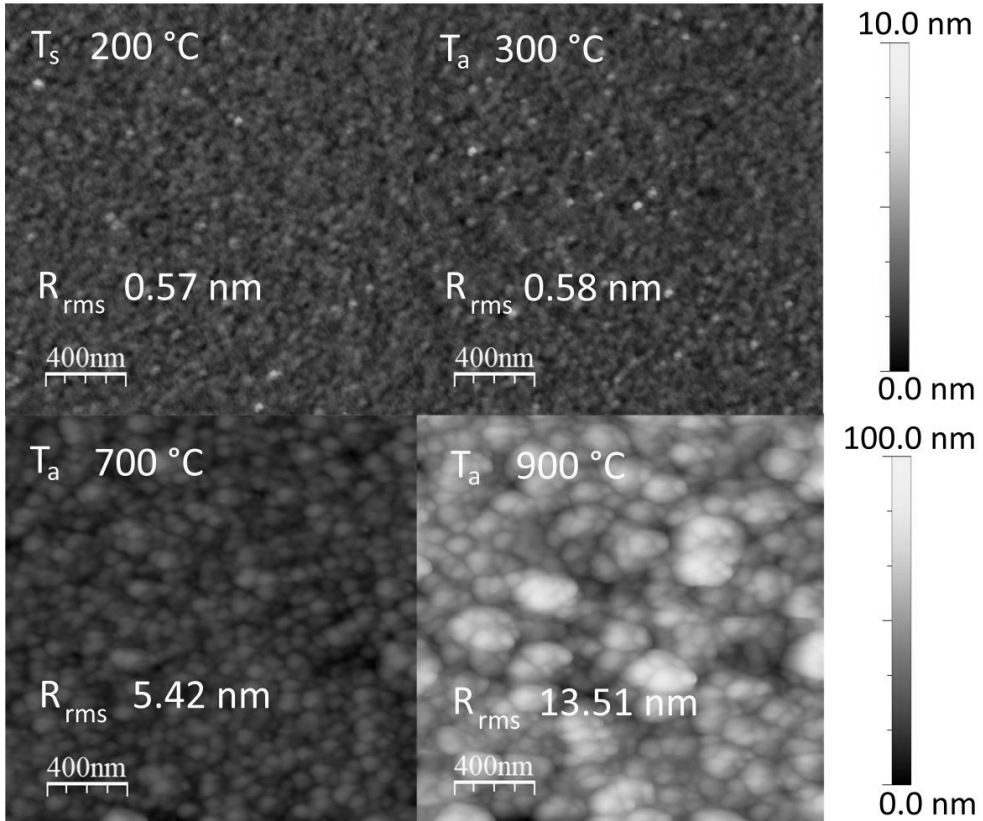


Figure 25 AFM topography maps of the annealed MgF_2 films with the root-mean-square roughness values [Adapted from P1].

When comparing the as deposited $T_s = 200\text{ °C}$ surface and the surface by the lowest annealing temperature $T_a = 300\text{ °C}$, we see that there is practically no change in the surface morphology. As T_a increases, the MgF_2 films start to form granular surfaces. At $T_a = 700\text{ °C}$ the surface is formed by grains of the size of 50 to 100 nm. At $T_a =$

900 °C the grain size is around few hundreds of nanometers and the R_{rms} is two orders of magnitude larger than the initial surface roughness after deposition. In hindsight, some additional AFM scans, like $T_{\text{a}} = 500$ °C for $T_{\text{s}} = 200$ °C and $T_{\text{a}} = 400$ °C for $T_{\text{s}} = 50$ °C, could have further elaborated the suitability of the RTA treatment for the post-deposition quality enhancement. But as is, the AFM measured series verifies that above 600 °C RTA processing is not beneficial, as was indicated by the ellipsometry measurements presented in **Figure 24**. Below $T_{\text{a}} = 700$ °C RTA processes seem to be effective in removing the adsorbed water and result in improved film quality. The upper temperature limit of $T_{\text{a}} = 700$ °C for RTA treatments is suitable for MJSC structures incorporating GaInNAsSb subcells, as the dilute nitride junctions generally benefit from annealing up to 800 °C [182], [183]. However, as the annealing affects the doping density [184], induces a bandgap blue-shift [185]–[188], changes the carrier lifetimes [189], and its effects are growth conditions and N composition dependent [183], [186]–[188], the possible RTA treatment for the ARC should be known and taken into consideration prior the MJSC design and growth.

Relative changes in reflectance due time for ARCs deposited at $T_{\text{s}} = 200$ °C were measured and presented in P1. The optical performance was negatively affected by caused humidity shifting the reflectance, as was predicted by the long-term refractive index changes shown in **Figure 22** b). A need to test post-deposition RTA treatments with a multilayer design is evident and it could help to reduce the influence of humidity and long-term exposure to ambient conditions by enhancing the quality of the MgF₂ top layer. Without a comprehensive testing with other constituent materials, the result would most likely be like in **Figure 2** b) and c) instead of a quality improvement.

As an additional test after publishing P1, we exposed MgF₂ deposited at $T_{\text{s}} = 200$ °C to the DIW treatment used for Al₂O₃ nanostructuring. Like Al₂O₃, MgF₂ seems to

react with DIW and to form a nanostructured surface. Surface SEM scan of the DIW treated MgF_2 is shown in **Figure 26**.

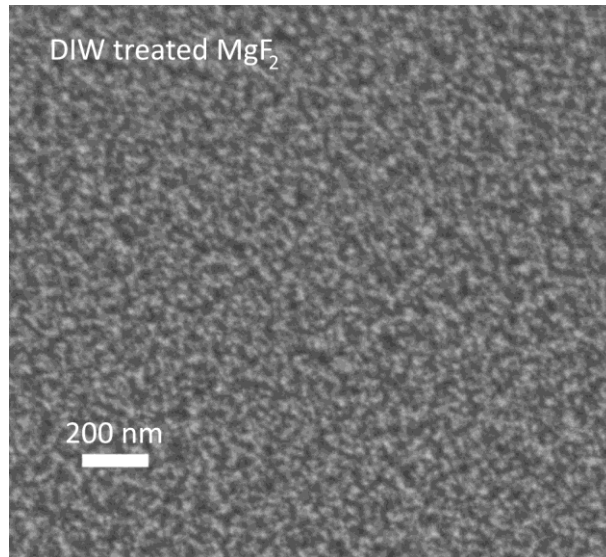


Figure 26 SEM image of DIW treated MgF_2 surface that shows minor structuring compared to the as-deposited surface.

The reactivity with DIW and the observed porosity of the e-beam deposited MgF_2 prevents using it as an intermediate layer in ML ARC between the nanostructured alumina and silica. As a topmost nanostructured layer, instead of alumina, it could potentially enable lower average reflectance than current MgF_2 -ARCs that utilize only planar top layers, but this has not been yet investigated.

4.2 Optimizing Ion Beam Sputtering Process of Ta₂O₅ for III–V Materials

Motivation behind using Ta₂O₅ instead of TiO₂ lies in its similarly high refractive index and lower absorption in the UV region [80], [81]. **Figure 27** a) shows the refractive indices for both materials deposited with IBS measured with spectroscopic ellipsometer. **Figure 27** b) presents the related extinction coefficients.

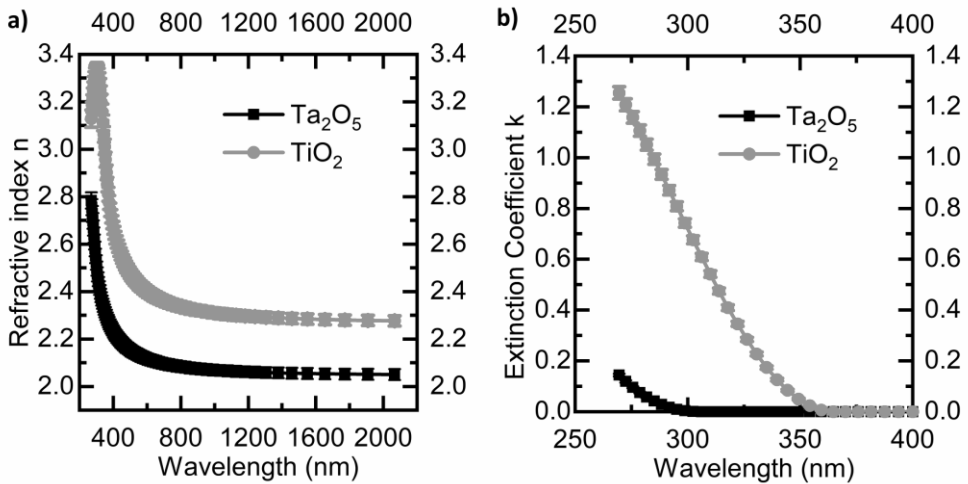


Figure 27 a) Measured refractive index of IBS deposited Ta₂O₅ and TiO₂. b) Extinction coefficients of the same Ta₂O₅ and TiO₂ films.

Both TiO₂ and Ta₂O₅ are regarded as high refractive index materials and the differences in their optical constants are moderate as is evident from the **Figure 27**. Replacing titania with tantala in a double-layer ARC structure with SiO₂ and tuning the thicknesses of the layers should result in comparable results for the previous designs. As it happens, that is not the case with IBS deposited Ta₂O₅, as is shown in the LIV-results measured for a triple-junction GaInP/GaAs/GaInNAsSb MJSC in **Figure 28**.

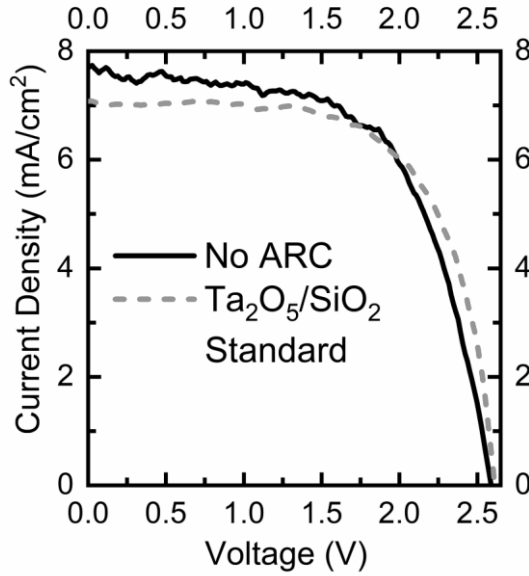


Figure 28 LIV for a bare GaInP/GaAs/GaInNAsSb MJSC and with Ta₂O₅/SiO₂ ARC deposited with standard parameters.

The MJSC with Ta₂O₅/SiO₂ ARC yields significantly lower current density than the same solar cell without a coating. The short-circuit current density J_{sc} decreases from 7.6 mA/cm² to 7.1 mA/cm² which is in contradiction of the improved reflectance shown in P2. The fact that the V_{oc} remains unaltered (2.6 V) points mainly to increased recombination losses in the window layer, instead of other loss mechanisms.

As all the optical qualities of the coating were good and did not provide an explanation for such a catastrophic performance deterioration, an ARC test series for PL measurements were deposited on two kinds of MJSCs, GaInP/GaAs/GaInNAsSb and AlGaAs/GaAs/GaInNAsSb. The series altered the IBS deposition parameters for Ta₂O₅ linearly with a multiplier coefficient f , as is shown in **Table 3**.

Table 3 Sputtering parameters for the Ta₂O₅ test series. Parameter f denotes the linear scaling coefficient for the three ion source parameters.

f	Primary Source RF Power [W]	Beam Current [mA]	Beam Voltage [V]
1	145	225	2000
0.7	102	158	1400
0.6	87	135	1200
0.5	73	113	1000

The topmost layer of the MJSC structure, the window layer, was different for the two MJSC designs: AlInP for GaInP top junction and AlGaAs for AlGaAs top junction. The results of the PL measurements are shown in **Figure 29**. Excitation with 532 nm is used to probe the topmost junctions. The CW mode mainly generates signal from the very topmost part of the junction, whereas Q-switched excitation enables signal contribution from deeper in the junction. The middle-junction GaAs was probed with 785 nm CW excitation.

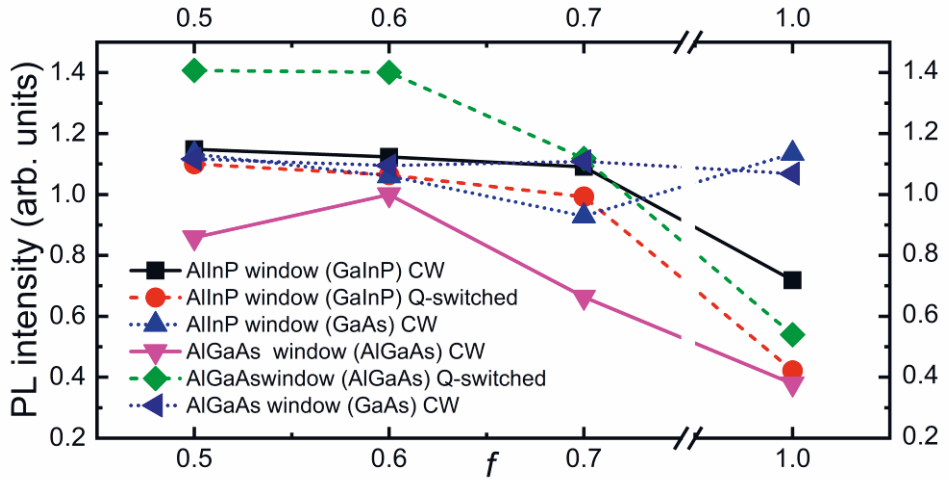


Figure 29 The reflectance corrected normalized photoluminescence intensities for Ta_2O_5 parametrizations [P2].

The PL measurements show that the standard sputtering parameters for Ta_2O_5 degrade the material quality of both MJSCs with AlInP or AlGaAs, which explains the poor LIV performance in **Figure 28**. The top junctions seem to take most of the damage with the standard parameters ($f = 1$) as the GaAs signal remains above 1, when the PL of the top junctions reach as low as 0.4. As the sputtering parameters are reduced by $f = 0.7$, AlInP window MJSC has already significantly improved surface PL when compared to the standard parameters. For AlGaAs MJSC the surface PL is just slightly improved. At $f = 0.6$ all the PL signals are above 1 indicating unharmed deposition of Ta_2O_5 in respect of the MJSCs. For $f = 0.5$, however, the signal from AlGaAs top junction is reduced for CW excitation. All the other signals are slightly better or the same than with the parametrization $f = 0.6$. The overall trend seems to be that the PL intensities improve as the sputtering parameters are reduced. Only contradiction to this is the drop of the AlGaAs PL intensity from $f = 0.6$ to $f = 0.5$. As the Q-switched signal is still relatively high (~ 1.4), the signal drop of AlGaAs might be related to an oxidation of the AlGaAs

window layer. This could also explain why the signal for AlInP window structure is further improved, as AlInP does not oxidate similarly than AlGaAs [39].

In addition to the possible oxidation causing reduced performance, it is clear that the standard deposition parameters damage both of the window materials. Possible mechanisms are unintentional sputtering of the III–V surface by the scattered primary projectiles (Ar^+) or the sputtered molecules (TaO), ion implantation of the scattered Ar^+ ions, and crystal defects induced by collision cascades. To investigate the first one, we calculated the maximum kinetic energies of the sputtered TaO particles (E_{spu}) and the scattered argon ions (E_{sca}) as a function of the primary ion energy (E_{proj}) shown in **Figure 30 a**). Both particle species seem to have enough energy at the higher parametrizations ($f = 1, 0.7$) to cause secondary sputtering.

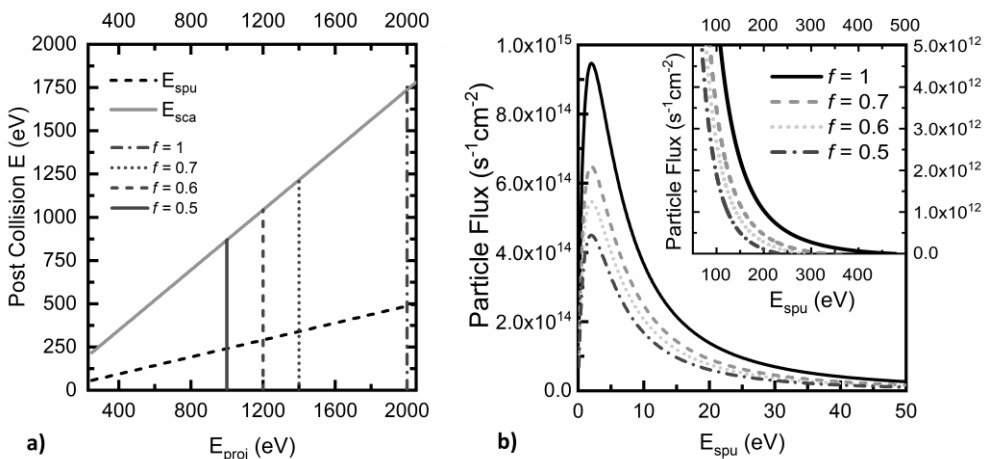


Figure 30 a) Particle energies for scattered Ar^+ -ions and sputtered TaO particles as a function of the initial energy of the projectile Ar^+ -ions. b) Calculated TaO particle fluxes as a function of their kinetic energy. [P2]

In order to get a clearer picture of the number of the high energetic particles, we calculated the fluxes of the sputtered TaO particles as a function of the particle energy, both in low energy region (≤ 50 eV) and in high energy region (≥ 50 eV).

The calculated TaO fluxes are shown in **Figure 30 b)**. Most TaO particles have less than 50 eV kinetic energy to begin with and on their way to the substrate they lose much of that due to collisions with the background gas particles [190]. On average, a sputtered TaO particle collides approximately 4 times with oxygen molecules before reaching the semiconductor surface. In comparison a scattered Ar⁺ ion undergoes only ~2 collisions. The collisions have been calculated for oxygen atmosphere, where other gas species have not been considered. In this sense, the post-collision energies shown in **Figure 30 a)** and **b)** are the absolute upper limits for projectiles arriving at the substrates.

For estimating the possible secondary sputtering at the semiconductor surface, we need to know the surface binding energies (U_{sb}) of the sputtered material to calculate the sputtering thresholds (E_{th}) for the projectile-target pairs. The U_{sb} values in this work are directly from Seah [113] and Malherbe [119]. The calculated E_{th} values for the normal incidence [112] and for the oblique angle [114] are shown in **Table 4**.

Table 4 Calculated sputtering thresholds for Ta₂O₅, GaAs, AlGaAs and AlInP.

Sputtering Threshold [eV]							
Target material	Ta ₂ O ₅	GaAs		AlGaAs		AlInP	
Projectile	Ar ⁺	Ar ⁺	TaO	Ar ⁺	TaO	Ar ⁺	TaO
E_{th}^{normal}	19	14	41	16	49	23	77
$E_{th}^{oblique}$	14	8	19	9	22	16	24

The sputtering thresholds at oblique angles are significantly lower than at the normal incidence as a larger fraction of the particle energy is deposited near surface [116]. Projectiles with less energy than the sputtering threshold of the material do not contribute to the sputtering process. The higher sputtering threshold energies for TaO particles indicate smaller yields compared to Ar⁺. In contrast, the sputtering threshold energies with Ar⁺ are about ~10 eV smaller than for TaO. The number of scattered Ar⁺ ions can be significant and their high-energy counts can be ten times of the counts for high-energy sputtered species [191], [192], which would favor sputtering by the Ar⁺ ions compared to TaO particles. The calculated sputtering yields for GaAs, AlGaAs, and AlInP with Ar⁺ are shown in **Figure 31 a)** and with TaO particles in **Figure 31 b)**.

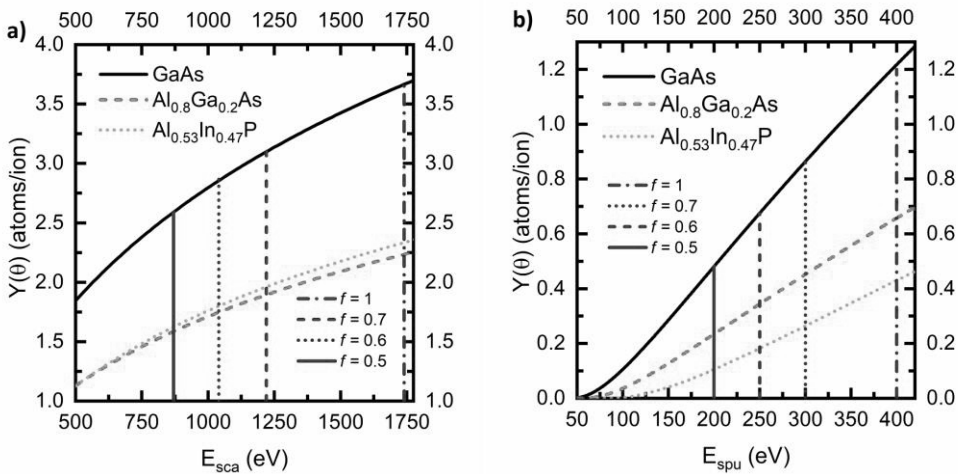


Figure 31 a) Calculated sputtering yields for GaAs, AlGaAs and AlInP by the scattered Ar⁺ ions at 50° incidence. b) Calculated sputtering yields for GaAs, AlGaAs and AlInP by the primary TaO particles at 50° incidence [Adapted from P2].

As the angular sputtering yields are not well defined with the projectile energies below and near the threshold energy of the target materials [114], we show the

calculated yields for TaO sputtering at $E_{\text{sput}} \geq 50$ eV, which is well above the calculated sputtering thresholds for oblique angles in **Table 4**. We see that the sputtering yields follow the sputtering threshold energies i.e., the lowest threshold material (GaAs) has the highest yield and so forth. Also, the yields with Ar-projectiles are nearly three times higher than the yields by TaO particles with the same parametrization. This combined with the thermalization losses that the TaO particles experience on their way from target to samples [190] makes it more likely that the damage for the semiconductors is due to the scattered Ar^+ ions. The differences in PL results with the parametrization are not directly explained by the sputtering yields as both AlInP and AlGaAs follow similar trend between $f = 1$ and $f = 0.5$. It is likely that the surface oxidation of AlGaAs plays a major role in the discrepancies between the two window materials [37], [38].

To test the outcome for the optimization of sputtering Ta_2O_5 , we deposited the same $\text{Ta}_2\text{O}_5/\text{SiO}_2$ ARC on the same GaInP/GaAs/GaInNAsSb MJSC structure than in **Figure 28** and measured its LIV performance. Only this time, we used parameters given by $f = 0.6$. The resulting LIV curves before and after ARC deposition are shown in **Figure 32**.

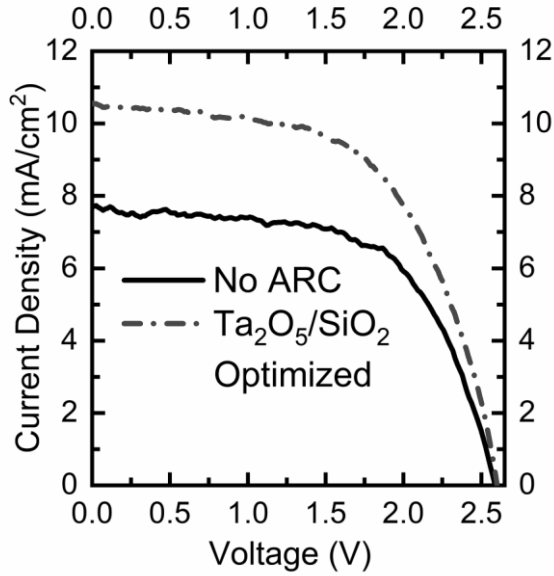


Figure 32 LIV of a bare GaInP/GaAs/GaInNAsSb and with optimized ($f = 0.6$) Ta₂O₅/SiO₂ ARC.

The optimized ARC leads to a significant enhancement in the short-circuit current density from 7.6 mA/cm² to 10.5 mA/cm² (~40%) and shows no clear evidence of sputtering induced damage. Also, the open-circuit voltage of the MJSC remains unchanged (2.6 V). This proves that the linear parameter optimization is useful in reducing the deposition induced damage to the MJSC.

In conclusion, the standard deposition parameters damaged the MJSCs leading to reduced PL intensities and to a significant drop in the short-circuit current density. The optimization by linearly scaling the three main parameters of the ion source, namely RF power, ion beam current, and beam voltage mitigated the process induced damage. This enables using IBS deposited Ta₂O₅ as a part of ML ARC for MJSC. As the main damage mechanism was evaluated to be the scattered Ar⁺ ions, it is

necessary to utilize similar optimization for any IBS deposited materials for III–V MJSCs.

4.3 Utilizing Nanostructured Alumina Coatings

Our approach for utilizing nanostructured antireflection coating on MJSC comprised three subsequential phases. First, the concept of designing and fabricating ML ARC with the DIW treated nanostructured alumina top layer was tested and verified. Secondly, the ARC performance on 4-junction MJSCs was tested and its optical properties and functionality were characterized. Thirdly, the durability of the alumina nanostructure was put under test with atmospheric icing conditions at TAU Ice Laboratory. The following subchapters describe these phases in more detail.

4.3.1 Achieving Broadband Antireflection

The nanostructured alumina on its own is not enough to provide low reflectance over a broadband spectrum for a semiconductor surface, as can be seen in **Figure 33**. For glass it is sufficient, especially if the substrate is coated on both sides, but the large refractive index contrast between alumina and air prevents continuous gradual index change from the substrate to the incident medium.

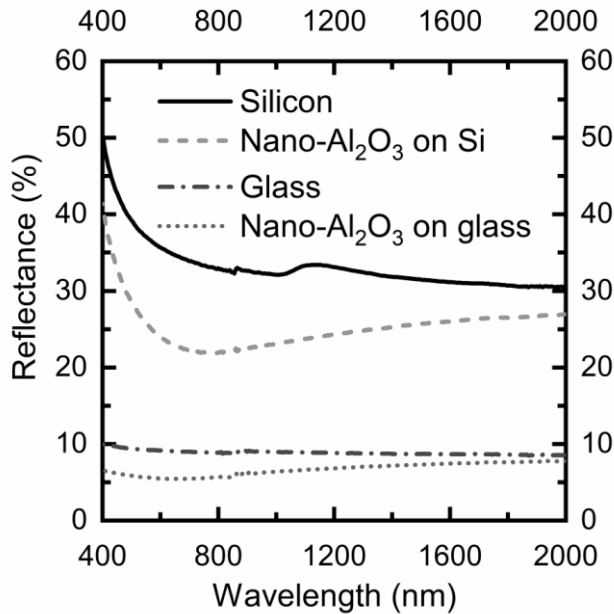


Figure 33 Measured reflectance of bare glass, bare silicon, and both with a nanostructured alumina layer on them.

To utilize the alumina nanostructure in MJSC ARC, it needs to be combined with underlying planar layers that can match the index gap between alumina and the MJSC. For this, the other materials used in the ARC design must be able to withstand the DIW treatment without similar structural alterations that are evident for the amorphous alumina. The other layer materials preferably need to be deposited in the same run with the Al₂O₃ to prevent unnecessary processing steps and to avoid possible contamination risk jeopardizing adhesion between the layers. In our case, the available deposition methods and materials included variable oxides by e-beam and IBS. As the nanostructuring process for Al₂O₃ had been tested only with atomic layer deposition and magnetron sputtering grown films in the literature [92], [93], also alumina was included in the material test set. The oxides were deposited on silicon wafer pieces and treated afterwards with the heated DIW bath. The refractive

indices at $\lambda = 632.8$ nm and the physical thickness of the deposited films were measured prior and after the DIW treatment to quantify any notable changes in the films. The ellipsometry results are shown in **Table 5**.

Table 5 A comparison of refractive index at $\lambda = 632.8$ nm and thickness changes before and after DIW treatment for various IBS and e-beam oxide materials.

		Material	Before DIW	After DIW	Δ [%]
IBS	<i>n</i> (@633nm)	Al ₂ O ₃	1.671	N/A	N/A
			1217	N/A	N/A
	Thick. [Å]	SiO ₂	1.483	1.481	-0.2
			1025	1014	-1.1
		TiO ₂	2.372	2.370	-0.1
			1046	1043	-0.3
		Ta ₂ O ₅	2.110	2.109	-0.1
			743	740	-0.4
E-beam	<i>n</i> (@633nm)	Al ₂ O ₃	1.583	N/A	N/A
			1245	N/A	N/A
	Thick. [Å]	SiO ₂	1.449	1.444	-0.3
			907	875	-3.5
		TiO ₂	2.177	2.170	-0.3
			514	510	-0.7
		Ta ₂ O ₅	1.948	1.930	-0.9
			632	630	-0.3

As expected, both IBS and e-beam deposited alumina are unmeasurable by the monochromatic ellipsometer after the DIW treatment. This indicates inhomogeneous layer structure caused by morphological changes in the alumina surface. Rest of the tested oxide materials show no significant changes either in the

refractive index or in the film thickness by the DIW process. Based on this, utilization of nanostructured alumina on ML ARC made of these oxides is possible.

To study the microstructural changes in the alumina films, they were imaged with SEM and AFM before and after the DIW treatment. **Figure 34** shows the imaged surfaces.

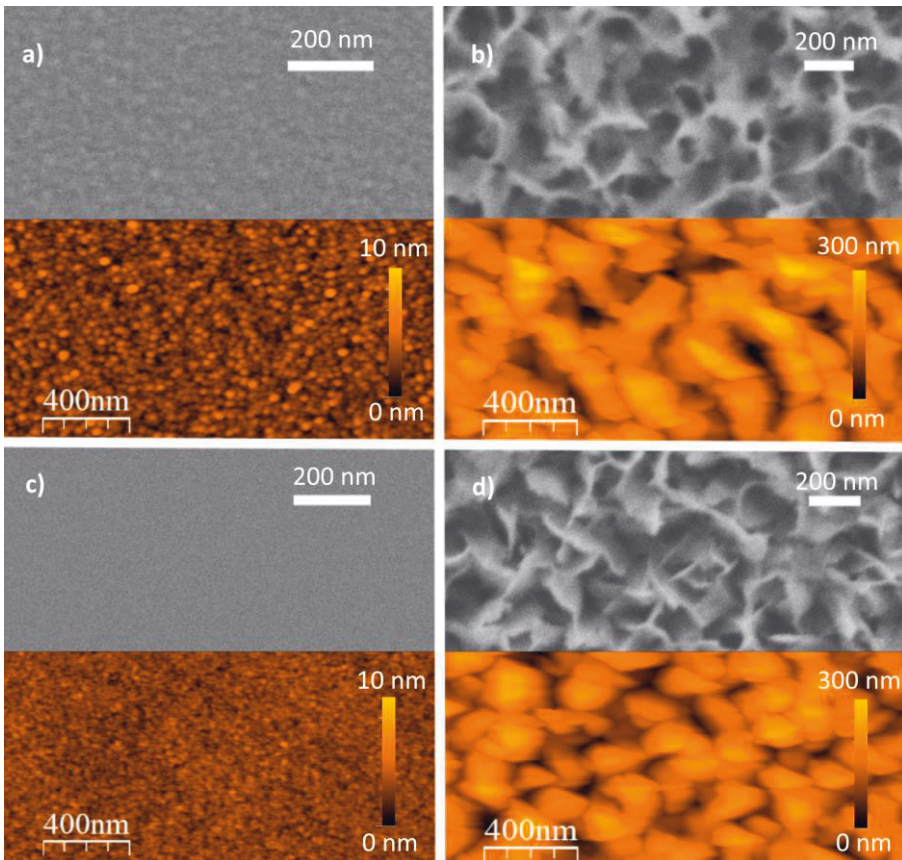


Figure 34 Microstructure of alumina surfaces, as a) e-beam as-deposited, b) e-beam DIW treated, c) IBS as-deposited, and d) IBS DIW treated. The top part of each frame is a SEM micrograph of the coating surface, and the lower part is the corresponding AFM surface scan [Adapted from P3].

Prior the DIW treatment, both e-beam and IBS deposited films are smooth. After the DIW treatment the alumina films have formed porous nanostructure which is in line with similar studies done for alumina deposited by other methods [92], [93], [193], [194]. The numerical roughness values for the films presented in **Figure 34** are shown in **Table 6**.

Table 6 Surface roughness of alumina films before and after the DIW treatment measured by AFM.

	E-Beam		IBS	
	Untreated	DIW	Untreated	DIW
R_{rms} [nm]	0.86	41.09	0.13	42.10
R_{ave} [nm]	0.68	33.01	0.10	34.54
Average height [nm]	2.69	161.83	0.68	135.20
Max height [nm]	7.55	303.35	1.36	257.99

E-beam deposited alumina is a bit rougher to begin with than the IBS deposited film. Difference in R_{rms} is ~ 0.7 nm, which is still very little but indicates that the e-beam Al_2O_3 might be slightly porous to begin with. This would explain the difference in the height distribution of the pores of DIW treated samples in between the e-beam and IBS deposited films, which is on average ~ 30 nm. A bit different structure profile between the nanostructures deposited with the two methods, will lead to different optical properties, as was shown in P3.

When the physical height profile information of the nanostructure is combined with the measured optical properties, like $T\%$ and $R\%$, the interference properties of the nanostructure can be estimated with a fitted rugate approximation. The principle of the rugate approach, shown in **Figure 35 a)**, is practically to mimic the gradual refractive index change of the nanostructure with a large number of individual layers whose refractive indices are scaled according to the Maxwell-Garnett approximations [103], [195]. Being able to simulate the nanostructure in TMM calculations enables using the nanostructure as a part of new simulated coating structures. This way potential ARCs can be numerically evaluated and optimized prior fabrication.

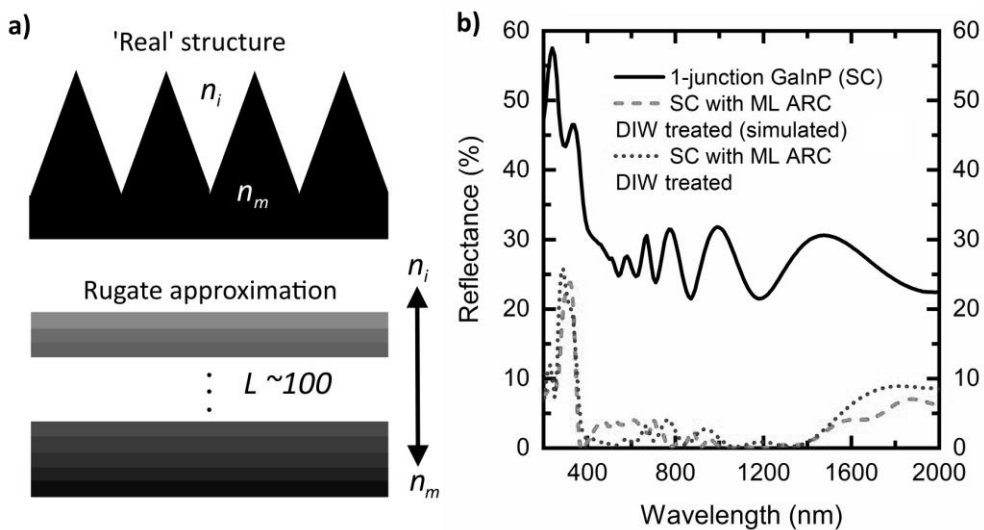


Figure 35 a) The principle of the rugate approximation used to simulate the nanostructured alumina. b) Reflectance comparison of a simulated ARC with nanostructured alumina top layer and an actual reflectance of the said coating on GaInP solar cell [Adapted from P3].

To test the effectiveness of the generated rugate design in ARC optimization, we designed and fabricated a ML ARC with nano-alumina layer on top on a GaInP single-junction solar cell and compared the simulated and measured reflectance. The

comparison is shown in **Figure 35** b) and the fit for the nano-ARC is good. It correctly shows the locations and magnitudes of the reflectance minima and the trends of reflectance for the whole broadband spectrum (200-2000 nm). The total average reflectance from 300 to 1800 nm is excellent 3.2%, which surpasses all the achievable minimum average reflections for planar coatings calculated with Eq. 3 by almost 10 percentage point.

A nanostructured alumina top layer combined with underlying oxide ML ARC seems to be a feasible approach for broadband MJSC ARC by the utilization of the DIW treatment. It is possible to accurately simulate the nanostructure with a rugate approximation for further design optimization and the approach provides broadband reflectance reduction.

4.3.2 Nano-ARC Performance on Multijunction Solar Cells

Demonstrated functionality on glass, silicon, and a single-junction GaInP is a good step forward in realizing a broadband ML ARC for MJSC with the alumina nanostructure (nano-ARC). Work of P3 presented in the previous subchapter provided necessary design and fabrication tools for further testing the nano-ARC at oblique angles and on four-junction MJSC. In **Figure 36** a) is presented a cross-sectional surface scan of the nanostructured alumina, and b) and c) show the schematics and an actual cross-section of the complete ML nano-ARC, respectively.

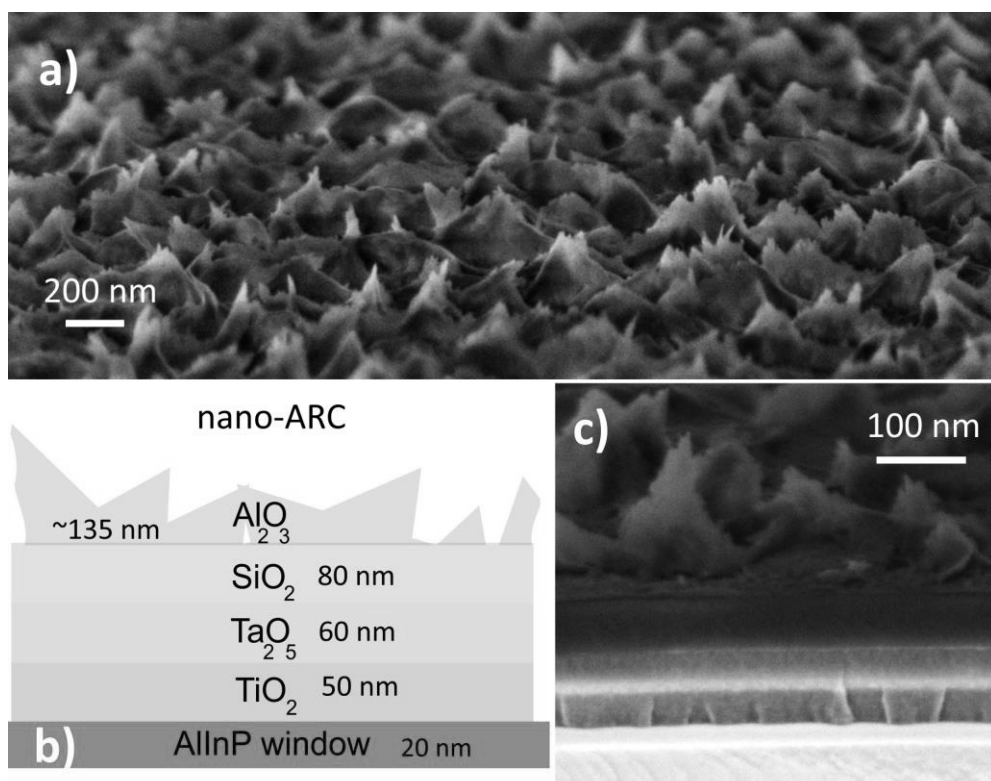


Figure 36 a) A SEM surface scan of the nano-ARC, b) a schematic illustration of its structure, and c) a cross-sectional scanning electron micrograph of the nanostructured coating. [P4]

Instead of the calculational average given by Eq. 3, we compare the performance of the nano-ARC on MJSC to a conventional planar double-layer $\text{TiO}_2/\text{SiO}_2$. This double-layer ARC has originally been optimized for GaInP/GaAs/GaInNAsSb triple-junction MJSC [77], to prevent the top-junction (GaInP) becoming the current-limiting junction. Its nominal structure is 50 nm TiO_2 / 89 nm SiO_2 . It exhibits relatively broadband low reflectivity at 400 –1000 nm and with the given materials represents a robust and realistic optimal double-layer ARC for these III–V MJSCs.

As nanostructured top layer should provide angle-independent reflectance reduction [60], [196], the ARCs were first deposited on single-junction GaInP solar cells for angle-dependent EQE measurements. The EQE results are presented in **Figure 37**. **Figure 37 a)** shows that the nano-ARC practically retains its ARC properties almost fully even at incidence angles of 45° and 60° . The calculated difference in the short-circuit current density between the normal incidence and 60° is just 0.4 mA/cm^2 . At normal incidence the nano-ARC works in a similar manner to the planar double-layer ARC, as is shown in **Figure 37 b)**, and they result in the same short-circuit current density. At 45° the short-circuit current density of the double-layer ARC begins to drop while the nano-ARC remains the same as at the normal incidence. At 60° the calculated difference in the short-circuit current density is already 1.0 mA/cm^2 for the double-layer ARC when compared to the normal incidence angle. Angle-dependent EQE measurements demonstrate in practice an angle-independent operation for the nano-ARC.

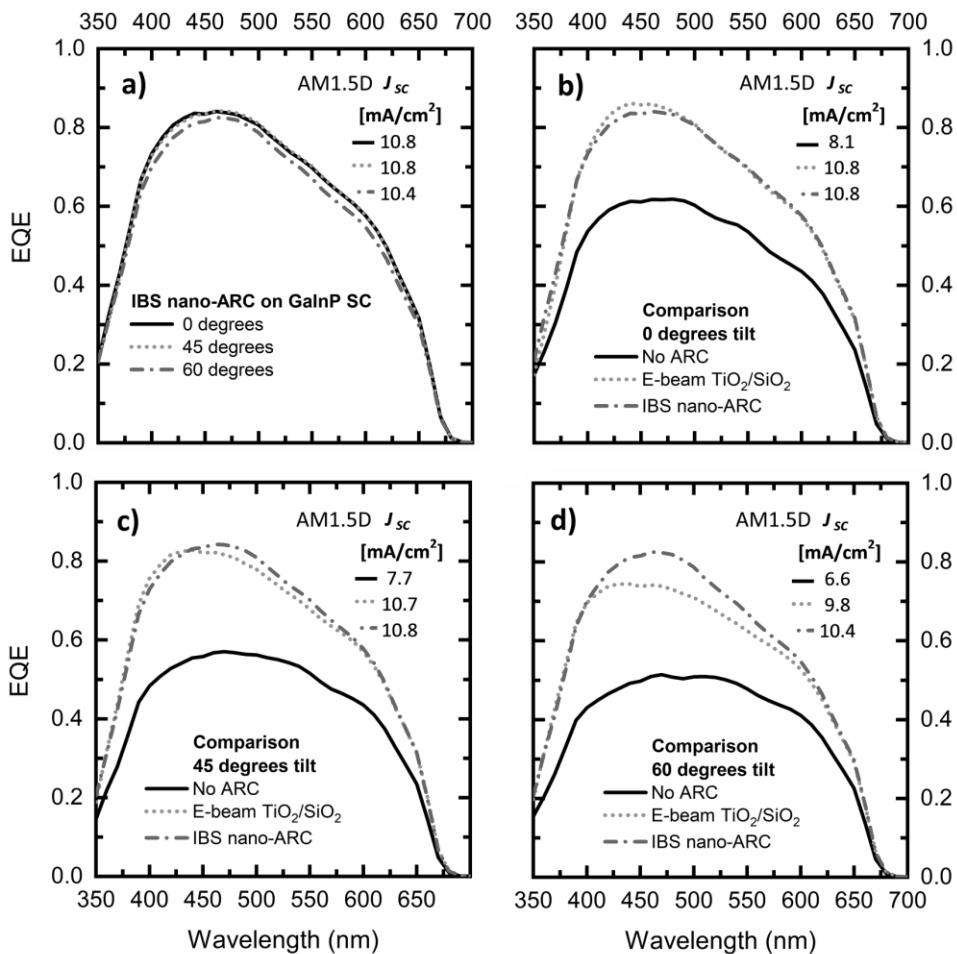


Figure 37 a) Measured angle-dependent EQEs for the single-junction GaInP solar cells coated with the nano-ARC at the angles of 0°, 45° and 60°, demonstrating nearly unchanged performance as a function of the incidence angle. b)-d) comparison of single-junction GaInP solar cell EQEs without an ARC, with the e-beam ARC and with the nano-ARC at the angles of 0°, 45° and 60°, respectively. For each of the measured EQEs the corresponding current density under AM1.5D (1000 W/m²) spectrum has been calculated and is shown in the inset tables on the right upper corner of each sub-plot. [P4]

To prove the effectiveness of the nano-ARC also on an actual MJSC structure, the ARCs were compared on GaInP/GaAs/GaInNAsSb/GaInNAsSb SCs. The effect of a more complex MJSC structure with additional junctions shows in the number of interference fringes in the MJSC reflectance. This complexity makes it challenging to design a balanced broadband ARC to spectrally fit the sub-cell current-matching requirements [33], [143], as the average reflectance plays a smaller role than the sub-cell bandwidths or the MJSC overall design. **Figure 38** a) shows the reflectance comparison on the GaInP/GaAs/GaInNAsSb/GaInNAsSb MJSC and **Figure 38** b) presents the LIV characterizations.

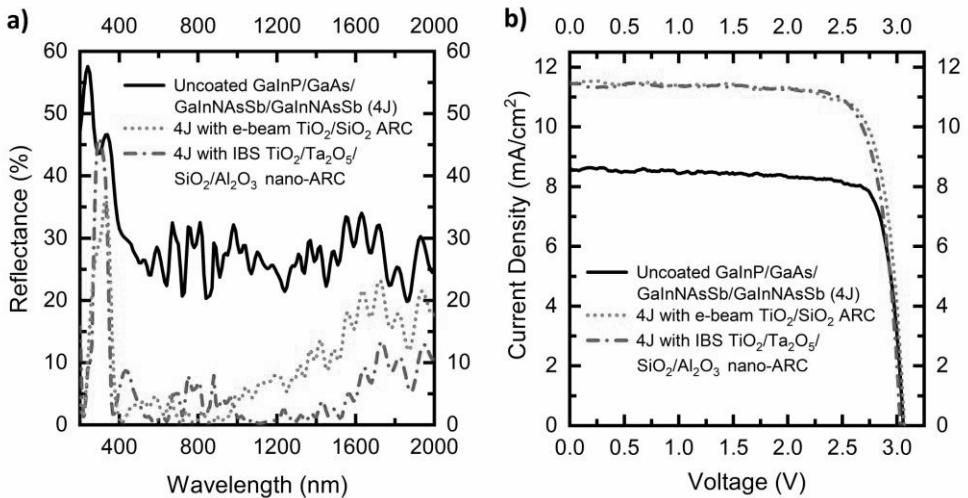


Figure 38 a) The reflectance of an uncoated GaInP/GaAs/GaInNAsSb/GaInNAsSb solar cell (4J), with the conventional e-beam double-layer ARC and with the nano-ARC. b) The measured LIV characteristics under AM1.5D (1000 W/m²) for the 4J solar cells without a coating, with the e-beam double-layer ARC and with the nano-ARC. [Adapted from P4]

The total average reflectance of the nano-ARC is lower than the planar ARC, especially at the wavelengths 1000-1800 nm, where the average reflection for nano-ARC is as low as 3.5%, which is 8.1 percentage points less than with the double-layer

ARC. However, the poorer performance at the GaInP and GaAs bandwidths might lead to reduced effectiveness in the LIV results. In a case of either of the top sub-cells being slightly too thin and having such high reflectance at its bandwidth, the possibility of the top cell becoming the current limiting junction in the structure increases. The LIV shown in **Figure 38 b)** indicates that the short-comings of the nano-ARC at the GaInP and GaAs bandwidths are not too severe, as the behavior compared to the planar double-layer ARC is very similar. Numerical comparison of V_{oc} , J_{sc} , and η shown in **Table 7** indicates that the nano-ARC should be improved at the shorter wavelengths, as it performs slightly worse than the double-layer structure, which implies that either GaInP or GaAs junction would already be a limiting subcell. Reflectance reduction at the longer IR wavelengths for low band gap materials then again is already excellent.

Table 7 Measured LIV –characteristics as conversion efficiency η , open-circuit voltage V_{oc} , short-circuit current density J_{sc} , and fill factor FF under AM1.5D (1000 W/m²) for the MJSCs as bare, with planar e-beam ARC and with the nano-ARC.

	Uncoated	E-beam TiO ₂ /SiO ₂	IBS TiO ₂ /Ta ₂ O ₅ /SiO ₂ /Al ₂ O ₃ nano-ARC
η [%]	21.2	27.6	27.4
V_{oc} [V]	3.1	3.1	3.0
J_{sc} [mA/cm ²]	8.6	11.5	11.4
FF [%]	81.0	78.4	79.2

Although the nano-ARC had a non-optimal reflectance at the GaInP and GaAs bandwidths, the nano-ARC coated MJSC was still a functional device and no

significant difference in the electrical performance compared to the planar coated MJSC was observed. This would suggest that using nanostructured alumina ML ARC is suitable for high efficiency MJSCs. The limitations of the nano-ARC can be overcome with optimizing the Al_2O_3 nanostructure by tuning the DIW process parameters [94] and by altering the planar layer thicknesses in the multilayer configuration. The tested nanostructure was not spectrally optimized, as mainly the suitability of the method for a real MJSC device was under inspection.

4.3.3 Improving Environmental and Temporal Stability

Durability requires that the coating needs to be able to withstand both time and environmental effects. As the alumina nanostructure is processed basically with just heat and water, which both are abundant within regular operation condition of photovoltaics; heat via unconverted solar energy and water via humidity in air, there is a question if the nano-ARC can fulfill this expectation. SEM scans shown in **Figure 39** prove that in its initial condition it cannot.

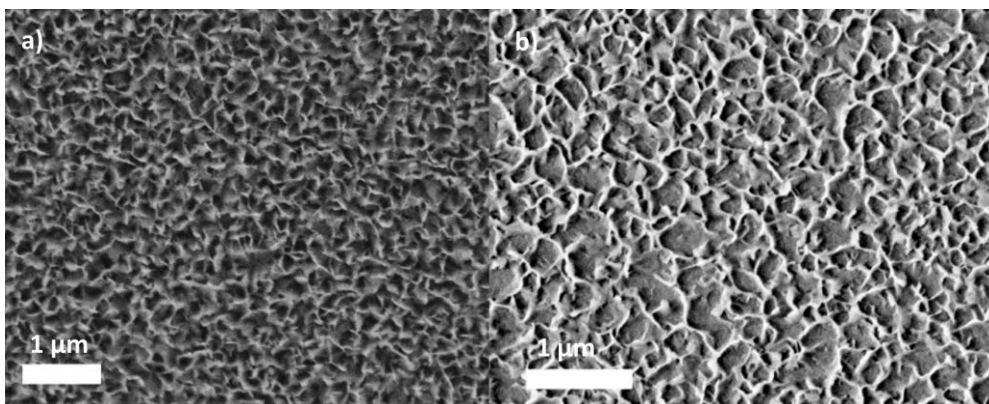


Figure 39 a) The surface of a nano-alumina ARC shortly after the deposition. b) The same nano-alumina ARC after a year-long exposure to atmospheric conditions.

In **Figure 39 a)** the just-deposited alumina nanostructure is densely packed and sharply featured. In **Figure 39 b)** the same surface after a year-long exposure to measurement conditions and storage has worn out some of the nanostructure and dulled the previously sharp features. Such a drastic structural change leads into poorer optical performance and reduced LIV results and makes using a bare nano-ARC a non-viable option for high efficiency MJSCs. A possible workaround is to add a surface-energy reducing polymer-layer to provide hydrophobicity in the coating, which would prevent the evident structural changes [129]–[131], [133], [135], [136].

To this end, we fabricated an environmental test series of alumina coatings on glass and silicon. The series included nanostructured alumina films with and without a hydrophobicity treatment and, as a comparison, planar alumina films. The coating types are referred as Plano for planar alumina, Nano for nanostructured alumina, and Fluoro for nanostructured and hydrophobicity treated alumina films. The films were characterized after fabrication and exposed to atmospheric icing conditions with a sequential CAT testing that can be seen as a harsh and rapid ice removal stress test for the coatings. After the CAT the films were re-characterized to quantify the changes in the films.

The CA measurements shown in **Figure 40 a)** indicate that Plano alumina on both surfaces is hydrophilic in nature ($SCA < 90^\circ$) [167]. Similarly, the Nano coatings are superhydrophilic, as the droplets spread out on the surface immediately [168]. Fluoro exhibits hydrophobicity ($SCA \sim 130^\circ$), but not superhydrophobicity. This probably could be improved by using different process parameters, like longer process time, as similar treatment has produced superhydrophobic nano-alumina [95]. In overall, the coating performance is very similar between the two substrate materials.

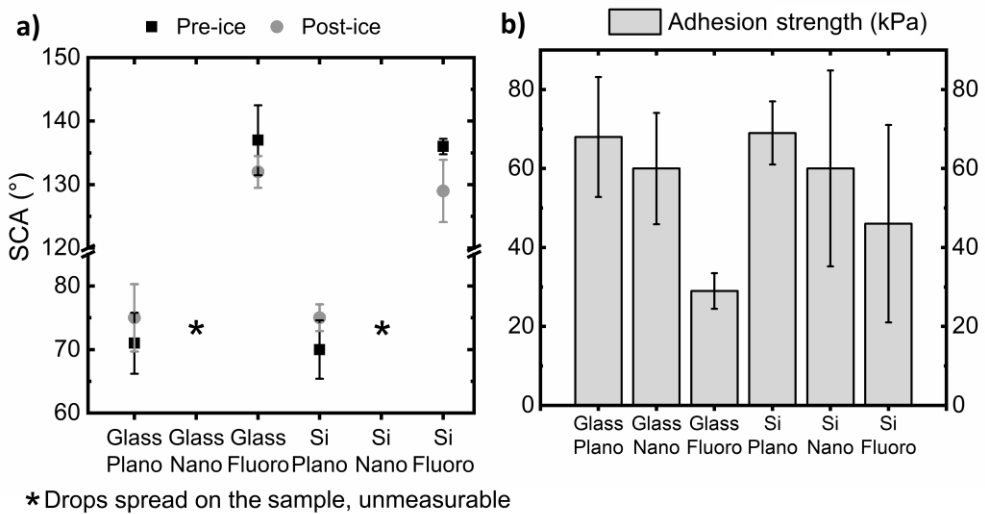


Figure 40 a) SCAs for the Plano, Nano and Fluoro prior icing and after ice adhesion test. b) Ice adhesion values for the centrifugal adhesion test. [Adapted from P5]

The ice adhesion strengths measured with CAT are shown in **Figure 40 b)**. The adhesion of ice to the alumina coatings seems to be independent of the substrate material, which suggests similar growth and nanostructuring process for the alumina coatings on both substrates. Both Plano and Nano coatings have ice adhesion values that correspond to the medium-low adhesion region, given in **Error! Reference source not found.**, 70 kPa and 60 kPa, respectively. The ice adhesion strength on Fluoro is significantly lower and reach the low adhesion region. For Fluoro on glass and on silicon the ice adhesion strengths are 29 kPa and 46 kPa, respectively. When compared to many other anti-icing coatings that have values between 50 kPa to over 100 kPa [129], [131], [132], [134], [197], the low ice adhesion strength on Fluoro is excellent. Also, the post-CAT CAs shown in **Figure 40 a)** have changed only small degradation ($\sim 5^\circ$) which should indicate increased mechanical durability.

As the optical performance of an ARC should remain unchanged due time the changes in average transmittance and reflectance due icing and CAT were measured with spectrophotometer. The transmittance of the alumina coatings on glass are presented in **Figure 41 a)** and similarly the reflectance on silicon in **Figure 41 b)**.

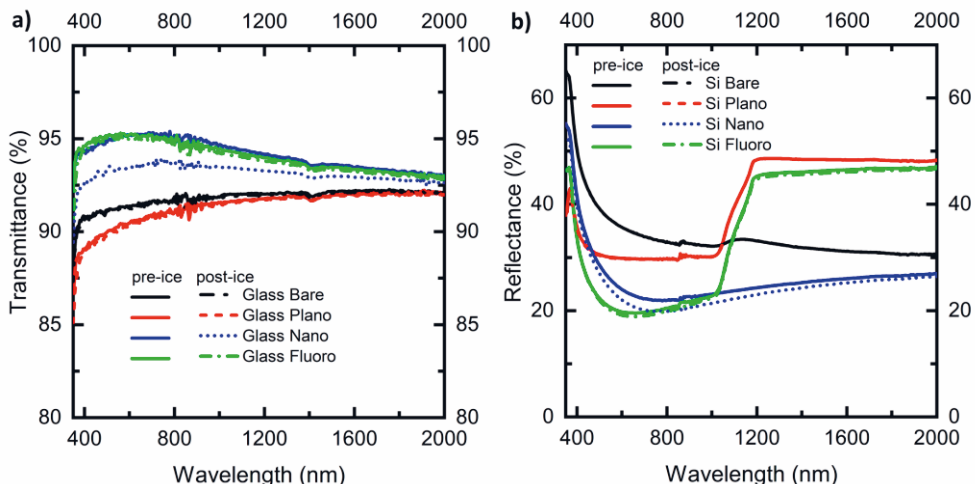


Figure 41 a) Transmittance of Plano, Nano and Fluoro on glass. b) Reflectance of Plano, Nano and Fluoro on silicon. [Adapted from P5]

The bare substrates presented in **Figure 41** were not iced and are presented only as reference. The average pre-ice transmittance over the bandwidth of 400 nm to 800 nm for Plano, Nano, and Fluoro on glass are 90.4%, 95.0%, and 95.1%, respectively. Compared to many other hydrophobic anti-icing coatings the presented transmittance of $\sim 95\%$ is excellent, as the reported transparencies are usually reduced $\sim 1\text{-}10\%$ from the bare glass transmittance at similar bandwidths [130], [131], [135], [197]. A comparison with the reflectance in P5, also shows that there are also no losses involved in the alumina coatings, as $T\%$ and $R\%$ on glass sum up to 100%. Only Nano has been significantly influenced by the icing, as its transmittance has reduced. Presumably the icing has altered the nanostructure. The

biggest effect on Nano is at the visible wavelengths, where the change in transmittance is on average 1.6% reduction. As it comes to the reflectance of alumina on silicon, there is apparently also backside reflectance included for Plano and Fluoro samples, which can be seen as a discrete increase of $R\%$ below the silicon bandgap ($E_g \sim 1.1$ eV). Like on glass, only Nano has had notable changes between pre- and post-ice reflectance. The reflectance has dropped 1.8% at 400-800 nm, which would indicate changes in the nanostructure due to the icing procedure.

Presumably, Plano and Fluoro samples are mostly intact after icing and CAT, which was concluded by AFM in P5. Their roughness and surface topography changes were small. Nano coatings, however, had rather drastic changes, as are shown in **Figure 42**.

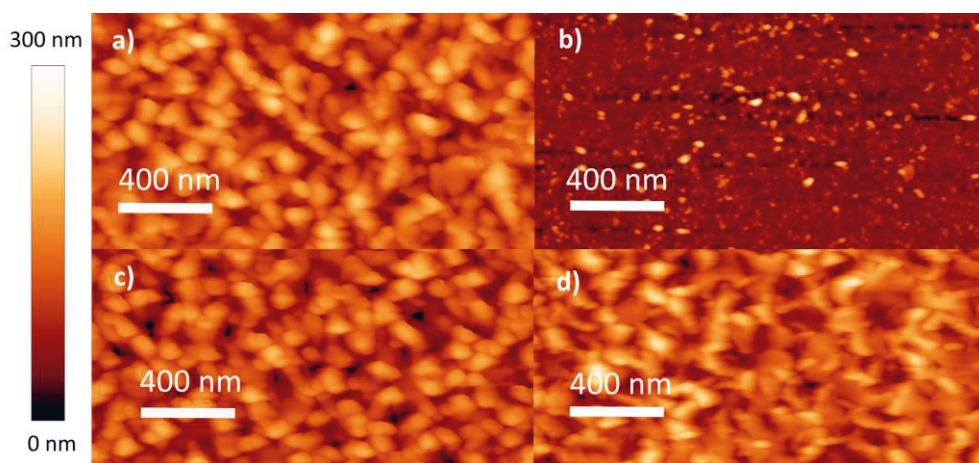


Figure 42 AFM scans for Nano on glass before a), and after b) ice adhesion test. AFM scans for Nano on silicon before c), and after d) ice adhesion test. [Adapted from P5]

It seems that Nano on glass has been ripped off with the ice during the adhesion test and only small islands with height of ~ 20 nm are still visible on the image. Surprisingly, Nano on silicon has not peeled off, but has maintained its

nanostructure. The features seem sharper in contrast than before icing and there is some increase in roughness values, but the nanostructure has not notably changed. Apparently, the adhesion of alumina on silicon is greater than the adhesion on glass, as the measured adhesion of ice on Nano on both substrates was basically the same (~ 60 kPa).

To get a wider overview of the surface features, the coatings on silicon were imaged in SEM. The pre-iced Plano, Nano, and Fluoro are presented in **Figure 43** a), b), and c), respectively. Similarly, the post-iced Plano, Nano, and Fluoro are presented in **Figure 43** d), e), and f), respectively.

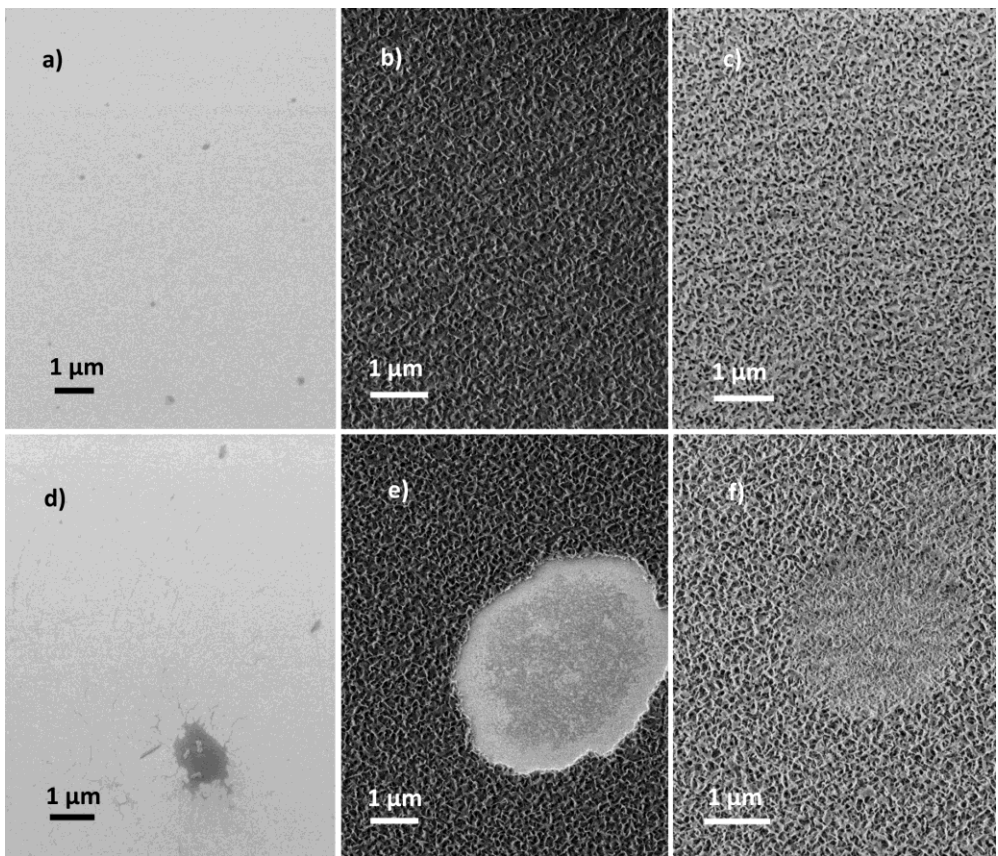


Figure 43 Scanning electron micrographs of alumina films on silicon. a)-c) show Plano, Nano and Fluoro surfaces pre-icing, respectively, and d)-f) show the same surfaces post-icing. [P5]

All three coatings, Plano, Nano, and Fluoro, are uniform before the icing and the adhesion testing. The contrast difference between Nano and Fluoro shows the thin fluoropolymer on the surface of Fluoro. Otherwise, the nanostructures are structurally very similar, as was indicated by the similarity in $T\%$ and $R\%$ spectra between Nano and Fluoro. Images taken after the CAT show that all three coatings have been negatively affected by the icing procedure. Plano shows micrometers wide areas where the coating has been ripped off and micro-cracks near such areas. Nano

has mainly the same structure than before the icing and the nanostructure seems to be unchanged, but there are large holes with diameters ranging from 1 μm to tens of micrometers of which the coating has completely peeled off the surface. It is likely that at the droplet impact stage the water drops have penetrated the coating [198], which combined with the freezing seemingly leads to permanent coating damage. Fluoro shows no such peeled-off areas, and the substrate is still uniformly coated with the film. There are visible dents very similar to the off-peeled areas on Nano, but the water droplet has not penetrated the surface and caused delamination of the coating after icing.

To further investigate the durability of Fluoro coatings they were exposed to four additional icing and melting cycles with Plano coatings as reference. The hydrophobicity was examined with subsequential CA measurements. Both static and dynamic CAs are presented in **Figure 44 a)** and the corresponding CA hysteresis is shown in **Figure 44 b)**.

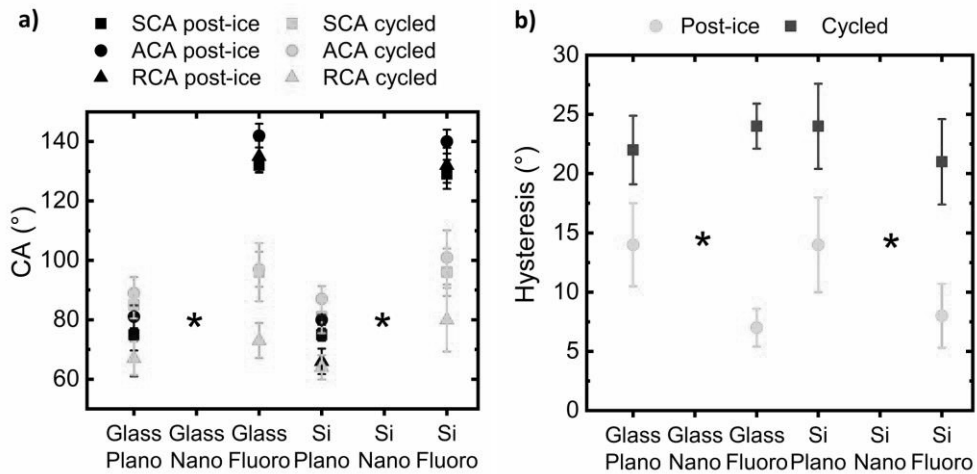


Figure 44 a) Contact angles after ice adhesion test and after four additional cycles of icing and melting the surfaces. b) Contact angle hysteresis after ice adhesion test and after four

additional cycles of icing and melting the surfaces. * Samples were not included in the additional icing-melting series. [P5]

The CA results after the cyclic icing and melting reveal that the hydrophobicity wears off for Fluoro samples whereas Plano surfaces have only small changes, most likely linked to the partial delamination seen in the SEM scans. This is in line with the similar cycling study in which several different anti-icing nanocoatings were tested and found to lose their hydrophobic performance due to the cycling [129]. The CA hysteresis in **Figure 44** b) shows that the difference between ACA and RCA stabilizes around $\sim 20^\circ$ for both planar and hydrophobic nanostructured samples.

Although the fluoropolymerization of nanostructured alumina did not offer long-term protection against icing, it makes the nano-ARC durable and effective in less harsh conditions than atmospheric icing. In the normal operating conditions of high efficiency MJSCs, the ARC remains under a cover glass or concentrating optics and would not be exposed to regular icing. The excellent transparency and extended durability when compared to the planar coating or only the nanostructured alumina shows the potential of fluoropolymerized nano-alumina for specialized broadband ARC solutions.

5 SUMMARY AND CONCLUSIONS

As the field of high efficiency III–V multijunction solar cells is continuously progressing to reach higher conversion efficiencies towards 50% and above, the requirements for any subpart of a solar cell gets stricter. This thesis aimed to contribute to the development of a practical broadband multilayer antireflection coatings for such high efficiency multijunction solar cells by improving the material properties of electron-beam deposited low refractive index MgF_2 and ion beam sputtered high refractive index Ta_2O_5 . In addition, it investigated the use of nanostructured Al_2O_3 top layer integrated into a multilayer antireflection coating. In the introduction

Table 1 summarized the main research questions for the publications of the thesis and the relevant aspects of each of the studies. **Table 8** included below summarizes the corresponding key results of each of the manuscripts.

Table 8 The key results for each of the publications of the thesis.

Key findings	
P1	<ul style="list-style-type: none">• The refractive index of e-beam deposited MgF_2 decreases as the deposition temperature increases.• The films are porous and affected by humidity due time, which will lead shifts in ARC performance. This process is partly reversable by heating in vacuum.• Deposition temperatures under 200 °C produce MgF_2 films that will crack due time.• RTA treatment was shown to improve the quality of MgF_2 films but utilization in ML structures requires further research.• DIW processing could be used also to produce nanostructured MgF_2.

- Standard reactive ion beam sputtering process of Ta₂O₅ damages the III–V MJSCs.
 - The root cause for the performance drop is caused by the high energetic scattered Ar⁺ ions.
- P2**
- The linear parametrization provided a functional tool for finding suitable deposition conditions of Ta₂O₅ on III–V MJSCs. The parametrization should be similarly done to other IBS deposited oxides for MJSCs.
 - Oxidation of the III–V surfaces in the reactive process should be considered prior coating.
- P3**
- Both e-beam evaporated, and IBS deposited oxides are suitable for the DIW ML ARC process, as only alumina is structurally altered by the process.
 - Structural characterization of nano-Al₂O₃ provided a functional basis for rugate modelling of ML ARCs with the nanostructure on top.
 - Numerical model yields a realistic evaluation of the ARC properties.
- P4**
- EQEs on GaInP single-junction SCs showed angle-independent reflectance reduction with the nano-ARC.
 - Electrical properties of the MJSC with nano-ARC were similar to the standard ARC process showing that the fabrication process of nano-ARC suits MJSCs.
 - In the long-wavelength range, 1000-1800 nm, the nano-ARC provided 3.5 percentage points average reflection that demonstrates its suitability for high efficiency MJSCs with 4 or more junctions.
- P5**
- Bare nano-alumina does not endure extended exposure to environmental conditions.
 - Hydrophobicity treatment provides protection against environmental strain.
 - Cyclic icing-melting gradually wears off the hydrophobicity of the treated nano-ARC.
 - Hydrophobic nano-ARC retains an excellent reflectance reduction after CAT and provides temporary protection even against atmospheric icing.

To conclude the practicality of the results and further development steps, annealing the e-beam deposited MgF_2 was not straightforwardly compatible with the multilayer antireflection coating approach and would require further research on the rapid thermal annealing process for multilayer structures. The de-ionized water treatment test for MgF_2 also showed another possible route for nanostructured surface that was not followed in the thesis.

For ion beam sputtered Ta_2O_5 , we managed to optimize the deposition process, enabling the use of Ta_2O_5 as a part of a multijunction solar cell antireflection coating. The numerical examination of the ion beam sputtering process also revealed the harmful energetic scattering of the projectile argon ions, that should be considered when coating III–V materials by ion beam sputtering. Also, the reactive oxygen process oxidizes the III–V surfaces that should be prevented for optimal results.

The de-ionized water treatment was suitable for multilayer oxide antireflection coating having alumina on top. The rugate approximation proved to be an efficient model for numerical simulation of the nanostructure which enables further design optimization for different multijunction solar cell configurations. The tested nano-ARC on a four-junction multijunction solar cell showed that the nano-ARC fabrication process is suitable for multijunction solar cells and does not generate significant additional losses. The last publication investigated the stability and durability of the nanostructured alumina with atmospheric icing tests and showed that a fluoropolymerization to induce hydrophobicity was necessary and beneficial for the stability of the nanostructured coating.

Finally, the carried-out work resulted in a practical, scalable, and broadband multilayer antireflection coating that is suitable for high efficiency III–V multijunction solar cells. A hydrophobicity treatment for the nanostructured alumina improved the temporal and environmental stability of the nanostructure beyond the performance exhibited by a planar alumina coating. In this light, we hope to see the developed nano-ARC in use with the future high efficiency multijunction solar cells,

as I believe there is potential to have additional benefits via this approach compared to other antireflection coating methods. The hydrophobicity treatment requires further development, as fluorine-based approaches have environmental consequences that should be avoided in more wide-scale approaches. Also, the presented nano-ARC was not specifically matched or optimized for any certain multijunction solar cell structure, which needs to be done in order to deliver the best possible performance.

6 BIBLIOGRAPHY

- [1] A. Macleod, “The early days of optical coatings,” *J. Opt. A Pure Appl. Opt.*, vol. 1, no. S, pp. 779–783, Dec. 1999, doi: 10.1088/1464-4258/1/S/305.
- [2] J. von Fraunhofer, “Versuche über die Ursachen des Anlaufens und Mattwerdens des Glases und die Mittel, denselben zuvorzukommen,” *Gesammelte Schriften*, 1888.
- [3] A. C. de Lega, “Coatings for ophthalmic lenses,” *Opt. News*, vol. 15, no. 7, p. 16, Jul. 1989, doi: 10.1364/ON.15.7.000016.
- [4] D. Ristau and T. Gross, “Ion beam sputter coatings for laser technology,” *Adv. Opt. Thin Film. II*, vol. 5963, p. 596313, 2005, doi: 10.1117/12.624772.
- [5] B. E. Yoldas and D. P. Partlow, “Wide spectrum antireflective coating for fused silica and other glasses,” *Appl. Opt.*, vol. 23, no. 9, pp. 1418–1424, 1984, doi: 10.1364/AO.23.001418.
- [6] D. T. Wei, “Ion beam interference coating for ultralow optical loss,” *Appl. Opt.*, vol. 28, no. 14, p. 2813, 1989, doi: 10.1364/ao.28.002813.
- [7] C. E. Valdivia *et al.*, “Optimization of antireflection coating design for multijunction solar cells and concentrator systems,” in *Photonics North 2008*, Jun. 2008, vol. PROCEEDING, no. November 2016, p. 709915, doi: 10.1117/12.807675.
- [8] M. Victoria, C. Domínguez, I. Antón, and G. Sala, “Antireflective coatings for multijunction solar cells under wide-angle ray bundles,” *Opt. Express*,

- vol. 20, no. 7, pp. 8136–8147, Nov. 2012, doi: 10.1364/OE.20.008136.
- [9] E. E. Perl, W. E. McMahon, J. E. Bowers, and D. J. Friedman, “Design of antireflective nanostructures and optical coatings for next-generation multijunction photovoltaic devices,” *Opt. Express*, vol. 22, no. S5, p. A1243, Aug. 2014, doi: 10.1364/OE.22.0A1243.
- [10] ResearchAndMarkets.com, “Global Optical Coating Market Analysis Report 2022-2030: Focus on Anti-reflective Coating, Reflective Coatings, Filter Coatings, Conductive Coatings, Electrochromic Coatings,” 2022. [Online]. Available: <https://www.researchandmarkets.com/reports/4808525/optical-coating-market-size-share-and-trends>.
- [11] A. T. Aho *et al.*, “High-Power 1180-nm GaInNAs DBR Laser Diodes,” pp. 1–4, 2017.
- [12] A. T. Aho, J. Viheriala, M. Koskinen, T. Uusitalo, J. Reuna, and M. Guina, “High-Power 1.5 μm Tapered Distributed Bragg Reflector Laser Diodes for Eye-Safe LIDAR,” *IEEE Photonics Technol. Lett.*, vol. 32, no. 19, pp. 1249–1252, Oct. 2020, doi: 10.1109/LPT.2020.3019845.
- [13] D. C. Law *et al.*, “Future technology pathways of terrestrial III-V multijunction solar cells for concentrator photovoltaic systems,” *Sol. Energy Mater. Sol. Cells*, vol. 94, no. 8, pp. 1314–1318, 2010, doi: 10.1016/j.solmat.2008.07.014.
- [14] R. R. King *et al.*, “40 % efficient metamorphic GaInP/GaInAs/Ge multijunction solar cells,” *Appl. Phys. Lett.*, vol. 90, no. 18, 2007, doi: <http://dx.doi.org/10.1063/1.2734507>.
- [15] J. F. Geisz *et al.*, “Six-junction III–V solar cells with 47.1% conversion efficiency under 143 Suns concentration,” *Nat. Energy*, vol. 5, no. 4, pp. 326–335, Apr. 2020, doi: 10.1038/s41560-020-0598-5.

- [16] A. Aho *et al.*, “Lattice-matched four-junction tandem solar cell including two dilute nitride bottom junctions,” *Prog. Photovoltaics Res. Appl.*, vol. 27, no. 4, pp. 299–305, Dec. 2019, doi: 10.1002/pip.3094.
- [17] M. A. Khan, D. T. Olson, J. M. Van Hove, and J. N. Kuznia, “Vertical-cavity, room-temperature stimulated emission from photopumped GaN films deposited over sapphire substrates using low-pressure metalorganic chemical vapor deposition,” *Appl. Phys. Lett.*, vol. 58, no. 14, pp. 1515–1517, 1991, doi: 10.1063/1.105163.
- [18] J. Nikkinen, A. Härkönen, I. Leino, and M. Guina, “Generation of Sub-100 ps Pulses at 532, 355, and 266 nm Using a SESAM Q-Switched Microchip Laser,” *IEEE Photonics Technol. Lett.*, vol. 29, no. 21, pp. 1816–1819, 2017, doi: 10.1109/LPT.2017.2752421.
- [19] F. Hjort *et al.*, “A 310 nm Optically Pumped AlGaIn Vertical-Cavity Surface-Emitting Laser,” *ACS Photonics*, vol. 8, no. 1, pp. 135–141, 2021, doi: 10.1021/acsp Photonics.0c01382.
- [20] J. Nikkinen, V. M. Korpijärvi, I. Leino, A. Härkönen, and M. Guina, “Microchip laser Q-switched with GaInNAs/GaAs SESAM emitting 204 ps pulses at 1342 nm,” *Electron. Lett.*, vol. 51, no. 11, pp. 850–852, 2015, doi: 10.1049/el.2015.1000.
- [21] S. P. Ojanen *et al.*, “GaSb diode lasers tunable around 2.6 μ m using silicon photonics resonators or external diffractive gratings,” *Appl. Phys. Lett.*, vol. 116, no. 8, 2020, doi: 10.1063/1.5140062.
- [22] D. J. Friedman, “Progress and challenges for next-generation high-efficiency multijunction solar cells,” *Curr. Opin. Solid State Mater. Sci.*, vol. 14, no. 6, pp. 131–138, 2010, doi: <http://dx.doi.org/10.1016/j.cossms.2010.07.001>.
- [23] J. Zhao and M. A. Green, “Optimized antireflection coatings for high efficiency silicon solar cells,” *IEEE Trans. Electron Devices*, vol. 38, no. 8,

- pp. 1925–1934, 1991, doi: 10.1109/16.119035.
- [24] H. Nagel, A. G. Aberle, and R. Hezel, “Optimised antireflection coatings for planar silicon solar cells using remote PECVD silicon nitride and porous silicon dioxide,” *Prog. Photovoltaics Res. Appl.*, vol. 7, no. 4, pp. 245–260, 1999, doi: 10.1002/(SICI)1099-159X(199907/08)7:4<245::AID-PIP255>3.0.CO;2-3.
- [25] C. H. Henry, “Limiting efficiencies of ideal single and multiple energy gap terrestrial solar cells,” *J. Appl. Phys.*, vol. 51, no. 8, pp. 4494–4500, 1980, doi: 10.1063/1.328272.
- [26] E. C. Warmann, M. S. Leite, and H. A. Atwater, “Photovoltaic efficiencies in lattice-matched III-V multijunction solar cells with unconventional lattice parameters,” in *Photovoltaic Specialists Conference (PVSC), 2011 37th IEEE*, 2011, pp. 570–574, doi: 10.1109/PVSC.2011.6186019.
- [27] A. Polman and H. a. Atwater, “Photonic design principles for ultrahigh-efficiency photovoltaics,” *Nat. Mater.*, vol. 11, no. 3, pp. 174–177, 2012, doi: 10.1038/nmat3263.
- [28] “AZUR SPACE Solar Power GmbH.” <http://www.azurspace.com/index.php/en/>.
- [29] “SPECTROLAB, INC.” <https://www.spectrolab.com/index.html>.
- [30] M. Price, C. Kitchen, H. Eaves, R. Crabb, and P. Buia, “Solar cell coverglasses for satellites in the intermediate earth orbit,” *Eur. Sp. Agency, (Special Publ. ESA SP*, no. 416 PART 2, pp. 569–572, 1998, doi: 10.1109/pvsc.1997.654260.
- [31] D. Wilt, N. Snyder, P. Jenkins, and A. Gray, “Novel flexible solar cell coverglass for space photovoltaic devices,” in *2013 IEEE 39th Photovoltaic Specialists Conference (PVSC)*, Jun. 2013, pp. 2835–2839, doi: 10.1109/PVSC.2013.6745062.

- [32] K. K. Chong, S. L. Lau, T. K. Yew, and P. C. L. Tan, "Design and development in optics of concentrator photovoltaic system," *Renew. Sustain. Energy Rev.*, vol. 19, pp. 598–612, 2013, doi: 10.1016/j.rser.2012.11.005.
- [33] D. J. Aiken, "Antireflection coating design for series interconnected multi-junction solar cells," *Prog. Photovoltaics Res. Appl.*, vol. 8, no. 6, pp. 563–570, Nov. 2000, doi: 10.1002/1099-159X(200011/12)8:6<563::AID-PIP327>3.0.CO;2-8.
- [34] R. R. King *et al.*, "High-Voltage , Low-Current GaInP / GaInP / GaAs / GaInNAs / Ge Solar Cells," 2002.
- [35] M. Ochoa *et al.*, "Modelling of lattice matched dilute nitride 4-junction concentrator solar cells on Ge substrates," *AIP Conf. Proc.*, vol. 1766, no. September, 2016, doi: 10.1063/1.4962101.
- [36] R. R. King *et al.*, "40% efficient metamorphic GaInP/GaInAs/Ge multijunction solar cells," *Appl. Phys. Lett.*, vol. 90, no. 18, p. 183516, Apr. 2007, doi: 10.1063/1.2734507.
- [37] N. A. Torkhov, "Formation of a native-oxide structure on the surface of n-GaAs under natural oxidation in air," *Semiconductors*, vol. 37, no. 10, pp. 1177–1184, Oct. 2003, doi: 10.1134/1.1619513.
- [38] R. Toyoshima, S. Murakami, S. Eguchi, K. Amemiya, K. Mase, and H. Kondoh, "Initial oxidation of GaAs(100) under near-realistic environments revealed by in situ AP-XPS," *Chem. Commun.*, vol. 56, no. 94, pp. 14905–14908, 2020, doi: 10.1039/D0CC05279E.
- [39] S. Van Riesen and A. W. Bett, "Degradation study of III-V solar cells for concentrator applications," *Prog. Photovoltaics Res. Appl.*, vol. 13, no. 5, pp. 369–380, 2005, doi: 10.1002/pip.603.
- [40] H. K. Pulker, *Coatings on Glass*, 2nd ed. Elsevier, 1999.

- [41] H. K. Pulker, "Characterization of optical thin films," *Appl. Opt.*, vol. 18, no. 12, p. 1969, Jun. 1979, doi: 10.1364/AO.18.001969.
- [42] O. S. Heavens, "Optical properties of thin films," *Reports Prog. Phys.*, vol. 23, no. 1, p. 1, 1960, [Online]. Available: <http://stacks.iop.org/0034-4885/23/i=1/a=301>.
- [43] A. Macleod, *Optical Thin Films*, Third Edit. Elsevier Inc., 2012.
- [44] M. A. Green *et al.*, "Solar cell efficiency tables (Version 60)," *Prog. Photovoltaics Res. Appl.*, no. May, pp. 687–701, 2022, doi: 10.1002/pip.3595.
- [45] K. Sasaki, T. Agui, K. Nakaido, N. Takahashi, R. Onitsuka, and T. Takamoto, "Development Of InGaP/GaAs/InGaAs inverted triple junction concentrator solar cells," *AIP Conf. Proc.*, vol. 1556, no. September, pp. 22–25, 2013, doi: 10.1063/1.4822190.
- [46] J. F. Geisz *et al.*, "Building a Six-Junction Inverted Metamorphic Concentrator Solar Cell," *IEEE J. Photovoltaics*, vol. 8, no. 2, pp. 626–632, 2018, doi: 10.1109/JPHOTOV.2017.2778567.
- [47] F. Dimroth *et al.*, "Four-Junction Wafer-Bonded Concentrator," vol. 6, no. 1, pp. 343–349, 2016.
- [48] N. Jain *et al.*, "High-efficiency inverted metamorphic 1.7/1.1 eV GaInAsP/GaInAs dual-junction solar cells," *Appl. Phys. Lett.*, vol. 112, no. 5, p. 053905, Jan. 2018, doi: 10.1063/1.5008517.
- [49] S. B. Musalinov, A. P. Anzulevich, I. V. Bychkov, A. S. Gudovskikh, and M. Z. Shvarts, "Influence of double- and triple-layer antireflection coatings on the formation of photocurrents in multijunction III–V solar cells," *Semiconductors*, vol. 51, no. 1, pp. 88–92, Jan. 2017, doi: 10.1134/S1063782617010146.

- [50] W. L. Wang and X. H. Rong, "Antireflection with Multilayer Structure Used on Silicon Solar Cell," *Appl. Mech. Mater.*, vol. 66--68, pp. 1–4, 2011, doi: 10.4313/TEEM.2010.11.1.033.
- [51] S. Saylan, T. Milakovich, S. A. Hadi, A. Nayfeh, E. A. Fitzgerald, and M. S. Dahlem, "Multilayer antireflection coating design for GaAs_{0.69}P_{0.31}/Si dual-junction solar cells," *Sol. Energy*, vol. 122, pp. 76–86, 2015, doi: 10.1016/j.solener.2015.07.049.
- [52] U. Sikder and M. A. Zaman, "Optimization of multilayer antireflection coating for photovoltaic applications," *Opt. Laser Technol.*, vol. 79, pp. 88–94, May 2016, doi: 10.1016/j.optlastec.2015.11.011.
- [53] C.-H. Sun, B. J. Ho, B. Jiang, and P. Jiang, "Biomimetic subwavelength antireflective gratings on GaAs," *Opt. Lett.*, vol. 33, no. 19, p. 2224, 2008, doi: 10.1364/ol.33.002224.
- [54] J. W. Leem, J. Su Yu, D. H. Jun, J. Heo, and W. K. Park, "Efficiency improvement of III-V GaAs solar cells using biomimetic TiO₂ subwavelength structures with wide-angle and broadband antireflection properties," *Sol. Energy Mater. Sol. Cells*, vol. 127, pp. 43–49, 2014, doi: 10.1016/j.solmat.2014.03.041.
- [55] D. Liang, Y. Kang, Y. Huo, Y. Chen, Y. Cui, and J. S. Harris, "High-Efficiency Nanostructured Window GaAs Solar Cells," *Nano Lett.*, vol. 13, no. 10, pp. 4850–4856, Oct. 2013, doi: 10.1021/nl402680g.
- [56] J. Tommila *et al.*, "Moth-eye antireflection coating fabricated by nanoimprint lithography on 1 eV dilute nitride solar cell," *Prog. Photovoltaics Res. Appl.*, vol. 21, no. 5, pp. 1158–1162, Aug. 2013, doi: 10.1002/pip.2191.
- [57] J. Tommila *et al.*, "Nanostructured broadband antireflection coatings on AlInP fabricated by nanoimprint lithography," *Sol. Energy Mater. Sol. Cells*, vol. 94, no. 10, pp. 1845–1848, Oct. 2010, doi:

10.1016/j.solmat.2010.05.053.

- [58] J. Zhu, C. M. Hsu, Z. Yu, S. Fan, and Y. Cui, “Nanodome solar cells with efficient light management and self-cleaning,” *Nano Lett.*, vol. 10, no. 6, pp. 1979–1984, 2010, doi: 10.1021/nl9034237.
- [59] E. E. Perl, C. T. Lin, W. E. McMahon, D. J. Friedman, and J. E. Bowers, “Ultrabroadband and wide-angle hybrid antireflection coatings with nanostructures,” *IEEE J. Photovoltaics*, vol. 4, no. 3, pp. 962–967, 2014, doi: 10.1109/JPHOTOV.2014.2304359.
- [60] W. Zhou, M. Tao, L. Chen, and H. Yang, “Microstructured surface design for omnidirectional antireflection coatings on solar cells,” *J. Appl. Phys.*, vol. 102, no. 10, 2007, doi: 10.1063/1.2817470.
- [61] R. M. France *et al.*, “Triple-junction solar cells with 39.5% terrestrial and 34.2% space efficiency enabled by thick quantum well superlattices,” *Joule*, vol. 6, no. 5, pp. 1121–1135, May 2022, doi: 10.1016/j.joule.2022.04.024.
- [62] H. A. Macleod, *Thin-Film Optical Filters*, 4th ed. CRC Press, 2010.
- [63] P. Baumeister, “Starting designs for the computer optimization of optical coatings,” *Appl. Opt.*, vol. 34, no. 22, pp. 4835–43, 1995, doi: 10.1364/AO.34.004835.
- [64] Z. Knittl, *Optics of Thin Films*, 1st ed. John Wiley & Sons, Ltd., 1976.
- [65] S. Martin, J. Rivory, and M. Schoenauer, “Synthesis of optical multilayer systems using genetic algorithms,” *Appl. Opt.*, vol. 34, no. 13, pp. 2247–2254, 1995.
- [66] R. R. Willey, *Practical Design and Production of Optical Thin Films*, 2nd ed. CRC Press, 2002.

- [67] X. Li, J. Gao, L. Xue, and Y. Han, “Porous polymer films with gradient-refractive-index structure for broadband and omnidirectional antireflection coatings,” *Adv. Funct. Mater.*, vol. 20, no. 2, pp. 259–265, 2010, doi: 10.1002/adfm.200901052.
- [68] G. Tan *et al.*, “Broadband antireflection film with moth-eye-like structure for flexible display applications,” *Optica*, vol. 4, no. 7, p. 678, 2017, doi: 10.1364/OPTICA.4.000678.
- [69] M. Keshavarz Hedayati and M. Elbahri, “Antireflective Coatings: Conventional Stacking Layers and Ultrathin Plasmonic Metasurfaces, A Mini-Review,” *Materials (Basel)*, vol. 9, no. 6, p. 497, Jun. 2016, doi: 10.3390/ma9060497.
- [70] J. A. Dobrowolski, D. Poitras, P. Ma, H. Vakil, and M. Acree, “Toward perfect antireflection coatings: numerical investigation,” *Appl. Opt.*, vol. 41, no. 16, pp. 3075–3083, 2002, doi: 10.1364/AO.41.003075.
- [71] T. Amotchkina, A. Tikhonravov, and M. Trubetskov, “Estimation for the number of layers of broad band anti-reflection coatings,” Sep. 2008, p. 710104, doi: 10.1117/12.796590.
- [72] P. P. Altermatt, “Silicon Solar Cells,” in *Optoelectronic Devices*, no. 3, New York: Springer-Verlag, 2005, pp. 313–341.
- [73] S. J. Eisele, T. C. Röder, J. R. Köhler, and J. H. Werner, “18.9% efficient full area laser doped silicon solar cell,” *Appl. Phys. Lett.*, vol. 95, no. 13, p. 133501, Sep. 2009, doi: 10.1063/1.3232208.
- [74] A. El amrani, I. Menous, L. Mahiou, R. Tadjine, A. Touati, and A. Lefgoum, “Silicon nitride film for solar cells,” *Renew. Energy*, vol. 33, no. 10, pp. 2289–2293, Oct. 2008, doi: 10.1016/j.renene.2007.12.015.
- [75] M. Beye, M. E. Faye, A. Ndiaye, F. Ndiaye, and A. S. Maiga, “Optimization of SiN_x Single and Double Layer ARC for Silicon Thin

- Film Solar Cells on Glass,” *Res. J. Appl. Sci. Eng. Technol.*, vol. 6, no. 3, pp. 412–416, Jun. 2013, doi: 10.19026/rjaset.6.4094.
- [76] F. Fertig *et al.*, “Economic feasibility of bifacial silicon solar cells,” *Prog. Photovoltaics Res. Appl.*, vol. 24, no. 6, pp. 800–817, Jun. 2016, doi: 10.1002/pip.2730.
- [77] A. Aho, J. Tommila, A. Tukiainen, V. Polojärvi, T. Niemi, and M. Guina, “Moth eye antireflection coated GaInP/GaAs/GaInNAs solar cell,” *AIP Conf. Proc.*, vol. 33, no. May, pp. 33–36, 2014, doi: 10.1063/1.4897022.
- [78] A. Aho *et al.*, “High efficiency lattice-matched 4j space solar cells on gaas,” in *2019 European Space Power Conference, ESPC 2019*, 2019, doi: 10.1109/ESPC.2019.8932092.
- [79] A. Aho, A. Tukiainen, V. Polojarvi, and M. Guina, “Performance assessment of multijunction solar cells incorporating GaInNAsSb,” *Nanoscale Res. Lett.*, vol. 9, pp. 1–7, 2014, doi: 10.1186/1556-276X-9-61.
- [80] H. Demiryont, J. R. Sites, and K. Geib, “Effects of oxygen content on the optical properties of tantalum oxide films deposited by ion-beam sputtering,” *Appl. Opt.*, vol. 24, no. 4, p. 490, Feb. 1985, doi: 10.1364/AO.24.000490.
- [81] T. Amotchkina, M. K. Trubetskov, A. V Tikhonravov, I. B. Angelov, and V. Pervak, “Reliable optical characterization of e-beam evaporated TiO₂ films deposited at different substrate temperatures,” in *Optical Interference Coatings*, Feb. 2014, vol. 53, no. 4, p. FA.6, doi: 10.1364/AO.53.0000A8.
- [82] W. WEINSTEIN, “The Reflectivity and Transmissivity of Multiple Thin Coatings,” *J. Opt. Soc. Am.*, vol. 37, no. 7, p. 576, Jul. 1947, doi: 10.1364/JOSA.37.000576.
- [83] F. Abelès, “Recherches sur la propagation des ondes électromagnétiques sinusoïdales dans les milieux stratifiés,” *Ann. Phys. (Paris)*, vol. 12, no. 5,

pp. 596–640, Apr. 1950, doi: 10.1051/anphys/195012050596.

- [84] A. Herpin, “Calcul du pouvoir réflecteur d’un système stratifié quelconque,” *Comptes Rendus*, no. 225, pp. 182–183, 1947.
- [85] A. Macleod, “The Essential Macleod,” *software by Thin Film Center Inc.* Thin Film Center Inc, Tucson, AZ, USA, 1997, [Online]. Available: <https://www.thinfilmcenter.com/essential.php>.
- [86] FTG Software Associates, “FilmStar.” Princeton, NJ, USA, [Online]. Available: <http://www.ftgsoftware.com/design.htm>.
- [87] M. K. Tikhonravov, A. V. and Trubetskov, “OptiLayer thin film software.” [Online]. Available: <http://www.optilayer.com>.
- [88] S. J. Byrnes, “Multilayer optical calculations,” pp. 1–20, 2016, [Online]. Available: <http://arxiv.org/abs/1603.02720>.
- [89] A. Luce, A. Mahdavi, F. Marquardt, and H. Wankerl, “TMM-Fast, a transfer matrix computation package for multilayer thin-film optimization: tutorial,” *J. Opt. Soc. Am. A*, vol. 39, no. 6, p. 1007, 2022, doi: 10.1364/josaa.450928.
- [90] S. Larouche and L. Martinu, “OpenFilters: open-source software for the design, optimization, and synthesis of optical filters,” *Appl. Opt.*, vol. 47, no. 13, p. C219, May 2008, doi: 10.1364/AO.47.00C219.
- [91] “ASTM G173-03 Reference Spectra.” <http://rredc.nrel.gov/solar/spectra/am1.5/astmg173/astmg173.html>.
- [92] C. Kauppinen, K. Isakov, and M. Söponen, “Grass-like Alumina with Low Refractive Index for Scalable, Broadband, Omnidirectional Antireflection Coatings on Glass Using Atomic Layer Deposition,” *ACS Appl. Mater. Interfaces*, vol. 9, no. 17, pp. 15038–15043, May 2017, doi:

10.1021/acsami.7b01733.

- [93] V. Dokmai, R. Methaapanon, and V. Pavarajarn, "Corrosion of amorphous alumina in deionized water under mild condition," *Appl. Surf. Sci.*, vol. 499, no. September 2019, p. 143906, Jan. 2020, doi: 10.1016/j.apsusc.2019.143906.
- [94] C. Yin *et al.*, "Al₂O₃ anti-reflection coatings with graded-refractive index profile for laser applications," *Opt. Mater. Express*, vol. 11, no. 3, p. 875, Mar. 2021, doi: 10.1364/OME.418174.
- [95] K. Isakov, C. Kauppinen, S. Franssila, and H. Lipsanen, "Superhydrophobic Antireflection Coating on Glass Using Grass-like Alumina and Fluoropolymer," *ACS Appl. Mater. Interfaces*, vol. 12, no. 44, pp. 49957–49962, Nov. 2020, doi: 10.1021/acsami.0c12465.
- [96] J. Tommila, *Nanoscale Architecture for Site-controlled Epitaxy and Antireflective Coatings*, vol. 1159, no. 2013. 2013.
- [97] C.-H. Sun, P. Jiang, and B. Jiang, "Broadband moth-eye antireflection coatings on silicon," *Appl. Phys. Lett.*, vol. 92, no. 6, p. 061112, Feb. 2008, doi: 10.1063/1.2870080.
- [98] Q. Chen *et al.*, "Broadband moth-eye antireflection coatings fabricated by low-cost nanoimprinting," *Appl. Phys. Lett.*, vol. 94, no. 26, p. 263118, Jun. 2009, doi: 10.1063/1.3171930.
- [99] S. Rasappa *et al.*, "High molecular weight block copolymer lithography for nanofabrication of hard mask and photonic nanostructures," *J. Colloid Interface Sci.*, vol. 534, pp. 420–429, 2019, doi: 10.1016/j.jcis.2018.09.040.
- [100] P. Repo, *Reducing surface recombination in black silicon photovoltaic devices using atomic layer deposition*. 2016.

- [101] E. W. Thornton and P. G. Harrison, "Tin oxide surfaces. Part 1.—Surface hydroxyl groups and the chemisorption of carbon dioxide and carbon monoxide on tin(IV) oxide," *J. Chem. Soc. Faraday Trans. 1 Phys. Chem. Condens. Phases*, vol. 71, p. 461, 1975, doi: 10.1039/f19757100461.
- [102] S. Ogura, N. Sugawara, and R. Hiraga, "Refractive index and packing density for MgF₂ films: Correlation of temperature dependence with water sorption," *Thin Solid Films*, vol. 30, no. 1, pp. 3–10, Nov. 1975, doi: 10.1016/0040-6090(75)90298-9.
- [103] V. A. Markel, "Introduction to the Maxwell Garnett approximation: tutorial," *J. Opt. Soc. Am. A*, vol. 33, no. 7, p. 1244, Jul. 2016, doi: 10.1364/JOSAA.33.001244.
- [104] O. S. Heavens and S. D. Smith, "Dielectric Thin Films*," *J. Opt. Soc. Am.*, vol. 47, no. 6, p. 469, Jun. 1957, doi: 10.1364/JOSA.47.000469.
- [105] L. Gallais *et al.*, "An exhaustive study of laser damage in ion beam sputtered pure and mixture oxide thin films at 1030 nm with 500 fs pulse durations," vol. 8530, no. 0, pp. 85300K-85300K–8, 2012, doi: 10.1117/12.977553.
- [106] M. Cevro and G. Carter, "Ion beam sputtering and dual ion beam sputtering of titanium oxide films," *J. Phys. D. Appl. Phys.*, vol. 28, no. 9, pp. 1962–1976, Sep. 1995, doi: 10.1088/0022-3727/28/9/026.
- [107] M. F. Lambrinos, R. Valizadeh, and J. S. Colligon, "Effects of bombardment on optical properties during the deposition of silicon nitride by reactive ion-beam sputtering," *Appl. Opt.*, vol. 35, no. 19, p. 3620, Jul. 1996, doi: 10.1364/AO.35.003620.
- [108] H. Y. Chen, S. Han, and H. C. Shih, "The characterization of aluminum nitride thin films prepared by dual ion beam sputtering," *Surf. Coatings Technol.*, vol. 200, no. 10 SPEC. ISS., pp. 3326–3329, 2006, doi: 10.1016/j.surfcoat.2005.07.046.

- [109] T. W. Jolly and R. Lalezari, “Ion-beam sputter deposition techniques for the production of optical coatings of the highest quality,” in *SPIE Thin Films for Optical Systems*, Mar. 1993, vol. 1782, p. 250, doi: 10.1117/12.141036.
- [110] P. Sigmund, “Theory of Sputtering. I. Sputtering Yield of Amorphous and Polycrystalline Targets,” *Phys. Rev.*, vol. 184, no. 2, pp. 383–416, Aug. 1969, doi: 10.1103/PhysRev.184.383.
- [111] M. P. Seah, C. A. Clifford, F. M. Green, and I. S. Gilmore, “An accurate semi-empirical equation for sputtering yields I: for argon ions,” *Surf. Interface Anal.*, vol. 37, no. 5, pp. 444–458, May 2005, doi: 10.1002/sia.2032.
- [112] N. Matsunami *et al.*, “Energy dependence of the ion-induced sputtering yields of monatomic solids,” *At. Data Nucl. Data Tables*, vol. 31, no. 1, pp. 1–80, 1984, doi: 10.1016/0092-640X(84)90016-0.
- [113] M. P. Seah and T. S. Nunney, “Sputtering yields of compounds using argon ions,” *J. Phys. D. Appl. Phys.*, vol. 43, no. 25, p. 253001, Jun. 2010, doi: 10.1088/0022-3727/43/25/253001.
- [114] Y. Yamamura, Y. Itikawa, and N. Itoh, *Angular dependence of sputtering yields of monatomic solids*. Nagoya, Japan: Institute of Plasma Physics, Nagoya University, 1983.
- [115] T. Ohno and S. Samukawa, “Resistive switching in a few nanometers thick tantalum oxide film formed by a metal oxidation,” *Appl. Phys. Lett.*, vol. 106, no. 17, p. 173110, Apr. 2015, doi: 10.1063/1.4919724.
- [116] C. Bundesmann and H. Neumann, “Tutorial: The systematics of ion beam sputtering for deposition of thin films with tailored properties,” *J. Appl. Phys.*, vol. 124, no. 23, p. 231102, Dec. 2018, doi: 10.1063/1.5054046.
- [117] R. Feder, F. Frost, H. Neumann, C. Bundesmann, and B. Rauschenbach,

- “Systematic investigations of low energy Ar ion beam sputtering of Si and Ag,” *Nucl. Instruments Methods Phys. Res. Sect. B Beam Interact. with Mater. Atoms*, vol. 317, no. PART A, pp. 137–142, 2013, doi: 10.1016/j.nimb.2013.01.056.
- [118] T. Lautenschlager, “Systematic investigation of the ion beam sputter deposition of TiO₂, Ph.D. Thesis,” University of Leipzig, 2018.
- [119] J. B. Malherbe, “Sputtering of Compound Semiconductor Surfaces. I. Ion-Solid Interactions and Sputtering Yields,” *Crit. Rev. Solid State Mater. Sci.*, vol. 19, no. 2, pp. 55–127, 1994, doi: 10.1080/10408439408244588.
- [120] M. W. Thompson, “II. The energy spectrum of ejected atoms during the high energy sputtering of gold,” *Philos. Mag.*, vol. 18, no. 152, pp. 377–414, Aug. 1968, doi: 10.1080/14786436808227358.
- [121] W.-L. Min, A. P. Betancourt, P. Jiang, and B. Jiang, “Bioinspired broadband antireflection coatings on GaSb,” *Appl. Phys. Lett.*, vol. 92, no. 14, p. 141109, Apr. 2008, doi: 10.1063/1.2908221.
- [122] K.-S. Han, J.-H. Shin, W.-Y. Yoon, and H. Lee, “Enhanced performance of solar cells with anti-reflection layer fabricated by nano-imprint lithography,” *Sol. Energy Mater. Sol. Cells*, vol. 95, no. 1, pp. 288–291, 2011, doi: <http://dx.doi.org/10.1016/j.solmat.2010.04.064>.
- [123] H.-L. Chen *et al.*, “A 19.9%-efficient ultrathin solar cell based on a 205-nm-thick GaAs absorber and a silver nanostructured back mirror,” *Nat. Energy*, vol. 4, no. 9, pp. 761–767, Sep. 2019, doi: 10.1038/s41560-019-0434-y.
- [124] S. Schaefer and R. Lüdemann, “Low damage reactive ion etching for photovoltaic applications,” *J. Vac. Sci. Technol. A Vacuum, Surfaces, Film.*, vol. 17, no. 3, pp. 749–754, May 1999, doi: 10.1116/1.581644.
- [125] C. Gatzert, A. W. Blakers, P. N. K. Deenapanray, D. Macdonald, and F.

- D. Auret, “Investigation of reactive ion etching of dielectrics and Si in CHF₃/O₂ or CHF₃/Ar for photovoltaic applications,” *J. Vac. Sci. Technol. A Vacuum, Surfaces, Film.*, vol. 24, no. 5, pp. 1857–1865, 2006, doi: 10.1116/1.2333571.
- [126] M. de Lafontaine *et al.*, “Influence of plasma process on III-V/Ge multijunction solar cell via etching,” *Sol. Energy Mater. Sol. Cells*, vol. 195, no. January, pp. 49–54, Jun. 2019, doi: 10.1016/j.solmat.2019.01.048.
- [127] M. de Lafontaine *et al.*, “Anisotropic and low damage III-V/Ge heterostructure etching for multijunction solar cell fabrication with passivated sidewalls,” *Micro Nano Eng.*, vol. 11, no. February, p. 100083, 2021, doi: 10.1016/j.mne.2021.100083.
- [128] D. Kang *et al.*, “Damage and residual layer analysis of reactive ion etching textured multi-crystalline silicon wafer for application to solar cells,” *Sol. Energy*, vol. 233, no. January, pp. 111–117, 2022, doi: 10.1016/j.solener.2022.01.003.
- [129] S. Farhadi, M. Farzaneh, and S. A. Kulinich, “Anti-icing performance of superhydrophobic surfaces,” *Appl. Surf. Sci.*, vol. 257, no. 14, pp. 6264–6269, 2011, doi: 10.1016/j.apsusc.2011.02.057.
- [130] T. Zhu *et al.*, “A transparent superhydrophobic coating with mechanochemical robustness for anti-icing, photocatalysis and self-cleaning,” *Chem. Eng. J.*, vol. 399, no. March, p. 125746, 2020, doi: 10.1016/j.cej.2020.125746.
- [131] A. Allahdini, R. Jafari, and G. Momen, “Transparent non-fluorinated superhydrophobic coating with enhanced anti-icing performance,” *Prog. Org. Coatings*, vol. 165, no. October 2021, p. 106758, 2022, doi: 10.1016/j.porgcoat.2022.106758.
- [132] S. A. Kulinich and M. Farzaneh, “On ice-releasing properties of rough hydrophobic coatings,” *Cold Reg. Sci. Technol.*, vol. 65, no. 1, pp. 60–64,

2011, doi: 10.1016/j.coldregions.2010.01.001.

- [133] S. Yang, Q. Xia, L. Zhu, J. Xue, Q. Wang, and Q. M. Chen, “Research on the icephobic properties of fluoropolymer-based materials,” *Appl. Surf. Sci.*, vol. 257, no. 11, pp. 4956–4962, 2011, doi: 10.1016/j.apsusc.2011.01.003.
- [134] G. Momen, R. Jafari, and M. Farzaneh, “Ice repellency behaviour of superhydrophobic surfaces: Effects of atmospheric icing conditions and surface roughness,” *Appl. Surf. Sci.*, vol. 349, pp. 211–218, 2015, doi: 10.1016/j.apsusc.2015.04.180.
- [135] N. T. Binh, V. T. H. Hanh, N. T. Ngoc, and N. B. Duc, “Anti-icing efficiency on bio-inspired slippery elastomer surface,” *Mater. Chem. Phys.*, vol. 265, no. March, p. 124502, 2021, doi: 10.1016/j.matchemphys.2021.124502.
- [136] M. Drábik *et al.*, “Super-hydrophobic coatings prepared by RF magnetron sputtering of PTFE,” *Plasma Process. Polym.*, vol. 7, no. 7, pp. 544–551, 2010, doi: 10.1002/ppap.200900164.
- [137] X. Yan *et al.*, “Enhanced omnidirectional photovoltaic performance of solar cells using multiple-discrete-layer tailored- and low-refractive index anti-reflection coatings,” *Adv. Funct. Mater.*, vol. 23, no. 5, pp. 583–590, 2013, doi: 10.1002/adfm.201201032.
- [138] D. Cardwell and N. Pan, “Triple junction GaAs high efficiency epitaxial lift-off solar cells,” *Opt. InfoBase Conf. Pap.*, vol. Part F116-, pp. 5–6, 2018, doi: 10.1364/OSE.2018.OW5C.6.
- [139] M. Steiner, G. Siefer, T. Schmidt, M. Wiesenfarth, F. Dimroth, and A. W. Bett, “43% Sunlight to Electricity Conversion Efficiency Using CPV,” *IEEE J. Photovoltaics*, vol. 6, no. 4, pp. 1020–1024, 2016, doi: 10.1109/JPHOTOV.2016.2551460.

- [140] M. Wiemer, V. Sabnis, and H. Yuen, “43.5% efficient lattice matched solar cells,” in *High and Low Concentrator Systems for Solar Electric Applications VI*, Sep. 2011, vol. 8108, p. 810804, doi: 10.1117/12.897769.
- [141] S. J. Fonash, *Solar Cell Device Physics*, 2nd ed. Academic Press, 2010.
- [142] M. Hermle, G. Létay, S. P. Philipps, and A. W. Bett, “Numerical simulation of tunnel diodes for multi-junction solar cells,” *Prog. Photovoltaics Res. Appl.*, vol. 16, no. 5, pp. 409–418, Aug. 2008, doi: 10.1002/pip.824.
- [143] W. Guter *et al.*, “Current-matched triple-junction solar cell reaching 41.1% conversion efficiency under concentrated sunlight,” *Appl. Phys. Lett.*, vol. 94, no. 22, pp. 8–11, Jun. 2009, doi: 10.1063/1.3148341.
- [144] I. Horcas, R. Fernández, J. M. Gómez-Rodríguez, J. Colchero, J. Gómez-Herrero, and A. M. Baro, “WSXM: A software for scanning probe microscopy and a tool for nanotechnology,” *Rev. Sci. Instrum.*, vol. 78, no. 013705, pp. 1–8, 2007, doi: 10.1063/1.2432410.
- [145] X. Zhang and Z. Liu, “Superlenses to overcome the diffraction limit,” *Nat. Mater.*, vol. 7, no. 6, pp. 435–441, 2008, doi: 10.1038/nmat2141.
- [146] N. I. Zheludev, “What diffraction limit?,” *Nat. Mater.*, vol. 7, no. 6, pp. 420–422, 2008, doi: 10.1038/nmat2163.
- [147] G. Chen, Z. Q. Wen, and C. W. Qiu, “Superoscillation: from physics to optical applications,” *Light Sci. Appl.*, vol. 8, no. 1, 2019, doi: 10.1038/s41377-019-0163-9.
- [148] T. Lepistö, *Pyyhkäisyelektronimikroskopia ja Mikroanalysointi*, 1st ed. Juvenes Print, 2016.
- [149] H. G. Tompkins and E. A. Irene, *Handbook of Ellipsometry*, 1st ed. William

Andrew, Inc., 2005.

- [150] B. Tatian, “Fitting refractive-index data with the Sellmeier dispersion formula,” *Appl. Opt.*, vol. 23, no. 24, p. 4477, 1984, doi: 10.1364/AO.23.004477.
- [151] B. von Blanckenhagen, D. Tonova, and J. Ullmann, “Application of the Tauc-Lorentz formulation to the interband absorption of optical coating materials,” *Appl. Opt.*, vol. 41, no. 16, p. 3137, Jun. 2002, doi: 10.1364/AO.41.003137.
- [152] H. Nesswetter, P. Lugli, A. W. Bett, and C. G. Zimmermann, “Electroluminescence and photoluminescence characterization of multijunction solar cells,” *Conf. Rec. IEEE Photovolt. Spec. Conf.*, vol. 3, no. PART 2, pp. 353–358, 2012, doi: 10.1109/pvsc-vol2.2012.6656769.
- [153] D. Lan, J. F. Geisz, M. A. Steiner, I. Garcia, D. J. Friedman, and M. A. Green, “Improved modeling of photoluminescent and electroluminescent coupling in multijunction solar cells,” *Sol. Energy Mater. Sol. Cells*, vol. 143, pp. 48–51, 2015, doi: 10.1016/j.solmat.2015.06.036.
- [154] F. Trespidi, A. Malchiodi, and F. Farina, “Note: Photoluminescence measurement system for multi-junction solar cells,” *Rev. Sci. Instrum.*, vol. 88, no. 5, 2017, doi: 10.1063/1.4982586.
- [155] J. García-García, J. González-Hernández, J. G. Mendoza-Alvarez, E. L. Cruz, and G. Contreras-Puente, “Photoluminescence characterization of the surface layer of chemically etched CdTe,” *J. Appl. Phys.*, vol. 67, no. 8, pp. 3810–3814, 1990, doi: 10.1063/1.346055.
- [156] M. M. May *et al.*, “On the benchmarking of multi-junction photoelectrochemical fuel generating devices,” *Sustain. Energy Fuels*, vol. 1, no. 3, pp. 492–503, 2017, doi: 10.1039/C6SE00083E.
- [157] H. Koivuluoto, C. Stenroos, R. Ruohomaa, G. Bolelli, L. Lusvarghi, and

- P. Vuoristo, “Research on icing behavior and ice adhesion testing of icephobic surfaces,” *Proc. 16th Int. Work. Atmos. Icing Struct. IW AIS XVI*, Jun 28–Jul 3, pp. 1–14, 2015, [Online]. Available: http://windren.se/IWAIS_p/IWAIS2015/IWAIS2015_pa/49_05_04_Paper_Koivuluoto_et_al_Research_on_icing_behavior_and_ice_adhesion_testing_of_icephobic_surfaces_49_WAIS_2015.pdf.
- [158] H. Koivuluoto, E. Hartikainen, and H. Niemelä-Anttonen, “Thermally Sprayed Coatings: Novel Surface Engineering Strategy Towards Icephobic Solutions,” *Materials (Basel)*, vol. 13, no. 6, p. 1434, Mar. 2020, doi: 10.3390/ma13061434.
- [159] H. Niemelä-Anttonen *et al.*, “Icephobicity of Slippery Liquid Infused Porous Surfaces under Multiple Freeze–Thaw and Ice Accretion–Detachment Cycles,” *Adv. Mater. Interfaces*, vol. 5, no. 20, pp. 1–8, 2018, doi: 10.1002/admi.201800828.
- [160] V. Donadei, H. Koivuluoto, E. Sarlin, H. Niemelä-Anttonen, T. Varis, and P. Vuoristo, “The effect of mechanical and thermal stresses on the performance of lubricated icephobic coatings during cyclic icing/deicing tests,” *Prog. Org. Coatings*, vol. 163, no. November 2021, 2022, doi: 10.1016/j.porgcoat.2021.106614.
- [161] S. Jung, M. Dorrestijn, D. Raps, A. Das, C. M. Megaridis, and D. Poulidakos, “Are superhydrophobic surfaces best for icephobicity?,” *Langmuir*, vol. 27, no. 6, pp. 3059–3066, 2011, doi: 10.1021/la104762g.
- [162] J. Chen *et al.*, “Superhydrophobic surfaces cannot reduce ice adhesion,” *Appl. Phys. Lett.*, vol. 101, no. 11, pp. 18–21, 2012, doi: 10.1063/1.4752436.
- [163] M. Nosonovsky and V. Hejazi, “Why superhydrophobic surfaces are not always icephobic,” *ACS Nano*, vol. 6, no. 10, pp. 8488–8491, 2012, doi: 10.1021/nn302138r.

- [164] K. K. Varanasi, T. Deng, J. D. Smith, M. Hsu, and N. Bhate, “Frost formation and ice adhesion on superhydrophobic surfaces,” *Appl. Phys. Lett.*, vol. 97, no. 23, pp. 95–98, 2010, doi: 10.1063/1.3524513.
- [165] L. Oberli, D. Caruso, C. Hall, M. Fabretto, P. J. Murphy, and D. Evans, “Condensation and freezing of droplets on superhydrophobic surfaces,” *Adv. Colloid Interface Sci.*, vol. 210, pp. 47–57, 2014, doi: 10.1016/j.cis.2013.10.018.
- [166] S. A. Kulinich, S. Farhadi, K. Nose, and X. W. Du, “Superhydrophobic surfaces: Are they really ice-repellent?,” *Langmuir*, vol. 27, no. 1, pp. 25–29, 2011, doi: 10.1021/la104277q.
- [167] K.-Y. Law, “Definitions for Hydrophilicity, Hydrophobicity, and Superhydrophobicity: Getting the Basics Right,” *J. Phys. Chem. Lett.*, vol. 5, no. 4, pp. 686–688, Feb. 2014, doi: 10.1021/jz402762h.
- [168] J. Drelich and E. Chibowski, “Superhydrophilic and superwetting surfaces: Definition and mechanisms of control,” *Langmuir*, vol. 26, no. 24, pp. 18621–18623, 2010, doi: 10.1021/la1039893.
- [169] B. Samuel, H. Zhao, and K. Y. Law, “Study of wetting and adhesion interactions between water and various polymer and superhydrophobic surfaces,” *J. Phys. Chem. C*, vol. 115, no. 30, pp. 14852–14861, 2011, doi: 10.1021/jp2032466.
- [170] A. Marmur, “Thermodynamic aspects of contact angle hysteresis,” *Adv. Colloid Interface Sci.*, vol. 50, pp. 121–141, May 1994, doi: 10.1016/0001-8686(94)80028-6.
- [171] L. Gao and T. J. McCarthy, “Contact Angle Hysteresis Explained,” *Langmuir*, vol. 22, no. 14, pp. 6234–6237, Jul. 2006, doi: 10.1021/la060254j.
- [172] F. Dimroth *et al.*, “Four-Junction Wafer-Bonded Concentrator Solar

- Cells,” *Ieee J. Photovoltaics*, vol. 6, no. 1, pp. 343–349, 2016, doi: 10.1109/JPHOTOV.2015.2501729.
- [173] H. K. Pulker and C. Zaminer, “Composition and structure of vapour-deposited cryolite films,” *Thin Solid Films*, vol. 5, no. 5–6, pp. 421–428, May 1970, doi: 10.1016/0040-6090(70)90113-6.
- [174] H. K. Pulker and E. Jung, “Correlation between film structure and sorption behaviour of vapour deposited ZnS, cryolite and MgF₂ films,” *Thin Solid Films*, vol. 9, no. 1, pp. 57–66, 1972, doi: 10.1016/0040-6090(72)90330-6.
- [175] R. P. Netterfield, “Refractive indices of zinc sulfide and cryolite in multilayer stacks,” *Appl. Opt.*, vol. 15, no. 8, p. 1969, 1976, doi: 10.1364/ao.15.001969.
- [176] L. Dumas, E. Quesnel, J.-Y. Robic, and Y. Pauleau, “Characterization of magnesium fluoride thin films deposited by direct electron beam evaporation,” *J. Vac. Sci. Technol. A Vacuum, Surfaces, Film.*, vol. 18, no. 2, p. 465, 2000, doi: 10.1116/1.582210.
- [177] G. Atanassov, J. Turlo, J. K. Fu, and Y. S. Dai, “Mechanical, optical and structural properties of TiO₂ and MgF₂ thin films deposited by plasma ion assisted deposition,” *Thin Solid Films*, vol. 342, no. 1–2, pp. 83–92, 1999, doi: [http://dx.doi.org/10.1016/S0040-6090\(98\)01407-2](http://dx.doi.org/10.1016/S0040-6090(98)01407-2).
- [178] H. Yu, H. Qi, Y. Cui, Y. Shen, J. Shao, and Z. Fan, “Influence of substrate temperature on properties of MgF₂ coatings,” *Appl. Surf. Sci.*, vol. 253, no. 14, pp. 6113–6117, May 2007, doi: 10.1016/j.apsusc.2007.01.037.
- [179] A. Çolak, H. Wormeester, H. J. W. Zandvliet, and B. Poelsema, “Surface adhesion and its dependence on surface roughness and humidity measured with a flat tip,” *Appl. Surf. Sci.*, vol. 258, no. 18, pp. 6938–6942, Jul. 2012, doi: 10.1016/j.apsusc.2012.03.138.

- [180] H. E. Bennett and J. O. Porteus, "Relation Between Surface Roughness and Specular Reflectance at Normal Incidence," *J. Opt. Soc. Am.*, vol. 51, no. 2, p. 123, Feb. 1961, doi: 10.1364/JOSA.51.000123.
- [181] D. L. Deadmore, J. S. Machin, and A. W. Allen, "Stability of Inorganic Fluorine-Bearing Compounds: I, Binary Metallic Fluorides," *J. Am. Ceram. Soc.*, vol. 44, no. 3, pp. 105–109, Mar. 1961, doi: 10.1111/j.1151-2916.1961.tb13722.x.
- [182] A. Aho, "Dilute Nitride Multijunction Solar Cells Grown by Molecular Beam Epitaxy," Tampere University of Technology, 2015.
- [183] A. Aho *et al.*, "Composition dependent growth dynamics in molecular beam epitaxy of GaInNAs solar cells," *Sol. Energy Mater. Sol. Cells*, vol. 124, pp. 150–158, 2014, doi: <http://dx.doi.org/10.1016/j.solmat.2014.01.044>.
- [184] S. Kurtz, J. F. Geisz, D. J. Friedman, W. K. Metzger, R. R. King, and N. H. Karam, "Annealing-induced-type conversion of GaInNAs," *J. Appl. Phys.*, vol. 95, no. 5, pp. 2505–2508, Mar. 2004, doi: 10.1063/1.1643775.
- [185] V. M. Korpijärvi *et al.*, "Study of nitrogen incorporation into GaInNAs: The role of growth temperature in molecular beam epitaxy," *J. Appl. Phys.*, vol. 112, no. 2, 2012, doi: 10.1063/1.4737127.
- [186] M. Hugues, B. Damilano, J. M. Chauveau, J. Y. Duboz, and J. Massies, "Blue-shift mechanisms in annealed (Ga,In) (N,As) GaAs quantum wells," *Phys. Rev. B - Condens. Matter Mater. Phys.*, vol. 75, no. 4, p. 045313, Jan. 2007, doi: 10.1103/PhysRevB.75.045313.
- [187] D. Bisping, D. Pucicki, M. Fischer, S. Höfling, and A. Forchel, "Influence of arsenic flux on the annealing properties of GaInNAs quantum wells for long wavelength laser applications around 1.6 μm ," *J. Cryst. Growth*, vol. 311, no. 7, pp. 1715–1718, 2009, doi: 10.1016/j.jcrysgro.2008.09.206.
- [188] E. M. Pavelescu *et al.*, "Growth-temperature-dependent (self-)annealing-

- induced blueshift of photoluminescence from 1.3 μm GaInNAs/GaAs quantum wells,” *Appl. Phys. Lett.*, vol. 83, no. 8, pp. 1497–1499, 2003, doi: 10.1063/1.1601309.
- [189] A. Gubanov, V. Polojärvi, A. Aho, A. Tukiainen, N. V. Tkachenko, and M. Guina, “Dynamics of time-resolved photoluminescence in GaInNAs and GaNAsSb solar cells,” *Nanoscale Res. Lett.*, vol. 9, no. 1, p. 80, Dec. 2014, doi: 10.1186/1556-276X-9-80.
- [190] K. Meyer, I. K. Schuller, and C. M. Falco, “Thermalization of sputtered atoms,” *J. Appl. Phys.*, vol. 52, no. 9, pp. 5803–5805, 1981, doi: 10.1063/1.329473.
- [191] R. Feder, C. Bundesmann, H. Neumann, and B. Rauschenbach, “Ion beam sputtering of Ag - Angular and energetic distributions of sputtered and scattered particles,” *Nucl. Instruments Methods Phys. Res. Sect. B Beam Interact. with Mater. Atoms*, vol. 316, pp. 198–204, 2013, doi: 10.1016/j.nimb.2013.09.007.
- [192] D. Kalanov, A. Anders, and C. Bundesmann, “Ion beam sputtering of silicon: Energy distributions of sputtered and scattered ions,” *J. Vac. Sci. Technol. A*, vol. 37, no. 5, p. 051507, 2019, doi: 10.1116/1.5114973.
- [193] G. C. Correa, B. Bao, and N. C. Strandwitz, “Chemical stability of titania and alumina thin films formed by atomic layer deposition,” *ACS Appl. Mater. Interfaces*, vol. 7, no. 27, pp. 14816–14821, 2015, doi: 10.1021/acsami.5b03278.
- [194] N. Yamaguchi, K. Tadanaga, A. Matsuda, T. Minami, and M. Tatsumisago, “Anti-Reflective Coatings of Flowerlike Alumina on Various Glass Substrates by the Sol-Gel Process with the Hot Water Treatment,” *J. Sol-Gel Sci. Technol.*, vol. 33, no. 1, pp. 117–120, Jan. 2005, doi: 10.1007/s10971-005-6711-1.
- [195] D. E. Aspnes, “Optical properties of thin films,” *Thin Solid Films*, vol. 89,

no. 3, pp. 249–262, Mar. 1982, doi: 10.1016/0040-6090(82)90590-9.

- [196] J.-C. Zhang, L.-M. Xiong, M. Fang, and H.-B. He, “Wide-angle and broadband graded-refractive-index antireflection coatings,” *Chinese Phys. B*, vol. 22, no. 4, p. 044201, Apr. 2013, doi: 10.1088/1674-1056/22/4/044201.
- [197] X. Wu, Y. Tang, V. V. Silberschmidt, P. Wilson, and Z. Chen, “Mechanically Robust Transparent Anti-Icing Coatings: Roles of Dispersion Status of Titanate Nanotubes,” *Adv. Mater. Interfaces*, vol. 5, no. 18, pp. 1–10, 2018, doi: 10.1002/admi.201800773.
- [198] T. Sun, F. Álvarez-Novoa, K. Andrade, P. Gutiérrez, L. Gordillo, and X. Cheng, “Stress distribution and surface shock wave of drop impact,” *Nat. Commun.*, vol. 13, no. 1, p. 1703, Dec. 2022, doi: 10.1038/s41467-022-29345-x.

PUBLICATION

1

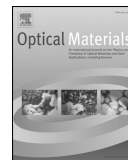
Influence of ex-situ annealing on the properties of MgF₂ thin films deposited by electron beam evaporation

J. Reuna, V. Polojärvi, P. Pääkkönen, K. Lahtonen, M. Raappana, T. Aho, R. Isoaho, A. Aho, M. Valden, and M. Guina

Optical Materials, vol. 96, p. 109326, Oct. 2019

<https://doi.org/10.1016/j.optmat.2019.109326>

Publication reprinted with the permission of the copyright holders.



Influence of ex-situ annealing on the properties of MgF₂ thin films deposited by electron beam evaporation

Jarno Reuna^{a,*}, Ville Polojärvi^a, Pertti Pääkkönen^{b,1}, Kimmo Lahtonen^{c,2}, Marianna Raappana^a, Timo Aho^a, Riku Isoaho^a, Arto Aho^a, Mika Valden^c, Mircea Guina^a

^a Optoelectronics Research Centre, Physics Unit, Faculty of Engineering and Natural Sciences, Tampere University, P.O. Box 692, FIN-33014, Tampere, Finland

^b Institute of Photonics, University of Eastern Finland, P.O. Box 111, FIN-80101, Joensuu, Finland

^c Surface Science Laboratory, Physics Unit, Faculty of Engineering and Natural Sciences, Tampere University, P.O. Box 692, FIN-33014, Tampere, Finland

ARTICLE INFO

Keywords:

Electron beam evaporation
Thin film coatings
Ellipsometry
Rapid thermal annealing (RTA)
X-ray photoelectron spectroscopy (XPS)

ABSTRACT

We report on the properties of magnesium fluoride (MgF₂) thin films deposited by electron beam evaporation as a function of substrate deposition temperature and ex-situ annealing temperature. In particular, we report on the dependence of refractive index on annealing temperature, which can be used as a tuning parameter of the optical properties. Mechanical and structural properties of the films influenced by the annealing are also examined. Changing the substrate temperature from 50 °C to 240 °C caused a decrease of the refractive index and the lowest value of 1.36 (measured at 632.8 nm) was achieved for the substrate temperature of 240 °C. Rapid thermal annealing further decreased the refractive indices to slightly below 1.32. This could indicate increase in the film porosity and removal of adsorbed water molecules. Prior annealing the film surfaces were very smooth with root mean square and mean roughness below 1 nm. Annealing above 700 °C changed the structure of the films drastically, as they started to form a granular structure, while an annealing temperature of 1000 °C increased the refractive index to a value as high as 1.5. Using X-ray photoelectron spectroscopy we show that the surface of the films consist mainly of Mg and F atoms, but also small traces of C and O are present. The Mg:F ratio remained essentially the same (43:57) between different deposition temperatures. To demonstrate the need for post-deposition annealing treatment, we have also studied the aging effect in the MgF₂ based anti-reflective coatings.

1. Introduction

MgF₂ is a widely used material for various kind of optical coatings [1–3]. Its relatively low refractive index of ~1.4 at visible wavelengths and wide transmission window from 0.11 to 4 μm [4] makes it a suitable low index material for optical coatings, such as anti-reflective coatings (ARC) and high reflectance dielectric mirrors. Multi-junction solar cells represent a specific application area where such ARCs are used, and where the specific optical properties of MgF₂ films present attractive features in terms of device performance, in particular in terms of achieving a broadband operation. To this end, thin film ARC structures utilized in multi-junction III–V semiconductor solar cells require non-absorbing high and low refractive index materials over a very broad wavelength range, extending from ultraviolet (UV) to beyond 1.5 μm, thus bringing considerable challenges for practical realization. For such coating MgF₂ is used as the low refractive index layer

[2,5,6]. We should note that not just refractive index values but also the material properties are utmost important when designing a structure that provides a low loss ARC while maintaining its functionality for a long time in varying environments. In this respect previous studies have demonstrated the effects of the deposition parameters on MgF₂ films employing electron beam evaporation [7], thermal evaporation [8,9], sputtering [10–13] and atomic layer deposition [14]. Moreover, studies focused on ion assisted deposition (IAD) showed some unwanted changes in film properties, like greater losses in the UV region and oxygen implantation [15]. It was also shown that IAD alone will not remove the need for substrate heating [16]. In this study we focus on identifying the interplay between the deposition parameters and the properties of MgF₂ thin films when employing electron beam (e-beam) evaporation. We focus in particular on the influence of the substrate temperature together with the post deposition annealing on the properties of MgF₂ with the aim to gain a good level of controllability over

* Corresponding author.

E-mail address: jarno.reuna@tuni.fi (J. Reuna).

¹ Spectroscopic ellipsometry measurements.

² XPS measurements.

the film properties.

2. Materials and methods

The MgF₂ thin films were deposited by a custom-built electron beam evaporator system. The device was assembled by Instrumentti Mattila Oy and it includes electron sources, crucibles, and sweep controls from Telemark Ltd and quartz monitoring from Intellemetrics Global Ltd. The system is essentially an improved bell jar vacuum chamber with two separate sections, one for materials and the electron source and another for samples. The sections are isolated with a gate valve, which enables using the upper chamber as a loading chamber. The vacuum level of the system is approximately 1×10^{-6} mbar. The films were evaporated from MgF₂ granules [17] in 16.3 cc tantalum liner. For electron beam creation we used Telemark's 7-1/2 turn tungsten filament and voltage of 8 keV with a total filament current between 4 and 8 mA. The electron beam was spiral shaped with a beam spot size approximately 3 cm². The evaporation rate was controlled via monitoring the filament current and the average deposition rate was kept at 0.3 nm/s. Substrate temperature (T_s) was measured from the backside of the steel substrate holder, where the holder temperature is approximated to be in thermal equilibrium with the substrate during the thin film deposition. The measurement utilized a K-type thermocouple for temperature monitoring and the heating of the substrates was done radiatively by halogen lamps.

The MgF₂ films were grown on 2" Si wafers and had a thickness of ~100 nm. The native monolayer oxide [18] on Si wafers was not removed prior to the growth and this was taken into account in spectroscopic ellipsometry measurements. Samples are identified by T_s as Ts50, Ts100, Ts150, Ts200 and Ts240, corresponding to 50 °C, 100 °C, 150 °C, 200 °C, and 240 °C, respectively. Subsequent to the growth, a test series of the samples was exposed to rapid thermal annealing (RTA) using JetFirst 100 annealing system from Jipelec Ltd. The annealing temperature T_a was varied from 300 °C to 1000 °C with 100 °C intervals. Inert N₂ atmosphere was used during temperature ramping while the annealing at the constant temperature was performed in a vacuum. Three of the annealed Ts200 samples were later characterized with atomic force microscope (AFM) and they are referred as Ts200Ta300, Ts200Ta700 and Ts200Ta900.

Film thicknesses and refractive indices of the MgF₂ layers were determined with a Rudolph AutoEL III Null ellipsometer equipped with a He/Ne laser at $\lambda = 632.8$ nm. The parameters for ellipsometric calculations were the refractive index of Si-substrate $n_s = 3.863$, substrate extinction coefficient $k_s = 0.162$ and the 70° angle of incidence. The refractive indices and film thicknesses in this study are average values of several measurements. For error limits we have used the standard deviation of single measurements, added the precision of the ellipsometer (refractive index 0.001, thickness 1 Å), and rounded up for consistent limits. For refractive index this gives an error limit of ± 0.002 and for normalized thickness an error limit of ± 0.02 a.u. with 90% level of confidence. These ellipsometric measurements were used to monitor film properties during environmental testing. The tests included measurements of the films i) as deposited, ii) after they were kept for two weeks in ambient conditions (22 °C, and relative humidity of 40%), iii) after they were soaked in water for 24 h, iv) after they were kept for a year in ambient conditions (again 22 °C and relative humidity of 40%), v) after short vacuum exposure (1 h at 1×10^{-5} mbar), and finally vi) after long vacuum exposure (3 h at 1×10^{-5} mbar and heating at 150 °C).

Spectroscopic ellipsometry was performed with a J.A.Woollam VASE spectral ellipsometer and the software used for material modelling was WVASE32® Version 3.774. All Psi and Delta ellipsometry function calculations were based on models incorporated in this software. A single oscillator Sellmeier approach was used to model the material refractive index and dispersion [19]. The uncertainty intervals for refractive indices were calculated using Sellmeier model parameter

with uncertainties reported by the WVASE software. This method does not take into account the possibility of a systematic error due to the cross-dependence of the material parameters and presumption of a normal distribution for the uncertainties.

X-ray photoelectron spectroscopy (XPS) measurements were performed utilizing a non-monochromatized Al K α X-rays (1486.6 eV) generated by DAR400 flood X-ray source (Omicron Nanotechnology GmbH) operated at 300 W for excitation of photoelectrons. The measurements were carried out in normal emission with detection area of 2.93 mm² ($\varnothing 1.93$ mm). The core level spectra were collected with a pass energy of 10 eV, producing a full width at half maximum (FWHM) of 1.09 eV for reference metallic Ag 3d_{5/2} peak, employing Argus hemispherical electron spectrometer (Omicron Nanotechnology GmbH) installed in a multifunctional ultra-high vacuum system with base pressure below 1×10^{-10} mbar [20].

The surface elemental concentrations and chemical states of compounds were identified by analyzing the core level photoemission spectra of C 1s, O 1s, Mg 2p, and F 2s using CasaXPS software Version 2.3.17PR1.1.2 [21]. The binding energy scale was calibrated according to the Mg 1s (MgF₂) component at 1305.0 eV. The spectral components were least-squares fitted with a combination of symmetric Gaussian–Lorentzian or asymmetric Lorentzian line shapes with tail damping followed by Shirley-type background subtraction. The relative atomic concentrations were calculated using Scofield's photoionization cross sections [22] and experimentally measured transmission function of the Argus analyzer. The sampling depths of the C 1s, O 1s, Mg 2p (~51 eV), and F 2s (~30 eV) signals in MgF₂ were calculated by TPP2M formula [23] and are 8.2, 6.8, 9.4, and 9.5 nm, respectively.

Scanning electron microscope (SEM) imaging was done with a SIGMA™ FESEM that was operated with SmartSEM® software, both products of Carl Zeiss NTS Ltd. Acceleration voltage was 1 kV and the aperture size was 10 μ m. For surface roughness measurements we used a Dimension™ 3100 AFM from Veeco Ltd and the image data was constructed with WSxM 5.0 Develop 8.2 software [24]. With these microscopic methods we obtained visual and numerical data of the structural quality of the MgF₂ films.

To test the aging performance of the e-beam evaporated MgF₂ we also designed two different ARCs for III–V multi-junction solar cells with Essential Macleod software [25] and measured the reflectance of the actual structures by using PerkinElmer Lambda 1050 spectrophotometer. The ARC structures were grown at 200 °C and did not have post-deposition RTA treatment. This T_s was chosen as a mid-value of supplier recommendations (150–250 °C) [17]. The ARC was designed for GaInP/GaAs/GaInNAsSb triple-junction solar cells with AlInP window layer [26]. The reflectance of ARCs were measured right after deposition and after exposure for a year in ambient conditions. The ARCs consisted of 103 nm MgF₂/56 nm TiO₂ and 76 nm MgF₂/39 nm Al₂O₃/50 nm TiO₂.

3. Results and discussion

In terms of optical properties, we assessed both the refractive indices and the extinction coefficients. The refractive indices measured by spectroscopic ellipsometry after deposition are plotted in Fig. 1. The measurements reveal a dependency of the refractive index on T_s , i.e. higher deposition temperature leads to a lower value of the refractive index. The decrease of refractive index as a function of fabrication temperature at selected wavelengths seems otherwise close to linear, except at the $T_s = 100$ °C. This exception could be linked to structural changes that start to take place around a substrate temperature of 100 °C.

The change of the refractive index is linked to the atomic structure of the films. MgF₂ thin films deposited by e-beam evaporation have been reported to start to crystallize at substrate temperatures above 250 °C [27] and to be partly amorphous and partly polycrystalline at temperatures below that [28]. As the densely packed amorphous

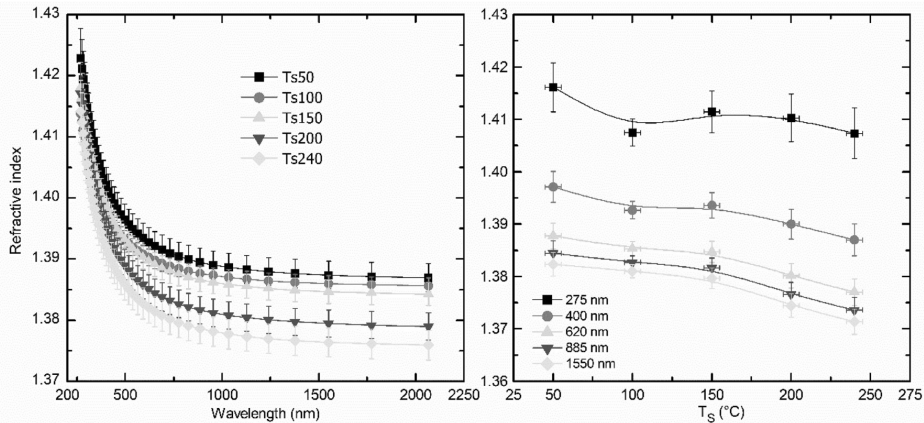


Fig. 1. Dispersion curves of the MgF_2 thin films and refractive index at selected wavelengths as a function of substrate temperature. The uncertainty bars represent 90% level of confidence.

domains start to form polycrystalline phases, they induce optically less dense structure, which lowers the refractive index. This decrease continues as a function of the deposition temperature, until the crystallization temperature ($\sim 250^\circ\text{C}$) after which the crystalline structure starts to get denser, leading to an increase in the refractive index [9]. The results presented in Fig. 1 are in agreement with the report of Dumas et al. [28], who showed that in the range of 30°C – 150°C the films are amorphous and in temperatures above 150°C the films start to be polycrystalline. The results in Fig. 1 are to be taken as effective refractive indices of the films, as we later show that the film structure is porous and thus the refractive index depends also on humidity. The films are kept, however, under the same environmental conditions, so their relative comparison is sensible.

The films Ts50 and Ts240 were measured with XPS to investigate their atomic compositions and possible impurities contained in the surface structure. Fig. 2 shows the corresponding survey spectra and high resolution spectra of low binding energy region. The Mg 2p and F 2s peaks were used in the calculation of film composition because the signals are close to each other in binding energy and thus have similar sampling depth. The main transitions of Mg 1s and F 1s were also recorded and used in the chemical identification (not shown here). In the XPS scans, we detected four elements: C, O, Mg and F. The small traces of C and O indicate impurities, like hydrocarbons and water, which are adsorbed to the film surface. The low amount of the C and O impurities correspond to less than one molecular layer.

Both samples Ts50 and Ts240 showed the same Mg:F atomic ratio of 43:57, which is in good agreement with the results of Jacob et al. [29], who showed that the atomic ratio of the film surface deviates a little from the stoichiometric value of the film. Table 1 summarizes the corresponding binding energies for each element, their FWHM and relative concentrations. The binding energies and binding energy differences of Mg 1s (1305 eV) and F 1s (685.5–685.8 eV) with reference also to C 1s (C–C/H) correspond to Mg–F bonding, not Mg–O or metallic Mg. Besides oxidized C species, the O 1s peak at 534.1 eV, detected only for the sample Ts50, could be associated with water [30]. As highlighted in red in Table 1, the photoelectron peaks of Mg (1s, 2s, 2p) and F (1s, 2s) are narrowed with increased deposition temperature indicating increasing structural ordering and/or chemical uniformity in the MgF_2 lattice, e.g., by crystallization and removal of impurities. This is in agreement with the presumption based on the refractive index profiles in Fig. 1 and the results of Dumas et al. [28].

Fig. 3 shows the refractive index values of the MgF_2 films during environmental tests. It is expected that during the long aging periods

the films have reached an equilibrium state with the environment and that the pores have been saturated with water. As the study done by Thornton and Harrison showed complete desorption of water molecules by exposing thin films to vacuum at 150°C [31], it can be expected that after the long vacuum treatment and heating, the films will no longer include significant amounts of adsorbed water molecules.

It is reasonable to expect that the porousness and thus the refractive index of the films would be directly comparable as a function of T_s . However, this is not the case right after the deposition, most likely due to partially adsorbed water during the evaporation. Ogura et al. [32] have shown that even during deposition there are some water molecules that get adsorbed to the pores of the film. As our refractive index measurements are done in ambient conditions, we are not able to calculate the actual packing density of the films, as the films already contain some amount of water. As the films age and they start to reach equilibrium with environmental conditions the order of the indices start to follow the assumptions we made based on the dispersion curves in Fig. 1. Soaking in water seems to have no effect on other samples than Ts50. This is likely to be caused by the difference in the pore size and structure, as with the smaller pore size the surface tension of water is high enough to prevent water diffusion to the pores within the used soaking time. When we compare the refractive indices of the water soaked samples to the index values of samples kept for about a year in ambient conditions, it can be concluded that the pores are not yet saturated with water due to the soaking. Furthermore, it can be seen that the short vacuum treatment is not capable of removing adsorbed water as the refractive indices still increase when compared to the values before vacuum treatment. As expected, the longer vacuum treatment with sufficient heating does remove adsorbed water from the film pores, but some hydroxyl groups are likely to remain on the surface of the film [31]. Fig. 3 shows that for the samples Ts100–Ts240 the film thickness remains rather stable as function of time. For Ts50 it would seem that after the deposition the film structure pulls together in the vertical direction of the wafer reducing the film thickness. This sort of a change in the film structure indicates relatively loose mechanical quality and high porousness.

Fig. 4 shows the surface morphology of the MgF_2 films and the cross-sectional film structure of samples Ts50 and Ts200 imaged with SEM. The images were taken after a year from the deposition.

It is clearly observable that the films deposited at temperatures below 200°C exhibited a large amount of micro-cracks. This influences the optical and mechanical properties of the film, as the cracks offer more sites for water vapor adsorption, which in turn modifies the

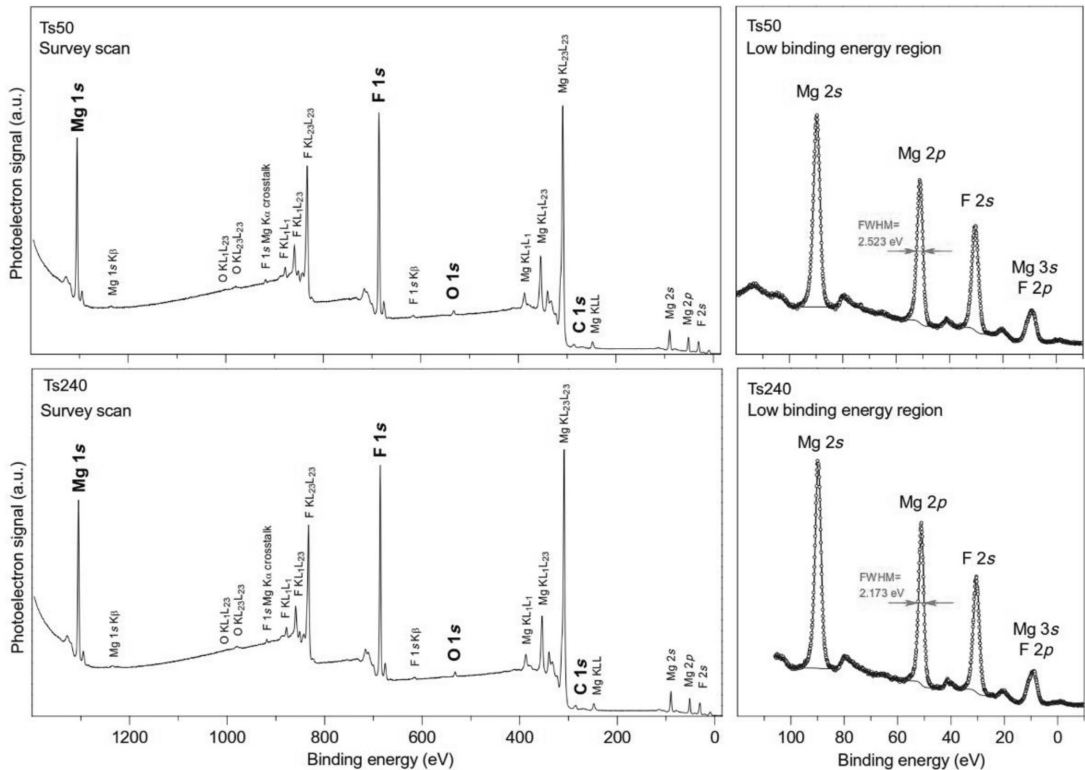


Fig. 2. XPS survey spectra (1400–0 eV) measurements and high resolution spectra (100–0 eV) of the MgF₂ thin films grown at temperatures of 50 °C and 240 °C.

effective refractive index, and decrease the abrasion resistance and the adhesion between the film and the substrate surface. Using such MgF₂ films evaporated at low temperature in multilayer structures would be problematic because micro-cracking could result in off-peeling of the coatings. In addition it seems that the cross-sectional columns of the film grown at 50 °C go through the entire film, while for the film grown at 200 °C the columns are somewhat shorter and more disoriented, thus creating a denser structure. The structural zone model (SZM) introduced by Movchan and Demchishin [33] and later revised by Thornton [34], suggests various film growth types according to the ratio of the T_s and the melting temperature of the film material T_m (both in Kelvins). For magnesium fluoride T_m is 1255 ± 3 °C [35] and the corresponding ratios of our samples are presented in Table 2.

According to the SZM, the samples Ts50, Ts100 and Ts150 belong to Zone T (ratio 0.1–0.3), which means that their structural growth is dominated by surface diffusion. This kind of growth is highly dependent

of the total energy of the particles that are forming the film, which in this case is dominated by the surface temperature. Lower temperature, thus lower surface energy, leads to creation of voids in the films and increases porosity. The samples Ts200 and Ts240 belong to Zone II (ratio > 0.3), where the films have high enough energy to start to form crystalline structure.

Fig. 5 Reveals the change of refractive index as a function of T_a . When annealed below 600 °C, the refractive index of Ts200 and Ts240 remain approximately unchanged, when compared to the as deposited values. However, the samples Ts50–Ts150 exhibit significantly lower refractive index values after the RTA treatment.

This behavior is most likely due to the removal of adsorbed water, which we have assumed to originate already from the deposition. This leaves behind voids of air ($n_{air} = 1.00$ vs $n_{water} = 1.33$) and decreases the refractive index. Calculations with effective medium approximations (EMA) [37] give us the ratios of air/MgF₂ in the films, which are

Table 1

XPS results for Ts50 and Ts240 showing the corresponding binding energies for each transition (E_B), the full width at half maximum of the peaks (FWHM) and the relative atomic concentration of the elements (C_x).

Sample		C 1s	O 1s	Mg 2p	F 2s	Mg: F	
		C–C/H	X–O(–H)	X–C=O/–O	Mg–F	Mg–F	
Ts50	C_x (at. %)	1.75	1.97	0.30	40.78	54.16	42.95 : 57.05
	E_B (eV)	284.78	287.37	534.14	51.00	30.28	
	FWHM (eV)	3.310	3.310	3.120	2.523	2.906	
Ts240	C_x (at. %)	2.57	1.83	–	40.27	53.41	42.99 : 57.01
	E_B (eV)	284.23	287.11	–	50.96	30.40	
	FWHM (eV)	2.930	2.930	–	2.173	2.686	

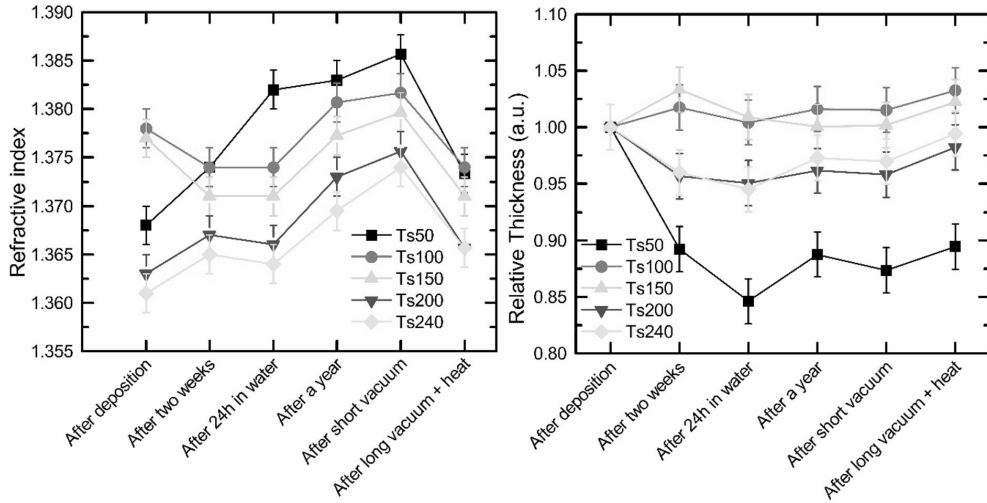


Fig. 3. Refractive indices and film thicknesses measured at $\lambda = 632.8$ nm of the MgF_2 thin films with different post deposition conditions. The uncertainty bars represent 90% level of confidence.

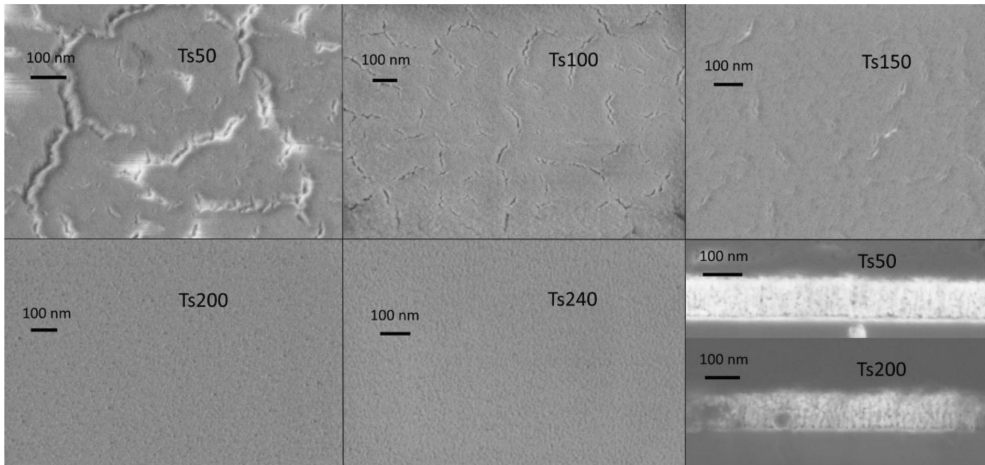


Fig. 4. Sample surfaces of the MgF_2 thin films imaged with SEM after a year exposure to ambient conditions and cross-sectional images of the samples grown in $50^\circ C$ and in $200^\circ C$.

Table 2

Calculated structure zone model ratios T_v/T_m .

Sample	Ts50	Ts100	Ts150	Ts200	Ts240
T_v/T_m	0.21	0.24	0.28	0.31	0.34

shown in Fig. 6. The calculations are based on assumptions that

- 1) The pores contain only air right after the annealing procedure ($f_{MgF_2} + f_{air} = 1$).
- 2) The MgF_2 skeleton has a refractive index of the bulk material $n = 1.378$ [36].
- 3) The films are transparent, so the dielectric constant follows equation $\epsilon = n^2$

Here f stands for the volume fraction of the film material expressed in the subscript. In EMA

$$f_{MgF_2}(\epsilon_{eff} - \epsilon_{MgF_2})/(\epsilon_{eff} + \epsilon_{MgF_2}) + f_{air}(\epsilon_{eff} - \epsilon_{air})/(\epsilon_{eff} + \epsilon_{air}) = 0, \quad (1)$$

from which we can derive

$$f_{air}/f_{MgF_2} = -((\epsilon_{eff} - \epsilon_{MgF_2})/(\epsilon_{eff} + \epsilon_{MgF_2}))/((\epsilon_{eff} - \epsilon_{air})/(\epsilon_{eff} + \epsilon_{air})) \quad (2)$$

The value ϵ_{eff} refers now to the effective dielectric constant of the deposited film, value ϵ_{MgF_2} to the bulk value and ϵ_{air} to the dielectric constant of air. Equation (2) reveals the relative amount of pores in the film and can be used to calculate the packing density p of the MgF_2 film, using

$$p = 1 - (f_{air}/f_{MgF_2}) \quad (3)$$

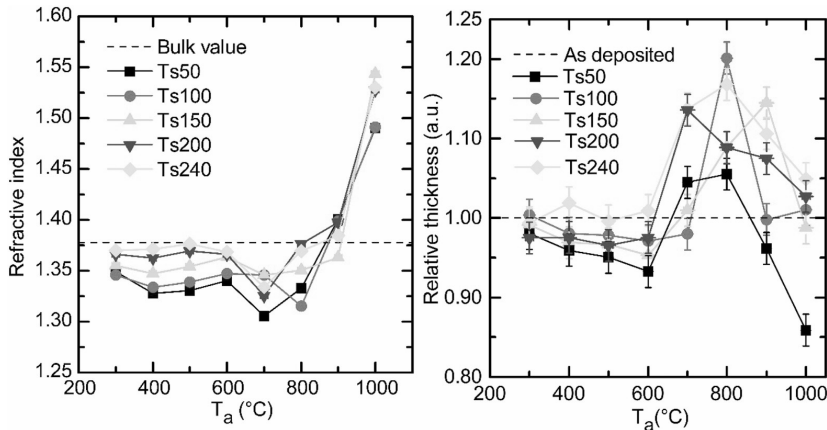


Fig. 5. Refractive indices and film thicknesses measured at $\lambda = 632.8$ nm of the MgF_2 thin films annealed in different temperatures. Bulk value by Heavens et al. [36]. The uncertainty bars represent 90% level of confidence.

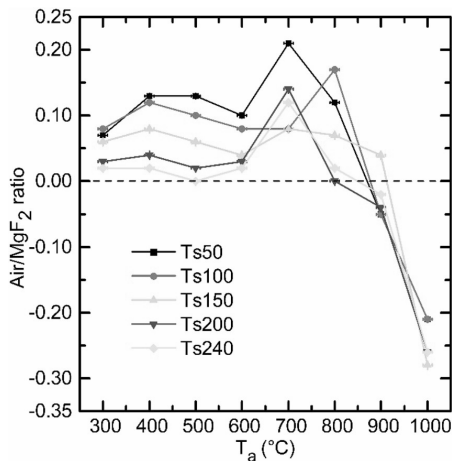


Fig. 6. Air/ MgF_2 ratio of the annealed thin film samples. The uncertainty bars represent 90% level of confidence.

The air/ MgF_2 ratios plotted in Fig. 6 indicate that increasing the T_a up to 600 °C improves the film quality and decreases the air content/porosity of the films, as a global minimum can be observed. At 700 °C a radical change occurs and the porosity of the films starts to increase again, after which the films seem to get denser than bulk MgF_2 based on refractive index comparison done in Fig. 5. It can also be stated that above 800 °C our assumptions for the EMA are no longer valid, which results to the negative values for air content.

As T_a increases to 700 °C the radical change of the film structure can also be seen in the film thicknesses shown in Fig. 5. The change is likely attributed to the lateral shrinkage of the films [38], which would also explain the rapid thickness increase.

Table 3
Surface roughness of the MgF_2 films measured by AFM.

Sample ID	Ts50	Ts100	Ts150	Ts200	Ts240	Ts200Ta300	Ts200Ta700	Ts200Ta900
R_{rms} [nm]	0.48	0.48	0.44	0.57	0.56	0.58	5.42	13.51
R_a [nm]	0.38	0.38	0.35	0.44	0.44	0.44	4.23	10.84

As the trends of refractive index and thickness as function of T_a are very similar between samples evaporated at different T_s , we chose few annealed test pieces of the sample Ts200 for closer examination with AFM. Table 3 presents the root mean square roughness (R_{rms}) and average roughness (R_a) values measured with AFM. Surface roughness affects adhesion between thin films [39] and increases surface scattering [40], which needs to be taken into account when designing an ARC.

The surface roughness values are in good agreement with the results of Atanassov et al. [27], who studied MgF_2 films deposited by e-beam evaporation in room temperature obtaining R_{rms} of 2.276 nm and after annealing in 350 °C for 3 h R_{rms} of 14.527 nm. Our results reveal that the surface roughness increases slightly as the T_s increases, although the sample Ts150 has the lowest roughness values of the samples. This could indicate increased ordering of the lattice structure between the lower temperatures and 150 °C. Annealing further increases the surface roughness and when combined with the film thickness results of Fig. 5 a coarse surface is expected. The related surface topologies are presented in Fig. 7. It can be seen that the lowest annealing temperature does not change the surface morphology. As T_a increases, the MgF_2 films start to form granular surfaces. The sample Ts200Ta700 consists of grains with a size of roughly 50–100 nm and the sample Ts200Ta900 has a grain size of around few hundreds of nanometers.

In addition, the structural change of the annealed samples can be linked to the SZM, as has been presented by Gupta et al. [41]. According to this model, T_a/T_m ratio values between 0.25 and 0.35 correspond to the Zone T of SZM. Values higher than 0.35 can be linked to major grain growth that leads to porousness and cracking of the film. Table 4 shows the SZM ratios of the annealed samples investigated by AFM.

Based on Figs. 5 and 7 it is clear that MgF_2 films treated with RTA do not straightforwardly follow the model introduced by Gupta et al. [41]. Instead, the change from Zone T to the grain growth zone, seems to occur between 600 and 800 °C which corresponds roughly to a ratio of 0.6. The difference could be explained by shorter annealing time in our case or the overall accuracy of SZM when applied to annealed

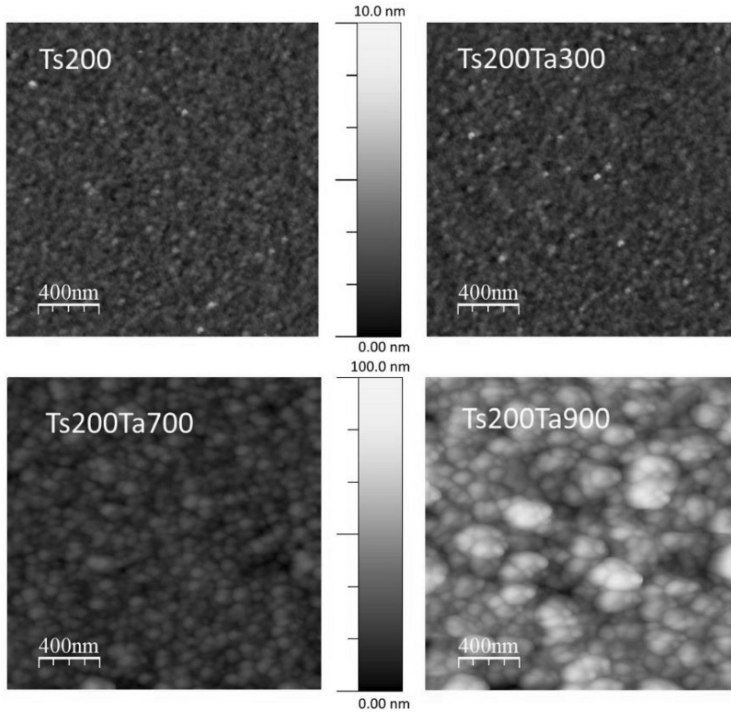


Fig. 7. Surface topology maps measured with AFM of the annealed MgF₂ thin films, initially evaporated at 200 °C and then annealed in 300 °C, 700 °C and 900 °C.

Table 4
Calculated structure zone model ratios T_n/T_m for annealed samples.

Sample	Ts200Ta300	Ts200Ta700	Ts200Ta900
T_n/T_m	0.38	0.64	0.77

samples.

The performance over time for the two test ARCs are shown in Fig. 8. It can be seen that both ARC structures decrease the average

reflectance of the un-coated solar cell, roughly 30% at the visible wavelengths and then the reflectance slowly increases towards the infrared bandwidth. Ideally for multi-junction solar cells, the reflectance should remain below 5% from UV to 1.5 μm [42]. The ARCs exhibit some deterioration in their performance, as the average reflectance increases, due to prolonged exposure to ambient conditions. This is likely due to small amounts of adsorbed water. On average the absolute difference in reflectance for the double layer structure is 1.1%, while for the triple layer it is only 0.5%. The absolute reflectance difference is higher near

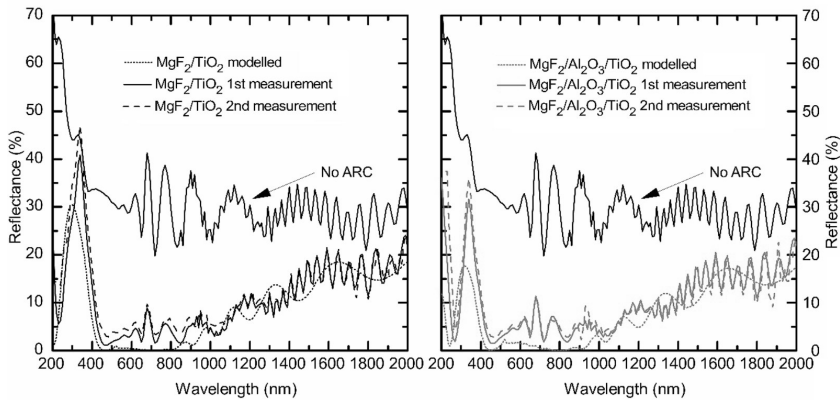


Fig. 8. Reflectance measurements of two different ARCs on a triple-junction solar cell right after deposition (1st measurement) and after a year exposure to ambient conditions (2nd measurement) and as a comparison the reflectance for the simulated design of the both ARC structures on top of the solar cell.

the UV region, and between 300 and 400 nm the values are 5.2% for the double layer structure and 3.2% for the triple layer structure.

To reach the highest efficiencies, multi-junction solar cells need to be current matched between the different junctions [43]. If the reflectance increases due time, the solar cell performance decreases, as the current balance changes [44]. Therefore the long time functionality of the coating needs to be further improved by decreasing the porosity of the MgF₂ film. This could be done by increasing the growth temperature or possibly by more effective post-growth annealing process. However, this would require also parametrization of the other layer materials to find suitable fabrication conditions for the entire ARC structure.

4. Conclusions

The properties of MgF₂ thin film structures deposited by e-beam evaporation at different substrate temperatures and subjected to post-growth annealing are reported. It was found that the growth temperature has a large impact both on the optical and structural properties without changing the Mg:F ratio of the film surface. When the T_s is increased from 50 °C to 240 °C the refractive index decreases and, on the other hand, temperatures below 200 °C lead to high porosity and micro-cracking. Due to the porosity, the film quality is more affected by humidity, which results in changes for the optical coating properties. Heating and vacuum treatment showed that the water trapping is partly a reversible process and that the films grown at higher temperature are less prone to changes in the quality due time or environmental effects. The high temperature (> 200 °C) evaporated MgF₂ films have more suitable properties for optical coatings, as they are mechanically more durable and provide a more stable refractive index that is less prone to humidity shifts.

While the films already contain small amounts of water during the deposition, the RTA process is effective in removing the water and results in improving the film quality. Excess heating, however, shrinks the films and changes their atomic structure drastically. Ellipsometric measurements suggests that the film structure can be improved at temperatures up until 600 °C. At 600 °C the porosity of the samples Ts50-Ts240 showed lowest values and no shrinkage was observed.

The functionality of MgF₂ layer for long lasting practical applications was assessed by fabricating ARCs containing MgF₂ films grown at 200 °C. The study showed that even though the mechanical quality was good, as there was no micro-cracking, the optical performance was still negatively affected by humidity. Further study would aim to test more complex multilayer designs with post-deposition RTA, to reduce the influence of humidity and long term exposure to ambient conditions. To this end, it seems beneficial to develop an effective post-deposition RTA process including the other ARC materials.

Funding

The research leading to these results has received funding from the European Research Council under the European Union's H2020 Framework [ERC-2015-AdG 695116] and Academy of Finland [Decision Number 286713]. Main author acknowledges personal support from the Fortum Foundation [201600119].

Declaration of competing interest

The authors declare that they have no known competing financial interests or personal relationships that could have appeared to influence the work reported in this paper.

References

- [1] M.A. Butt, S.A. Fomchenkov, A. Ullah, P. Verma, S.N. Khonina, Biomedical band-pass filter for fluorescence microscopy imaging based on TiO₂/SiO₂ and TiO₂/

- MgF₂ dielectric multilayers, *J. Phys. Conf. Ser.* 741 (2016) 012136, <https://doi.org/10.1088/1742-6596/741/1/012136>.
- [2] S.E. Lee, S.W. Choi, J. Yi, Double-layer anti-reflection coating using MgF₂ and CeO₂ films on a crystalline silicon substrate, *Thin Solid Films* 376 (2000) 208–213, [https://doi.org/10.1016/S0040-6090\(00\)01205-0](https://doi.org/10.1016/S0040-6090(00)01205-0).
- [3] G. Kedawat, S. Srivastava, V.K. Jain, P. Kumar, V. Kataria, Y. Agrawal, B.K. Gupta, Y.K. Vijay, Fabrication of artificially stacked ultrathin ZnS/MgF₂ multilayer dielectric optical filters, *ACS Appl. Mater. Interfaces* 5 (2013) 4872–4877, <https://doi.org/10.1021/am400612q>.
- [4] H.K. Pulker, Characterization of optical thin films, *Appl. Opt.* 18 (1979) 1969, <https://doi.org/10.1364/AO.18.001969>.
- [5] S. Liu, Y.-H. Zhang, MgF₂/ZnS double-layer anti-reflection coating design for ultrathin GaAs single-junction solar cells, *Renew. Energy Environ. OSA*, Washington, D.C., 2013, <https://doi.org/10.1364/OSE.2013.RM4D.5.RM4D.5>.
- [6] C.E. Valdivia, E. Desfonds, D. Masson, S. Fafard, A. Carlson, J. Cook, T.J. Hall, K. Hinzner, Optimization of antireflection coating design for multijunction solar cells and concentrator systems, *Proc. SPIE* 7099 (2008) 709910–709915, <https://doi.org/10.1117/12.807675>.
- [7] L. Dumas, E. Quesnel, J.-Y. Robic, Y. Pauleau, Characterization of magnesium fluoride thin films deposited by direct electron beam evaporation, *J. Vac. Sci. Technol. A* 18 (2000) 465–469 <https://doi.org/10.1116/1.582210>.
- [8] F. Perales, C. de las Heras, F. Agulló-Rueda, Structural properties of MgF₂ and ZnS in thin film and in multilayer optical coatings, *J. Phys. D Appl. Phys.* 41 (2008) 225405, <https://doi.org/10.1088/0022-3727/41/22/225405>.
- [9] H. Yu, H. Qi, Y. Cui, Y. Shen, J. Shao, Z. Fan, Influence of substrate temperature on properties of MgF₂ coatings, *Appl. Surf. Sci.* 253 (2007) 6113–6117, <https://doi.org/10.1016/j.apsusc.2007.01.037>.
- [10] J.I. Larruquert, R.A.M. Keski-Kuha, Far ultraviolet optical properties of MgF₂ films deposited by ion-beam sputtering and their application as protective coatings for Al, *Opt. Commun.* 215 (2002) 93–99, [https://doi.org/10.1016/S0030-4018\(02\)02229-0](https://doi.org/10.1016/S0030-4018(02)02229-0).
- [11] J. Mashaiekh, Z. Shafeizadeh, H. Nahidi, I. Hadi, Effect of deposition method on the optical and microstructural properties of vacuum-deposited MgF₂ thin films, *Optik* 124 (2013) 3957–3961, <https://doi.org/10.1016/j.jilco.2013.03.018>.
- [12] S. Mertin, L. Marot, C.S. Sandu, R. Steiner, J.-L. Scartezzini, P. Murali, Nanocrystalline low-refractive magnesium fluoride films deposited by reactive magnetron sputtering: optical and structural properties, *Adv. Eng. Mater.* 17 (2015) 1652–1659, <https://doi.org/10.1002/adem.201500129>.
- [13] E. Quesnel, L. Dumas, D. Jacob, F. Peiró, Optical and microstructural properties of MgF₂ UV coatings grown by ion beam sputtering process, *J. Vac. Sci. Technol. A Vac. Surf. Films* 18 (2000) 2869–2876, <https://doi.org/10.1116/1.1290374>.
- [14] T. Pilvi, T. Hatanpää, E. Puukilainen, K. Arstila, M. Bischoff, U. Kaiser, N. Kaiser, M. Leskela, M. Ritala, Study of a novel ALD process for depositing MgF₂ thin films, *J. Mater. Chem.* 17 (2007) 5077–5083, <https://doi.org/10.1039/B710903B>.
- [15] P.J. Martin, W.G. Sainy, R.P. Netterfield, D.R. McKenzie, D.J. Cockayne, S.H. Sie, O.R. Wood, H.G. Craighead, Influence of ion assistance on the optical properties of MgF₂, *Appl. Opt.* 26 (1987) 1235–1239, <https://doi.org/10.1364/AO.26.001235>.
- [16] R.R. Willey, W. Optical, Improved magnesium fluoride process by ion-assisted deposition, *53rd Annu. Tech. Conf. Proc.* 2010, pp. 313–319.
- [17] Magnesium fluoride MgF₂ for optical coating, (n.d.). <https://materion.com/ResourceCenter/ProductData/InorganicChemicals/Fluorides/MagnesiumFluorideMgF2forOpticalCoating.aspx>.
- [18] M. Morita, T. Ohmi, E. Hasegawa, M. Kawakami, M. Ohwada, Growth of native oxide on a silicon surface, *J. Appl. Phys.* 68 (1990) 1272–1281, <https://doi.org/10.1063/1.347181>.
- [19] B. Tatian, Fitting refractive-index data with the Sellmeier dispersion formula, *Appl. Opt.* 23 (1984) 4477, <https://doi.org/10.1364/AO.23.004477>.
- [20] K. Lahtonen, M. Lampimäki, P. Jussila, M. Hirsimäki, M. Valden, Instrumentation and analytical methods of an x-ray photoelectron spectroscopy-scanning tunneling microscopy surface analysis system for studying nanostructured materials, *Rev. Sci. Instrum.* 77 (2006), <https://doi.org/10.1063/1.2221539>.
- [21] N. Fairley, CasaXPS: Spectrum Processing Software for XPS, AES and SIMS, Version 2.3.17 PR 1.1, Casa Software Ltd., Cheshire, UK, 2009 2009 <http://www.casaxps.com/>.
- [22] J.H. Scofield, Hartree-Slater subshell photoionization cross-sections at 1254 and 1487 eV, *J. Electron. Spectrosc. Relat. Phenom.* 8 (1976) 129–137, [https://doi.org/10.1016/0368-2048\(76\)80015-1](https://doi.org/10.1016/0368-2048(76)80015-1).
- [23] S. Tanuma, C.J. Powell, D.R. Penn, Calculations of electron inelastic mean free paths. V. data for 14 organic compounds over the 50–2000 eV range, *Surf. Interface Anal.* 21 (1994) 165–176, <https://doi.org/10.1002/sia.740210302>.
- [24] I. Horcas, R. Fernández, J.M. Gómez-Rodríguez, J. Colchero, J. Gómez-Herrero, A.M. Baro, WsXM: A software for scanning probe microscopy and a tool for nanotechnology, *Rev. Sci. Instrum.* 78 (2007) 1–8, <https://doi.org/10.1063/1.2432410>.
- [25] Essential Macleod Optical Coating Design Program - User's Manual, Version 8.11, Thin Film Center Inc, 1999.
- [26] Arto Aho, Dilute Nitride Multijunction Solar Cells Grown by Molecular Beam Epitaxy Julkaisu 1343 • Publication 1343 Tampere 2015 Dilute Nitride Multijunction Solar Cells Grown by Molecular Beam Epitaxy, (2015).
- [27] G. Atanassov, J. Turlo, J.K. Fu, Y.S. Dai, Mechanical, optical and structural properties of TiO₂ and MgF₂ thin films deposited by plasma ion assisted deposition, *Thin Solid Films* 342 (1999) 83–92 [https://doi.org/10.1016/S0040-6090\(98\)01407-2](https://doi.org/10.1016/S0040-6090(98)01407-2).
- [28] L. Dumas, E. Quesnel, J.-Y. Robic, Y. Pauleau, Characterization of magnesium fluoride thin films deposited by direct electron beam evaporation, *J. Vac. Sci. Technol. A Vac. Surf. Films* 18 (2000) 465, <https://doi.org/10.1116/1.582210>.

- [29] D. Jacob, F. Peiró, E. Quesnel, D. Ristau, Microstructure and composition of MgF₂ optical coatings grown on Si substrate by PVD and IBS processes, *Thin Solid Films* 360 (2000) 133–138, [https://doi.org/10.1016/S0040-6090\(99\)00738-5](https://doi.org/10.1016/S0040-6090(99)00738-5).
- [30] National Institute of Standards and Technology, Gaithersburg, NIST X-Ray Photoelectron Spectroscopy Database, Version 4.1, (2012), <https://doi.org/10.18434/T4T88K>.
- [31] E.W. Thornton, P.G. Harrison, Tin oxide surfaces. Part 1.—surface hydroxyl groups and the chemisorption of carbon dioxide and carbon monoxide on tin(IV) oxide, *J. Chem. Soc., Faraday Trans. 1 Phys. Chem. Condens. Phases* 71 (1975) 461, <https://doi.org/10.1039/f19757100461>.
- [32] S. Ogura, N. Sugawara, R. Hiraga, Refractive index and packing density for MgF₂ films: correlation of temperature dependence with water sorption, *Thin Solid Films* 30 (1975) 3–10, [https://doi.org/10.1016/0040-6090\(75\)90298-9](https://doi.org/10.1016/0040-6090(75)90298-9).
- [33] A.V. Movchan, B.A. Demchishin, Structure and properties of thick condensates of nickel, titanium, tungsten, aluminum oxides, and zirconium dioxide in vacuum, *Phys. Met. Metallogr.* 28 (1969).
- [34] J.A. Thornton, High rate thick film growth, *Annu. Rev. Mater. Sci.* 7 (1977) 239–260, <https://doi.org/10.1146/annurev.ms.07.080177.001323>.
- [35] A. Duncanson, R.W.H. Stevenson, Some properties of magnesium fluoride crystallized from the melt, *Proc. Phys. Soc.* 72 (1958) 1001–1006, <https://doi.org/10.1088/0370-1328/72/6/308>.
- [36] O.S. Heavens, S.D. Smith, Dielectric thin films, *J. Opt. Soc. Am.* 47 (1957) 469, <https://doi.org/10.1364/JOSA.47.000469>.
- [37] V.A. Markel, Introduction to the Maxwell Garnett approximation: tutorial, *J. Opt. Soc. Am. A* 33 (2016) 1244, <https://doi.org/10.1364/JOSAA.33.001244>.
- [38] D.L. Deadmore, J.S. Machin, A.W. Allen, Stability of inorganic fluorine-bearing compounds: I, binary metallic fluorides, *J. Am. Ceram. Soc.* 44 (1961) 105–109, <https://doi.org/10.1111/j.1151-2916.1961.tb13722.x>.
- [39] A. Çolak, H. Wormeester, H.J.W. Zandvliet, B. Poelsema, Surface adhesion and its dependence on surface roughness and humidity measured with a flat tip, *Appl. Surf. Sci.* 258 (2012) 6938–6942, <https://doi.org/10.1016/j.apsusc.2012.03.138>.
- [40] H.E. Bennett, J.O. Porteus, Relation between surface roughness and specular reflectance at normal incidence, *J. Opt. Soc. Am.* 51 (1961) 123, <https://doi.org/10.1364/JOSA.51.000123>.
- [41] V. Gupta, A. Mansingh, Influence of postdeposition annealing on the structural and optical properties of sputtered zinc oxide film, *J. Appl. Phys.* 80 (1996) 1063–1073, <https://doi.org/10.1063/1.362842>.
- [42] C.E. Valdivia, E. Desfonds, D. Masson, S. Fafard, A. Carlson, J. Cook, T.J. Hall, K. Hinzler, R. Vallée, M. Piché, P. Mascher, P. Cheben, D. Côté, S. LaRochelle, H.P. Schriemer, J. Albert, T. Ozaki (Eds.), Optimization of Antireflection Coating Design for Multijunction Solar Cells and Concentrator Systems, *Photonics North*, 2008709915, , <https://doi.org/10.1117/12.807675>.
- [43] W. Guter, J. Schöne, S.P. Philipps, M. Steiner, G. Siefer, A. Wekkeli, E. Welsler, E. Oliva, A.W. Bett, F. Dimroth, Current-matched triple-junction solar cell reaching 41.1% conversion efficiency under concentrated sunlight, *Appl. Phys. Lett.* 94 (2009) 223504, , <https://doi.org/10.1063/1.3148341>.
- [44] D.J. Aiken, Antireflection coating design for series interconnected multi-junction solar cells, *Prog. Photovolt. Res. Appl.* 8 (2000) 563–570, [https://doi.org/10.1002/1099-159X\(200011/12\)8:6 <563::AID-PIP327 >3.0.CO;2-8](https://doi.org/10.1002/1099-159X(200011/12)8:6 <563::AID-PIP327 >3.0.CO;2-8).

PUBLICATION
2

Optimization of Reactive Ion Beam Sputtered Ta₂O₅ for III–V Compounds

J. Reuna, M. Vuorinen, R. Isoaho, A. Aho, S. Mäkelä, A. Hietalahti E. Anttola, A.
Tukiainen, M. Guina

Thin Solid Films, revised (4.10.2022), with editor

<https://doi.org/XXX>

Publication reprinted with the permission of the copyright holders.

PUBLICATION

3

Use of nanostructured alumina thin films in multilayer anti-reflective coatings

J. Reuna, A. Aho, R. Isoaho, M. Raappana, T. Aho, E. Anttola, A. Hietalahti, A. Tukiainen and M. Guina

Nanotechnology, vol. 32, no. 21, p. 215602, May 2021

[https://doi.org/ 10.1088/1361-6528/abe747](https://doi.org/10.1088/1361-6528/abe747)

Publication reprinted with the permission of the copyright holders.

Use of Nanostructured Alumina Thin Films in Multilayer Anti-Reflective Coatings

Jarno Reuna^{a,1}, Arto Aho^a, Riku Isoaho^a, Marianna Raappana^a, Timo Aho^a, Elina Anttola^a, Arttu Hietalahti^a, Antti Tukiainen^a, Mircea Guina^a

^a *Optoelectronics Research Centre, Physics Unit, Faculty of Engineering and Natural Sciences, Tampere University, P.O. Box 692, FIN-33014 Tampere, Finland*

¹Corresponding author: jarno.reuna@tuni.fi

Keywords: De-Ionized Water, Thin film coatings, Porosity, Aluminum Oxide, Multilayer

Abstract

A new method for modification of planar multilayer structures to create nanostructured aluminum oxide anti-reflection coatings is reported. The method is non-toxic and low-cost, being based on treatment of the coating with heated de-ionized water after the deposition of aluminum oxide. The results show that the method provides a viable alternative for attaining a low reflectance ARC. In particular, a low average reflectivity of ~3.3 % is demonstrated in a broadband spectrum extending from 400 nm to 2000 nm for ARCs deposited on GaInP solar-cells, the typical material used as top-junction in solar cell tandem architectures. Moreover, the process is compatible with volume manufacturing technologies used in photovoltaics, such as ion beam sputtering and electron beam evaporation.

1. Introduction

Aluminum oxide (Al_2O_3) is a versatile non-toxic low refractive index insulator widely used in optical coatings^{1,2} and passivation layers³⁻⁵. It can be deposited by a wide range of thin film technologies, including electron-beam (e-beam) evaporation⁶, ion beam sputtering (IBS)⁷, plasma-enhanced chemical deposition (PECVD)⁸, atomic layer deposition (ALD)^{5,9}, pulsed laser deposition (PLD)², radiofrequency (RF)¹⁰ and direct current (DC)¹¹ sputtering. Alumina is known to be an amphoteric substance¹² and to form porous structures via anodic growth^{13,14} and sol-gel

processes^{15,16}. These material properties could be utilized in controlled corrosion process to fabricate nanoporous Al₂O₃ thin film with anti-reflective functionalities.

Porous nanostructures have successfully been utilized in advanced solar cell anti-reflective coatings (ARC), where they have enabled broadband operation and very low average reflectivity^{17,18}. Many of these nanostructures have exploited bio-mimicked concepts, i.e. moth-eye structures fabricated by nanoimprinting lithography^{18,19}, but also lithography free methods have been developed^{20,21}. The lithography free processes offer more streamlined manufacturing when compared to multi-step lithography methods. In addition to the low average reflectance, the nanostructures can offer longer optical paths within the solar cell by enhancing the surface scattering, which results in better absorption of light in the solar cell junctions and increases the total conversion efficiency^{19,22}. Combining a nanoporous top layer with traditionally used multilayer (ML) ARC for III–V solar cells could offer even better performance over broader spectral window^{23,24}; yet in terms of making this a feasible approach for wider use one would like to avoid multi-step post-coating processing.

Recent studies have shown that amorphous thin film Al₂O₃ forms porous structure when treated with heated de-ionized water (DIW)^{10,25}. Kauppinen *et al.*²⁵ have studied and developed a process to utilize the instability of ALD deposited alumina with DIW to fabricate porous anti-reflective coating for glass and black silicon solar cells. Additionally, Dokmai *et al.*¹⁰ have studied RF sputtered alumina films taking a closer look to the process mechanism of alumina corrosion in DIW. A potentially interesting possibility is also to use DIW-induced processes for fabrication of porous Al₂O₃ nanostructure using deposition techniques routinely employed in fabrication of multilayer broadband ARCs, namely e-beam and IBS. Benefits of these commonly used deposition methods include fast coating cycles, relatively fast growth rates (0.2-2 μm/h) and ability to use several different materials in one deposition run, which enables single-run deposition of the suggested ML ARC.

To this end, we demonstrate the formation of porous nanostructured alumina fabricated by the DIW driven process and integrated as a topmost layer of a planar multilayer ARC deposited by e-beam and IBS. By combining alumina with materials typically used for planar ARCs, such as titanium dioxide (TiO₂), having a relatively high refractive index enables maximizing the ARC functionality over a wider spectrum. Such broadband ARC structures are especially needed for

high efficiency III–V multijunction solar cells²⁶ where a cost effective and volume reproducible technology for coating deposition is a must.

2. Methods

Purpose of any ML ARC is to form a destructive set of interference that cancels out any reflections induced by the coated structure and to minimize the refractive index difference between the surrounding media (usually air) and the last layer of the thin film stack. Here we have used transfer matrix method (TMM)^{27–29} to design and simulate both the traditional planar ML structure and the nanostructured Al₂O₃ layer on top of it, as well as to model the III–V solar cell beneath the coating.

E-beam Al₂O₃ was evaporated using a custom-built evaporator by Instrumentti Mattila Oy; the system includes an electron source, a crucible, sweep controls from Telemark Ltd, and a quartz monitoring from Intellemetrics Global Ltd. The system base pressure prior to evaporation is approximately 1×10^{-5} mbar and the electron beam is formed with Telemark's 7-1/2 turn tungsten filament. The deposition temperature was 150 °C, as measured from the backside of the steel substrate holder, where the holder temperature is approximated to be in thermal equilibrium with the substrate during the thin film deposition. The measurement utilized a K-type thermocouple for temperature monitoring and the heating of the substrates was done radiatively by halogen lamps. As evaporation material we used Al₂O₃ granules with the size of 1.5-4 mm and with a purity of 99.99 %. Evaporation parameters for all used oxides are given in the Appendix A.

IBS alumina was deposited with Navigator 700 sputtering system (Cutting Edge Coatings GmbH). Sputtering was done using Ar:O₂ gas mixture with a flow ratio of 8:5 sccm ensuring a reactive O₂ atmosphere with a pressure of 4.5×10^{-4} mbar. A 200 × 200 mm aluminum plate with purity of 99.999 % was used as the target. Sputtering voltage was 1.26 kV and the RF power of the ion source was 102 W. During the deposition, the sample holder was rotated at 60 rpm to guarantee uniform deposition. The thickness was controlled via *in-situ* broadband optical monitoring, which measures the transmittance of a transparent monitoring substrate and fits the measurement data to the theoretical spectrum calculated with the refractive indices and extinction coefficients of the given materials. The sputtering parameters for all oxides used are given in the Appendix A.

The DIW used in the treatment had a resistivity of 18.4 MΩ and was kept in glass beakers pre-heated to temperature of 90 °C on a hotplate before sample immersion. The temperature of the

solution was constantly monitored during the treatment and no agitation was used. Treatment time was kept constant at 30 minutes. Several characterization samples for DIW treatment were deposited on silicon (Si) wafer pieces, without removing the native oxide³⁰ from the substrate.

The film thicknesses and refractive indices of the dielectric layers were determined with a Rudolph AutoEL III Null ellipsometer equipped with a He/Ne laser at $\lambda = 632.8$ nm. As parameters for ellipsometric calculations we used a refractive index of Si-substrate $n_s = 3.863$, a substrate extinction coefficient $k_s = 0.162$, and an angle of incidence of 70° . The refractive indices and film thicknesses in this study are average values of several measurements. The error limits have been calculated for 95 % level of confidence and then added the precision of the ellipsometer (refractive index 0.001, thickness 1 Å). For refractive index this gives an error limit of ± 0.002 and for thickness an error limit of ± 2 Å.

Scanning electron microscope (SEM) images were taken with a SIGMATM FESEM operated with SmartSEM[®] software, both products of Carl Zeiss NTS Ltd. Acceleration voltage was 1 kV and the aperture size was 10 μm . For surface roughness measurements we used a DimensionTM 3100 Atomic force microscope (AFM) from Veeco Ltd and the image data was constructed with WSxM 5.0 Develop 8.2 software³¹. For grazing incidence x-ray diffraction (GIXRD) measurements a PANalytical X'Pert³ MRD system was used.

For the transmission and the reflectance measurements of the deposited thin films we used a PerkinElmer Lambda 1050 UV/VIS/NIR spectrophotometer. Reflectance was measured at 8° angle of incidence, which is the smallest measurable angle when using the universal reflectance accessory module. The transmittance was measured with normal angle of incidence by using Scan Lambda 1050 transmittance module. The measured data was also used for simulations and fitting of the optical properties of the alumina, which was done with *Essential Macleod*© thin film software, that calculates the structures using TMM. Figure 1 shows the starting point for our approximation of the reflectivity of the porous Al_2O_3 and how the optical properties can be calculated by transforming the structure to very thin finite layers of varying refractive index, so called rugate design. In the model, n_m is the refractive index of the film material and n_i is the refractive index of the incident medium.

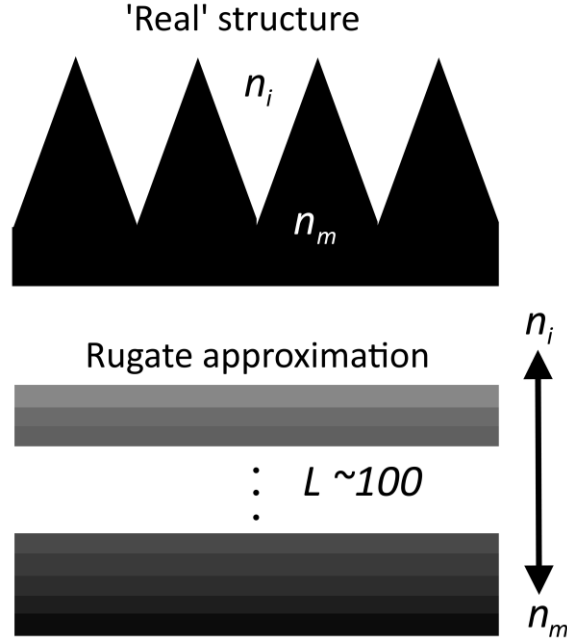


Fig. 1. Rugate filter principle for fitting optical properties of porous Al_2O_3 films.

In the rugate design we vary the packing density of the film material of each individual layer (L), which in turn scales the refractive index according to the Maxwell-Garnett approximations^{32,33}. The simulation for the packing density of each layer follows the equation:

$$\rho_L = 1 - (1 - (N - L)/N) , \quad (1)$$

where ρ_L is the packing density of the current layer, N is the total number of layers and L is the current layer number. The refractive index of each layer is calculated with the equation:

$$n_L = \rho \cdot n_m , \quad (2)$$

where n_L is the refractive index of an individual layer and n_m is the refractive index of the film material. For the simulations we started with 100 layers with the total thickness of the stack being 0.25 quarter wavelength of optical thickness at the wavelength of 633 nm. Then we used the Simplex© algorithm provided by the software to match the functionality of the stack to the spectrophotometer measurements by altering the physical thicknesses of the layers. The starting designs and fitted rugate layer values for the nanostructured alumina are given in the Appendix B.

Finally, when it comes to methodology, we should mention that the ARC performance of the film was tested on single-junction n-on-p GaInP solar cells, which were grown by molecular beam epitaxy on GaAs substrates using a Veeco GEN20 MBE system.

3. Results

To be able to process the ARC with DIW treatment, we needed to make sure that the other material components regularly used in optical coatings by e-beam and IBS would not be as prone to morphological changes as the alumina. Good measure of the film properties before and after DIW treatment is gained by ellipsometry that gives both thickness and refractive index of the film. The ellipsometry results for different e-beam and IBS oxides are shown in Table 1.

Table 1 Ellipsometry results for the oxides analyzed before and after DIW treatment. Refractive indices ± 0.002 and thicknesses $\pm 2 \text{ \AA}$ with 95 % level of confidence.

		Material	Before DIW	After DIW	Difference [%]
IBS	n (@633nm)	Al ₂ O ₃	1.671	N/A	N/A
			1217	N/A	N/A
	Thick. [\AA]	SiO ₂	1.483	1.481	-0.2
			1025	1014	-1.1
	TiO ₂	2.372	2.370	-0.1	
		1046	1043	-0.3	
Ta ₂ O ₅	2.110	2.109	-0.1		
	743	740	-0.4		
E-beam	n (@633nm)	Al ₂ O ₃	1.583	N/A	N/A
			1245	N/A	N/A
	Thick. [\AA]	SiO ₂	1.449	1.444	-0.3
			907	875	-3.5
	TiO ₂	2.177	2.170	-0.3	
		514	510	-0.7	
Ta ₂ O ₅	1.948	1.930	-0.9		
	632	630	-0.3		

For Al₂O₃ we were unable to calculate the refractive index and thickness of the films after the DIW treatment. With monochromatic ellipsometry this can mean inhomogeneous layer structure, which

indicates that some morphological changes took place for alumina films during DIW immersion. Other tested oxide materials showed little to no change in film properties due to the treatment. To verify what happened to the alumina films during DIW treatment, we imaged the samples with SEM and compared the film morphologies before and after the DIW processing. Figure 2 shows SEM surface images of untreated and DIW-treated Al_2O_3 for both e-beam and IBS deposited films.

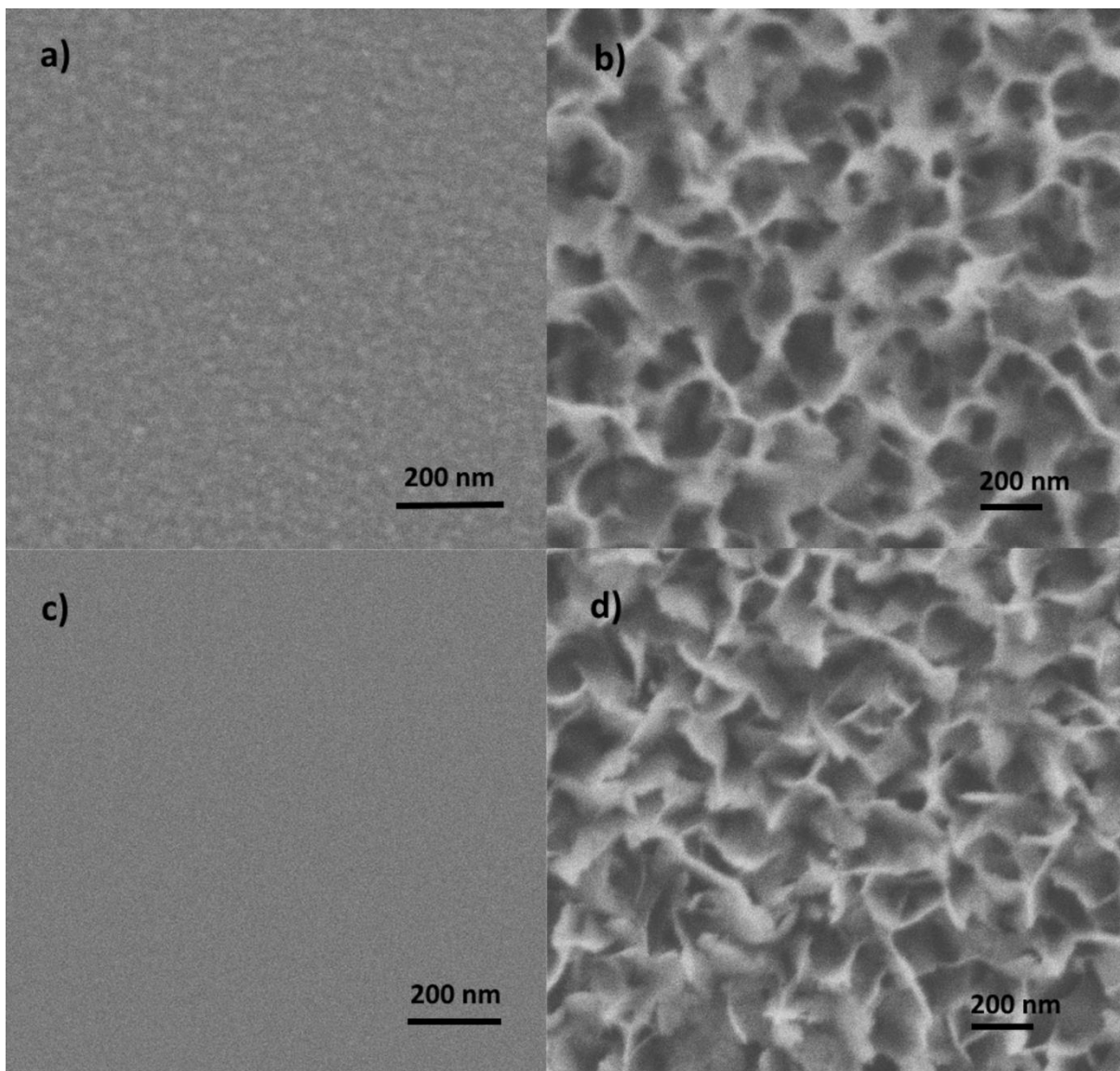


Fig. 2. SEM surface images of e-beam evaporated Al_2O_3 before (a) and after (b) DIW treatment and IBS deposited Al_2O_3 before (c) and after (d) DIW treatment.

From the SEM images we can see that both Al_2O_3 layers, independent of the deposition method, are relatively smooth prior to DIW immersion and after the treatment they form a porous, almost

flower-like, structure. In the case of ALD grown Al_2O_3 , it is hypothesized by Correa *et al.*³⁴ that the structural changes are due to the amorphous alumina hydrolyzing into aluminum hydroxides, namely $\beta\text{-Al}(\text{OH})_3$ (bayerite) and $\alpha\text{-Al}(\text{OH})_3$ (gibbsite)^{35,36}. According to their studies surface roughening and thickness change of the DIW treated samples matches to those of gibbsite and bayerite^{37,38}. To confirm the possible crystallinity of the Al_2O_3 films, the IBS Al_2O_3 samples were measured with XRD before and after DIW treatment. The XRD scans revealed no crystalline orientation, strongly indicating that both the as deposited and DIW treated films are of amorphous nature. This hydrolysis of amorphous alumina causing the morphology changes is examined in more detail by Dokmai *et al.*¹⁰.

To get a better sense of the height and roughness distribution of our samples, we used AFM scanning to measure the surface morphology, as shown in Figure 3.

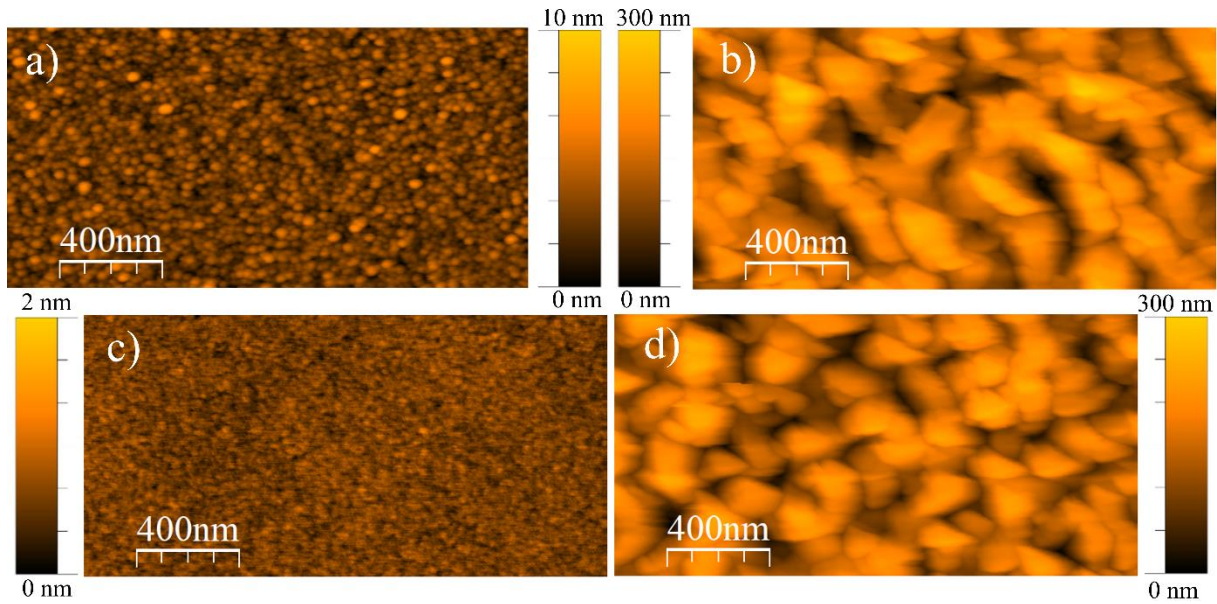


Fig. 3. Surface topography of *e*-beam evaporated Al_2O_3 before (a) and after (b) DIW treatment and IBS deposited Al_2O_3 before (c) and after (d) DIW treatment measured with AFM.

The AFM surface scans reveal a small difference in the height distribution of the pores of DIW treated samples in between the *e*-beam and IBS deposited films. We assume this to be related to the difference of the film quality in the as-deposited films, as the *e*-beam Al_2O_3 is slightly porous to begin with, whereas the IBS films are dense. Table 2 lists the numerical values for the surface

roughness and feature height and gives a nominal height difference of roughly 30 nm between the e-beam and IBS deposited Al_2O_3 after the DIW processing.

Table 2 *Surface roughness of the Al_2O_3 films before and after DIW treatment measured by AFM.*

	E-Beam		IBS	
	Untreated	DIW	Untreated	DIW
R_{rms} [nm]	0.86	41.09	0.13	42.10
R_{ave} [nm]	0.68	33.01	0.10	34.54
Average height [nm]	2.69	161.83	0.68	135.20
Max height [nm]	7.55	303.35	1.36	257.99

To verify the accuracy of the height distribution measured by AFM, we used SEM for cross-sectional imaging of the DIW treated IBS alumina. Figure 4 shows the corresponding heights of several alumina peaks.

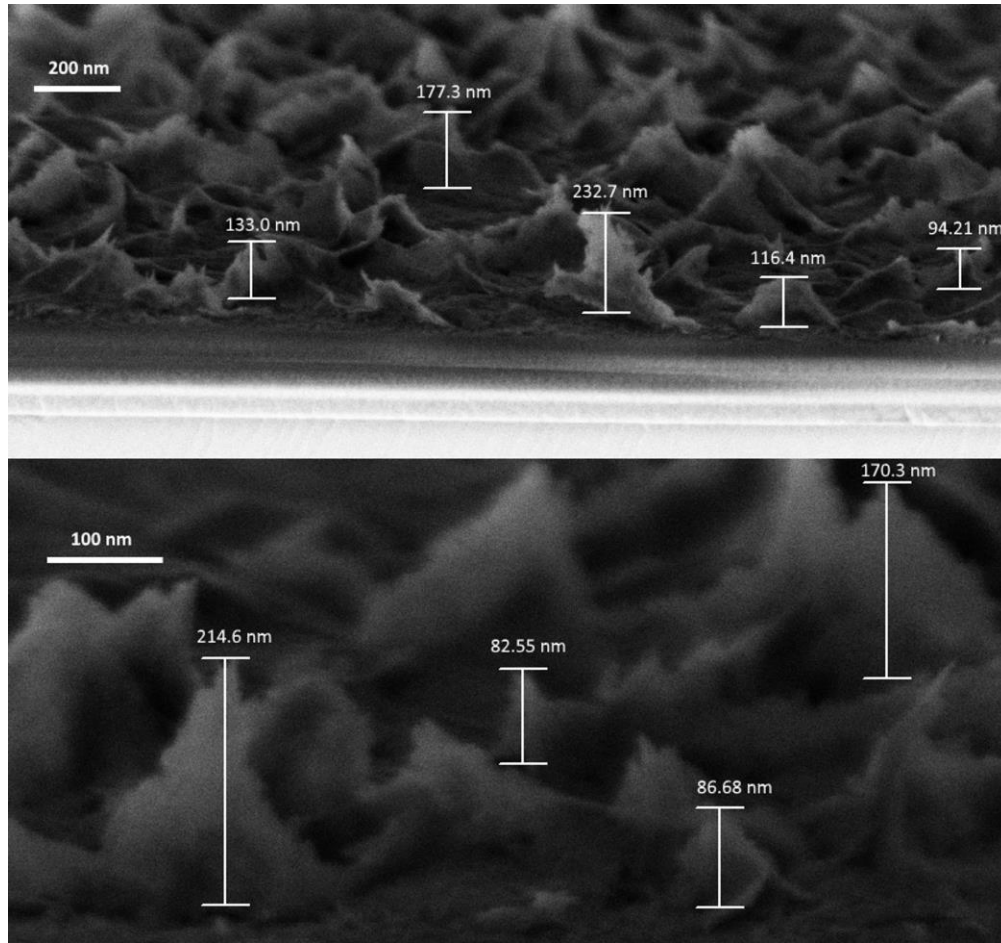


Fig. 4. Cross-sectional SEM images of DIW treated IBS Al_2O_3 with measured heights for chosen sampling of the peaks.

As already seen in Figure 2, Figure 4 shows the irregular morphology of the DIW treated Al_2O_3 and that the peak heights vary over 100 nm in length. The numerical data is well in line with the AFM measurements shown in Table 2.

Mechanical stability is an important issue for anti-reflection coatings in general and especially for porous coating types. However, we see that the mechanical durability is more connected to the environmental stability of the coating applications and not within the scope of this particular manuscript. Traditional Scotch tape test showed no signs of mechanical cracking or off-peeling of the coating under inspection of optical microscope, thus proving the mechanical stability sufficient for intended applications. In addition to the mechanical stability, the coating should remain clean enough to still function as an ARC. Any accumulating dust or moist on the nanostructured surface will likely reduce the transmission of the ARC and increase total losses. This can be solved by

very recently published fluoropolymerization process that makes the nanostructured alumina superhydrophobic³⁹. Our specific aim is utilization of this ARC on the III-V multi-junction solar cell architectures, where for example the space solar cells are encapsulated with cover glass/plastic⁴⁰ and concentrated photovoltaics behind the concentration optics⁴¹. Therefore, the suggested coating could be taken in use as is.

To test and see how the IBS and e-beam deposited porous alumina can be utilized for ARCs, we deposited a single layer of Al₂O₃ on fused silica (FS) substrates with post-deposition DIW treatment and measured the spectral performance of these filters. The measured transmittances are shown in Figure 5.

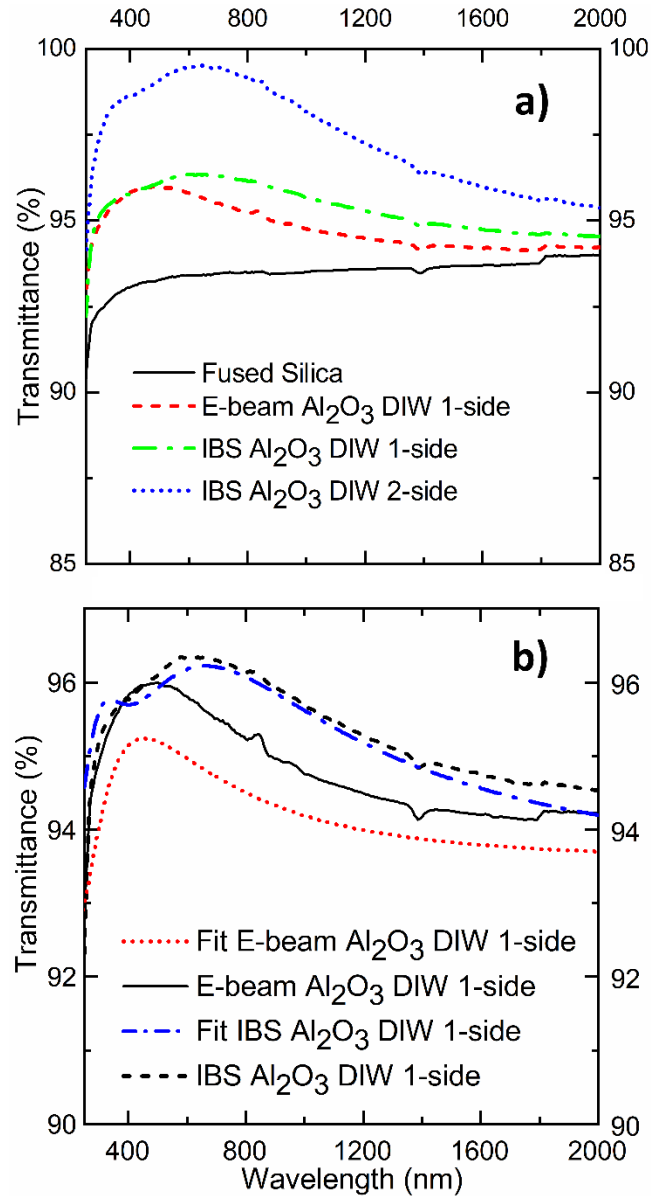


Fig. 5. a) The transmission spectra for samples coated with porous Al₂O₃ films with the transmittance of a bare fused silica substrate. b) Rugate filter numerical fittings compared to the measured transmittance of the DIW treated alumina structures.

For the one side coated DIW treated Al₂O₃ filters, the transmission is on average almost 95 % for both e-beam and IBS materials. The peak transmission wavelength of the filters differs slightly, pointing towards smaller feature size for e-beam deposited porous alumina than for the IBS deposited alumina. Based on the SEM and AFM comparison it would mean that the e-beam Al₂O₃ forms slightly narrower and taller build-ups than the IBS alumina. This also slightly reduces its

functionality as a graded index layer when compared to the IBS Al_2O_3 , as can be seen in the difference of the transmission curves between 1-side coated filters. To neglect the effect of substrate backside reflectance, we also tested two side IBS porous alumina coated FS, which reached an impressive 99.5 % peak transmittance at $\lambda = 600$ nm and overall transmittance over 95.5 % spanning the wide spectral region of 300-2000 nm.

To be able to effectively design coatings for new applications utilizing porous alumina films, it would be beneficial to simulate the effects of the films when combined with other materials before the actual deposition. For this purpose, we used the rugate filter approximation and matched its performance to the measured reflectance of TiO_2 /porous Al_2O_3 structures on silicon. To determine the applicability of the fit we used the alumina part of the fitting for comparison to the transmission measurements on FS as shown in Figure 5. b). For IBS deposited Al_2O_3 the fit works really well and only minor differences can be seen in the near ultraviolet and infrared parts of the spectrum. For e-beam deposited Al_2O_3 the fit is not nearly as good, as there is almost constant 1 % difference between the simulated and measured transmission of the film. However, even the e-beam simulation shows accurately the position of the peak transmission and the overall trend of the spectrum, which would make it useful for preliminary estimation of design functionalities.

As such, the used Si and FS substrates are a good starting point for material characterization, but as a part of an ARC on a real functional III–V solar cell (SC) the coatings might behave differently. Complex layer structure of the SC is also more challenging to simulate accurately for the preliminary optical designing of the ARC compared to a bare substrate. As the differences in functionality between e-beam and IBS deposited DIW treated alumina slightly favor the IBS deposited film, further ARC tests were done with IBS materials. The quality difference shown in this work is more related to the system specific limitations at our site than to the deposition methods itself, so no further comparison was made. To test out our nanoporous ARC structure and the accuracy of the used rugate model, we fabricated the DIW treated $\text{TiO}_2/\text{Al}_2\text{O}_3$ ARC by IBS on top of GaInP single-junction solar cell and simulated the entire structure to see the effectiveness of the model. GaInP SC is typically applied as the topmost junction in MJSC devices^{42,43} and is thus a reasonable choice for ARC characterization sample. The comparison between simulation and spectrophotometer measurements is shown in Figure 6. a).

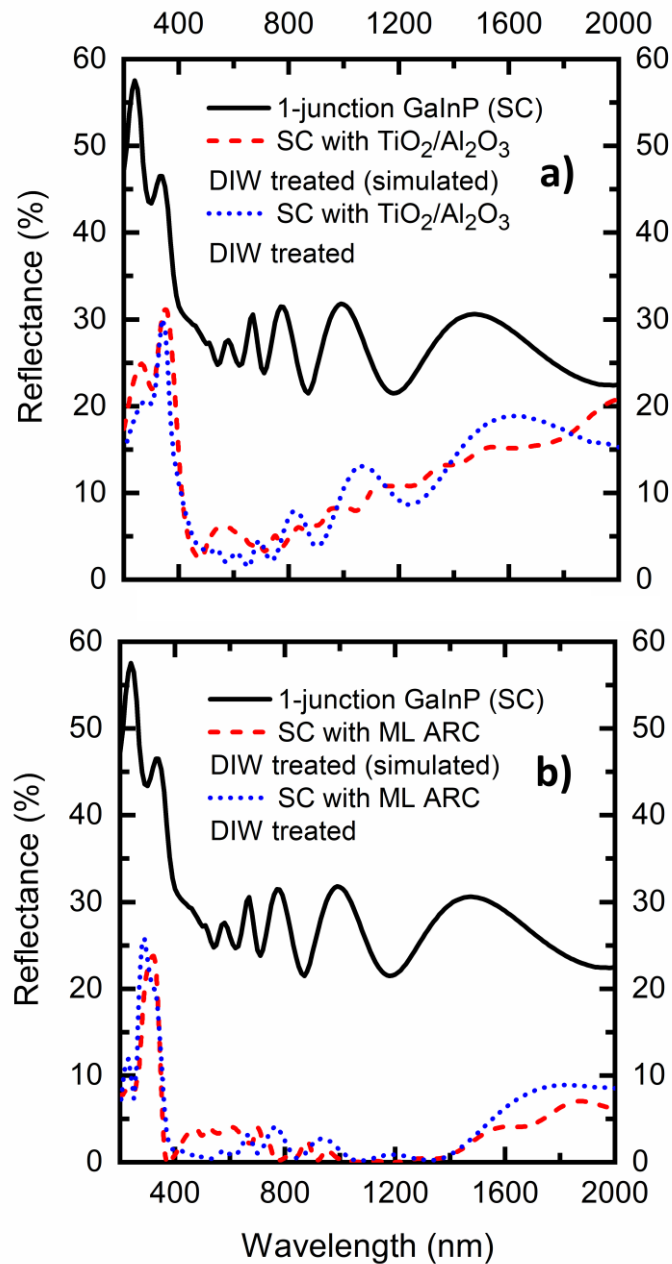


Fig. 6. Real and simulated reflectance of GaInP single-junction SC with DIW treated TiO₂/Al₂O₃ ARC in a) and with an advanced multilayer ARC structure with the nanoporous Al₂O₃ in b).

As Figure 6 shows, the simulated performance matches well to the actual measured reflectance of the coated GaInP solar cell and therefore the model is able to provide preliminary estimations of different ARC structures with the nanoporous Al₂O₃ top layer. The actual performance of the TiO₂/nanostructured Al₂O₃ ARC is not yet suitable to claim broadband operation nor does it reach

near 0 % reflectance at any point, so the design needs to be improved. To that end, we simulated and fabricated a ML ARC on top of the GaInP SC that combined all the tested IBS materials from Table 1. The reflectance of the ML ARC is plotted in the Figure 6 b). The ML ARC provides average reflectance of 3.28 % over a broadband spectral range from 400 to 2000 nm, which is especially beneficial for multijunction SC requiring such broadband operation. Regional average reflectance from 400 nm to 1000 nm is 1.65 % and from 1000 nm to 1500 nm the coating results in very impressive 0.86 % average reflectance. When comparing to the average reflectance of 2.7 % of a moth-eye patterned ARC⁴⁴, in the spectral range of 450 – 1650 nm, our approach provides almost 1 % lower average reflectance of 1.83 %. For multijunction solar cells the starting point for simulation and design is nominally different, but with the rugate filter approximation we can now have close estimations about the spectral performance for ARCs employing nanostructured Al₂O₃.

4. Conclusions

DIW based corrosion process for Al₂O₃ thin films was used to fabricate nanoporous optical coatings. The process does not alter the common hard coating oxides (SiO₂, TiO₂, Ta₂O₅) typically used in multilayer ARCs, which enables using the porous Al₂O₃ as a graded index layer on top of a multilayer ARC made of these oxides. The study showed that the post-deposition DIW treatment is compatible with both IBS and e-beam deposition methods, thus being applicable for a wide range of Al₂O₃ based ARCs. The optical effect of the topmost layer of the porous alumina can be simulated using a fitted rugate filter design, which then can be used to estimate the functionality of multilayer structures with TMM calculations. The performance of the nanoporous Al₂O₃ based ARCs was tested by fabricating such films on top of GaInP single-junction solar cells. The simulation model based on TMM rugate approach was also validated by fitting simulation and experimental results. The ML ARC exhibited a low average reflectance of ~3.3 % over a very broadband spectrum from 400 nm to 2000 nm, which is especially important in photovoltaic applications, where for example cover glasses, concentration lenses and other imperfect coated surfaces cause reflection losses.

The DIW corrosion based process for ML ARC with nanostructured Al₂O₃ is practical and can be easily implemented in efficient designs of ML coatings, we deem this development particular appealing for large scale exploitation in the next-generation SCs.

Acknowledgements

This work made use of Tampere Microscopy Center facilities at Tampere University. The authors acknowledge financial support provided by the European Research Council (ERC AdG AMETIST, #695116); the work is also part of the Academy of Finland PREIN flagship project (Grant No. 320165).

References

- ¹ D. Ristau and T. Gross, *Adv. Opt. Thin Film. II* **5963**, 596313 (2005).
- ² J. Gottmann and E.W. Kreutz, *Surf. Coatings Technol.* **116–119**, 1189 (1999).
- ³ R. Watanabe, M. Kawashima, and Y. Saito, *Thin Solid Films* **590**, 98 (2015).
- ⁴ K. Horiuchi, K. Nakada, S. Uchino, S. Hashii, A. Hashimoto, N. Aoki, Y. Ochiai, and M. Shimizu, *Appl. Phys. Lett.* **81**, 1911 (2002).
- ⁵ L.H. Kim, K. Kim, S. Park, Y.J. Jeong, H. Kim, D.S. Chung, S.H. Kim, and C.E. Park, *ACS Appl. Mater. Interfaces* **6**, 6731 (2014).
- ⁶ T.S. Eriksson, A. Hjortsberg, G.A. Niklasson, and C.G. Granqvist, *Appl. Opt.* **20**, 2742 (1981).
- ⁷ J. Kischkat, S. Peters, B. Gruska, M. Semtsiv, M. Chashnikova, M. Klinkmüller, O. Fedosenko, S. Machulik, A. Aleksandrova, G. Monastyrskyi, Y. Flores, and W. Ted Masselink, *Appl. Opt.* **51**, 6789 (2012).
- ⁸ C.E. Chryssou and C.W. Pitt, *Appl. Phys. A Mater. Sci. Process.* **65**, 469 (1997).
- ⁹ A.I. Abdulagatov, Y. Yan, J.R. Cooper, Y. Zhang, Z.M. Gibbs, A.S. Cavanagh, R.G. Yang, Y.C. Lee, and S.M. George, *ACS Appl. Mater. Interfaces* **3**, 4593 (2011).
- ¹⁰ V. Dokmai, R. Methaapanon, and V. Pavarajarn, *Appl. Surf. Sci.* **499**, 143906 (2020).

- ¹¹ G. Este and W.D. Westwood, *J. Vac. Sci. Technol. A Vacuum, Surfaces, Film.* **2**, 1238 (1984).
- ¹² C.P. Huang and W. Stumm, *J. Colloid Interface Sci.* **43**, 409 (1973).
- ¹³ J.S.L. Leach and P. Neufeld, *Corros. Sci.* **9**, 413 (1969).
- ¹⁴ G. Patermarakis, P. Lenas, C. Karavassilis, and G. Papayiannis, *Electrochim. Acta* **36**, 709 (1991).
- ¹⁵ K. Tadanaga, N. Katata, and T. Minami, *J. Am. Ceram. Soc.* **80**, 3213 (2005).
- ¹⁶ Z. Liu, J. Deng, and D. Li, *Anal. Chim. Acta* **407**, 87 (2000).
- ¹⁷ Q. Chen, G. Hubbard, P.A. Shields, C. Liu, D.W.E. Allsopp, W.N. Wang, and S. Abbott, *Appl. Phys. Lett.* **94**, 263118 (2009).
- ¹⁸ J. Tommila, A. Aho, A. Tukiainen, V. Polojärvi, J. Salmi, T. Niemi, and M. Guina, *Prog. Photovoltaics Res. Appl.* **21**, 1158 (2013).
- ¹⁹ K.-S. Han, J.-H. Shin, W.-Y. Yoon, and H. Lee, *Sol. Energy Mater. Sol. Cells* **95**, 288 (2011).
- ²⁰ C.-H. Sun, B.J. Ho, B. Jiang, and P. Jiang, *Opt. Lett.* **33**, 2224 (2008).
- ²¹ W.-L. Min, A.P. Betancourt, P. Jiang, and B. Jiang, *Appl. Phys. Lett.* **92**, 141109 (2008).
- ²² H.-L. Chen, A. Cattoni, R. De Lépinau, A.W. Walker, O. Höhn, D. Lackner, G. Siefer, M. Faustini, N. Vandamme, J. Goffard, B. Behaghel, C. Dupuis, N. Bardou, F. Dimroth, and S. Collin, *Nat. Energy* **4**, 761 (2019).
- ²³ E.E. Perl, W.E. McMahon, J.E. Bowers, and D.J. Friedman, *Opt. Express* **22**, A1243 (2014).
- ²⁴ M. Keshavarz Hedayati and M. Elbahri, *Materials (Basel)*. **9**, 497 (2016).

- ²⁵ C. Kauppinen, K. Isakov, and M. Sopanen, *ACS Appl. Mater. Interfaces* **9**, 15038 (2017).
- ²⁶ D.J. Friedman, *Curr. Opin. Solid State Mater. Sci.* **14**, 131 (2010).
- ²⁷ W. Weinstein, *J. Opt. Soc. Am.* **37**, 576 (1947).
- ²⁸ F. Abelès, *Ann. Phys. (Paris)*. **12**, 596 (1950).
- ²⁹ A. Herpin, *Comptes Rendus* 182 (1947).
- ³⁰ M. Morita, T. Ohmi, E. Hasegawa, M. Kawakami, and M. Ohwada, *J. Appl. Phys.* **68**, 1272 (1990).
- ³¹ I. Horcas, R. Fernández, J.M. Gómez-Rodríguez, J. Colchero, J. Gómez-Herrero, and A.M. Baro, *Rev. Sci. Instrum.* **78**, 1 (2007).
- ³² D.E. Aspnes, *Thin Solid Films* **89**, 249 (1982).
- ³³ V.A. Markel, *J. Opt. Soc. Am. A* **33**, 1244 (2016).
- ³⁴ G.C. Correa, B. Bao, and N.C. Strandwitz, *ACS Appl. Mater. Interfaces* **7**, 14816 (2015).
- ³⁵ K. Wefers and C. Misra, *Alcoa Tech. Pap.* **19**, 1 (1987).
- ³⁶ G. Lefèvre, M. Duc, P. Lepeut, R. Caplain, and M. Fédoroff, *Langmuir* **18**, 7530 (2002).
- ³⁷ R. Schoen and C.E. Roberson, *Am. Mineral.* **55**, 43 (1970).
- ³⁸ M.L.P. Antunes, H.D.S. Santos, and P.D.S. Santos, *Mater. Chem. Phys.* **76**, 243 (2002).
- ³⁹ K. Isakov, C. Kauppinen, S. Franssila, and H. Lipsanen, *ACS Appl. Mater. Interfaces* **12**, 49957 (2020).
- ⁴⁰ R. King, C. Fetzer, D. Law, K. Edmondson, H. Yoon, G. Kinsey, D. Krut, J. Ermer, P. Hebert,

B. Cavicchi, and N. Karam, in *2006 IEEE 4th World Conf. Photovolt. Energy Conf.* (IEEE, 2006), pp. 1757–1762.

⁴¹ S. Vaid, M. Kats, G. Hering, P. Blumenfeld, D. Buie, J. Nagyvary, J. Foresi, and P.A. Zawadzki, (2009).

⁴² R.R. King, D.C. Law, K.M. Edmondson, C.M. Fetzer, G.S. Kinsey, H. Yoon, R.A. Sherif, and N.H. Karam, *Appl. Phys. Lett.* **90**, (2007).

⁴³ M. Wiemer, V. Sabnis, and H. Yuen, in *High Low Conc. Syst. Sol. Electr. Appl. VI*, edited by K. VanSant and R.A. Sherif (2011), p. 810804.

⁴⁴ J. Tommila, A. Aho, A. Tukiainen, V. Polojärvi, J. Salmi, T. Niemi, and M. Guina, *Prog. Photovoltaics Res. Appl.* **21**, 1158 (2013).

Appendix A.

Deposition parameters

IBS	Al ₂ O ₃	SiO ₂	TiO ₂	Ta ₂ O ₅
	Al	Si	Ti	Ta
Target	purity of 99.999 %	purity of 99.999 %	purity of 99.8 %	purity of 99.95 %
Sputtering gas	Ar:O ₂ (8:5 sccm)	Ar:O ₂ (8:5 sccm)	Ar:O ₂ (8:5 sccm)	Ar:O ₂ (8:5 sccm)
Process gas [O ₂] flow [sccm]	80	90	80	80
Deposition pressure [mbar]	4.5 × 10 ⁻⁴	4.5 × 10 ⁻⁴	4.5 × 10 ⁻⁴	4.5 × 10 ⁻⁴
RF power [W]	102	115	150	145
Sputtering Voltage [kV]	1.26	1.50	2.00	2.00

E-beam	Al ₂ O ₃	SiO ₂	TiO ₂	Ta ₂ O ₅
	Al ₂ O ₃	SiO ₂	TiO ₂	Ta ₂ O ₅
Target	purity of 99.999 %	purity of 99.99 %	purity of 99.9 %	purity of 99.95 %
Additional O ₂	no	no	yes	yes
Deposition pressure [mbar]	6 × 10 ⁻⁵	5 × 10 ⁻⁵	1.9 × 10 ⁻⁴	1.5 × 10 ⁻⁴
Substrate temperature [°C]	150	100	100	100

Appendix B.

Rugate models for DIW treated Al₂O₃

Layer Nbr	E-beam	Start Design	Fitted	IBS	Start Design	Fitted
	Refractive Index	Physical Thickness [nm]	Physical Thickness [nm]	Refractive Index	Physical Thickness [nm]	Physical Thickness [nm]
100	1.000	1.58	0.56	1.000	1.58	3.63
99	1.006	1.57	0.67	1.007	1.57	1.03
98	1.012	1.56	0.17	1.014	1.56	2.85
97	1.018	1.56	0.11	1.020	1.55	1.95
96	1.024	1.55	0.00	1.027	1.54	5.36

95	1.030	1.54	2.97	1.034	1.53	2.22
94	1.036	1.53	0.01	1.041	1.52	5.10
93	1.042	1.52	3.57	1.047	1.51	13.07
92	1.048	1.51	1.77	1.054	1.50	10.95
91	1.053	1.50	0.05	1.061	1.49	11.96
90	1.059	1.49	0.01	1.068	1.48	20.41
89	1.065	1.49	0.59	1.074	1.47	5.93
88	1.071	1.48	5.28	1.081	1.47	21.55
87	1.077	1.47	32.32	1.088	1.46	1.87
86	1.083	1.46	10.37	1.095	1.45	0.73
85	1.089	1.45	7.65	1.101	1.44	0.48
84	1.095	1.45	19.29	1.108	1.43	0.35
83	1.101	1.44	4.54	1.115	1.42	1.63
82	1.107	1.43	0.36	1.122	1.41	2.85
81	1.113	1.42	7.13	1.128	1.40	3.08
80	1.119	1.42	4.26	1.135	1.40	3.42
79	1.125	1.41	1.95	1.142	1.39	0.88
78	1.131	1.40	0.40	1.149	1.38	0.11
77	1.137	1.39	0.40	1.155	1.37	3.31
76	1.143	1.39	2.91	1.162	1.36	5.36
75	1.149	1.38	0.26	1.169	1.36	4.95
74	1.155	1.37	0.02	1.176	1.35	18.71
73	1.160	1.37	0.06	1.182	1.34	21.03
72	1.166	1.36	0.01	1.189	1.33	14.06
71	1.172	1.35	0.56	1.196	1.33	0.34
70	1.178	1.35	0.01	1.203	1.32	1.44
69	1.184	1.34	0.01	1.209	1.31	1.87
68	1.190	1.33	0.15	1.216	1.30	8.00
67	1.196	1.33	0.18	1.223	1.30	3.28
66	1.202	1.32	0.06	1.230	1.29	2.11
65	1.208	1.31	0.30	1.236	1.28	1.29
64	1.214	1.31	0.00	1.243	1.28	0.61
63	1.220	1.30	0.02	1.250	1.27	0.88
62	1.226	1.29	0.14	1.257	1.26	1.40
61	1.232	1.29	0.09	1.263	1.26	0.73
60	1.238	1.28	0.04	1.270	1.25	0.74
59	1.244	1.28	0.03	1.277	1.24	0.44
58	1.250	1.27	0.01	1.284	1.24	0.55
57	1.256	1.26	0.01	1.290	1.23	0.40
56	1.262	1.26	0.00	1.297	1.22	0.42
55	1.267	1.25	0.02	1.304	1.22	0.36
54	1.273	1.25	0.59	1.311	1.21	0.71
53	1.279	1.24	0.45	1.317	1.21	0.88

52	1.285	1.23	0.50	1.324	1.20	0.79
51	1.291	1.23	0.01	1.331	1.19	0.48
50	1.297	1.22	0.18	1.338	1.19	1.02
49	1.303	1.22	0.30	1.344	1.18	0.90
48	1.309	1.21	0.01	1.351	1.18	0.64
47	1.315	1.21	0.16	1.358	1.17	0.06
46	1.321	1.20	0.29	1.365	1.16	0.03
45	1.327	1.20	0.31	1.371	1.16	0.06
44	1.333	1.19	0.02	1.378	1.15	0.01
43	1.339	1.19	0.03	1.385	1.15	0.01
42	1.345	1.18	0.08	1.392	1.14	0.07
41	1.351	1.18	0.46	1.398	1.14	0.24
40	1.357	1.17	0.17	1.405	1.13	0.10
39	1.363	1.17	0.00	1.412	1.13	0.19
38	1.369	1.16	0.63	1.419	1.12	0.21
37	1.374	1.16	0.75	1.426	1.11	0.02
36	1.380	1.15	1.07	1.432	1.11	0.09
35	1.386	1.15	0.92	1.439	1.10	0.15
34	1.392	1.14	0.15	1.446	1.10	0.07
33	1.398	1.14	0.02	1.453	1.09	0.26
32	1.404	1.13	0.08	1.459	1.09	0.00
31	1.410	1.13	0.08	1.466	1.08	0.07
30	1.416	1.12	0.20	1.473	1.08	0.05
29	1.422	1.12	0.23	1.480	1.07	0.02
28	1.428	1.11	0.03	1.486	1.07	0.10
27	1.434	1.11	0.01	1.493	1.06	0.01
26	1.440	1.10	0.13	1.500	1.06	0.01
25	1.446	1.10	0.17	1.507	1.06	0.02
24	1.452	1.09	0.15	1.513	1.05	0.05
23	1.458	1.09	0.13	1.520	1.05	0.02
22	1.464	1.09	0.07	1.527	1.04	0.03
21	1.470	1.08	0.11	1.534	1.04	0.09
20	1.475	1.08	0.11	1.540	1.03	0.01
19	1.481	1.07	0.11	1.547	1.03	0.14
18	1.487	1.07	0.01	1.554	1.02	0.01
17	1.493	1.06	0.05	1.561	1.02	0.06
16	1.499	1.06	0.30	1.567	1.01	0.03
15	1.505	1.06	0.11	1.574	1.01	0.00
14	1.511	1.05	0.25	1.581	1.01	0.01
13	1.517	1.05	0.00	1.588	1.00	0.01
12	1.523	1.04	0.00	1.594	1.00	0.40
11	1.529	1.04	0.00	1.601	0.99	0.02
10	1.535	1.04	0.05	1.608	0.99	0.02

9	1.541	1.03	0.08	1.615	0.99	0.00
8	1.547	1.03	0.53	1.621	0.98	0.00
7	1.553	1.02	0.96	1.628	0.98	0.08
6	1.559	1.02	0.28	1.635	0.97	0.10
5	1.565	1.02	1.16	1.642	0.97	0.30
4	1.571	1.01	0.01	1.648	0.97	0.15
3	1.577	1.01	0.47	1.655	0.96	0.07
2	1.582	1.01	0.85	1.662	0.96	0.26
1	1.588	1.00	2.09	1.669	0.95	0.34

PUBLICATION

4

Optical Performance Assessment of Nanostructured Alumina Multilayer Antireflective Coatings used in III–V Multijunction Solar Cells

J. Reuna, A. Hietalahti, A. Aho, R. Isoaho, T. Aho, M. Vuorinen, A. Tukiainen, E. Anttola and M. Guina

ACS Applied Energy Materials, vol. 5, no. 5, p. 5804-5810, April 2022

[https://doi.org/ 10.1021/acsam.2c00133](https://doi.org/10.1021/acsam.2c00133)

Publication reprinted with the permission of the copyright holders.

Optical Performance Assessment of Nanostructured Alumina Multilayer Antireflective Coatings Used in III–V Multijunction Solar Cells

Jarno Reuna,* Arttu Hietalahti, Arto Aho, Riku Isoaho, Timo Aho, Marianna Vuorinen, Antti Tukiainen, Elina Anttola, and Mircea Guina



Cite This: <https://doi.org/10.1021/acsaem.2c00133>



Read Online

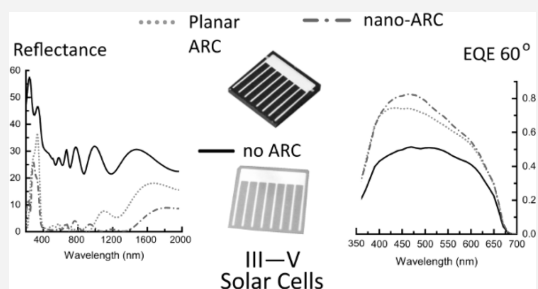
ACCESS |

Metrics & More

Article Recommendations

ABSTRACT: The optical performance of a multilayer antireflective coating incorporating lithography-free nanostructured alumina is assessed. To this end, the performance of single-junction GaInP solar cells and four-junction GaInP/GaAs/GaInNAsSb/GaInNAsSb multijunction solar cells incorporating the nanostructured alumina is compared against the performance of similar solar cells using conventional double-layer antireflective coating. External quantum efficiency measurements for GaInP solar cells with the nanostructured coating demonstrate angle-independent operation, showing only a marginal difference at 60° incident angle. The average reflectance of the nanostructured antireflective coating is ~3 percentage points smaller than the reflectance of the double-layer antireflective coating within the operation bandwidth of the GaInP solar cell (280–710 nm), which is equivalent of ~0.2 mA/cm² higher current density at AM1.5D (1000 W/m²). When used in conjunction with the four-junction solar cell, the nanostructured coating provides ~0.8 percentage points lower average reflectance over the operation bandwidth from 280 to 1380 nm. However, it is noted that only the reflectance of the bottom GaInNAsSb junction is improved in comparison to the planar coating. In this respect, since in such solar cells the bottom junction typically is limiting the operation, the nanostructured coating would enable increasing the current density ~0.6 mA/cm² in comparison to the standard two-layer coating. The light-biased current–voltage measurements show that the fabrication process for the nanostructured coating does not induce notable recombination or loss mechanisms compared to the established deposition methods. Angle-dependent external quantum efficiency measurements incline that the nanostructured coating excels in oblique angles, and due to low reflectance at a 1000–1800 nm wavelength range, it is very promising for next-generation broadband multijunction solar cells with four or more junctions.

KEYWORDS: antireflective coating, nanostructuring, III–V multijunction solar cell, omnidirectional, broadband



1. INTRODUCTION

High efficiency III–V multijunction solar cells (MJSC) offer the most advanced photovoltaic technology to date, with the highest confirmed conversion efficiency reaching 47.1%^{1,2} and theoretical efficiency surpassing 50%.^{3–5} Such MJSCs utilize a very broadband spectrum of the solar irradiation, and significant losses can come from the reflected light from the surface of the cell. Conventional double-layer antireflective coatings (ARC) have been frequently used in MJSC applications,^{6–8} but when exceeding three junctions, the current matching starts to require broader reduction of reflectance.^{6,9} This is especially true for solar cell structures with a germanium bottom junction, where the usable spectral bandwidth extends up to 1800 nm.^{10–12} In general, different kinds of nanostructured ARCs have been applied in order to

obtain low reflectance in a broad spectral band,^{13–20} but they typically come with their drawbacks. With a patterned semiconductor window layer, there are additional losses in the ultraviolet region due to the need for thick window layers,^{15–17} direct patterning of the solar cell structure can cause increased recombination losses,¹⁸ and with patterned dielectric structure, the refractive index contrast between the high index semiconductor material and the low index ARC is

Received: January 12, 2022

Accepted: April 12, 2022

too large for efficient reduction of reflectance.^{13,14} Multilayer dielectric coatings combined with patterning^{9,19,20} have so far been an effective but laborious solution due to multistep fabrication processes.

As an alternative, we proposed recently²¹ a simple, nontoxic, low-cost nanostructured multilayer ARC that is based on postdeposition treatment of planar amorphous alumina coatings with heated deionized water.^{22,23} An advantage of this approach compared to similar kind of hybrid broadband ARC^{19,20} is the reduced number of fabrication steps, as it does not need lithography and surface etching for patterning. The properties of the nanopattern can be controlled via film thickness and treatment time,²⁴ and the hydrophobicity of the film can be increased with postprocess polymerization.²⁵

Here, we present a comparison between the performance of the novel nanostructured ARC and conventional planar ARC when applied to single-junction (1J) and four-junction (4J) III–V solar cells (SC). The 1J structure is used for assessing the angle-dependent characteristics of the nanostructured coating, as with MJSC such characterization is challenging to do correctly and requires more developed instrumentation.^{26,27} The actual broadband operation and suitability for MJSCs are then verified with the 4J SCs.

2. EXPERIMENTAL SECTION

The lattice-matched III–V SC structures, namely, GaInP 1J and GaInP/GaAs/GaInNAsSb/GaInNAsSb 4J, with band gap energies of 1.9 eV/1.4 eV/1.2 eV/0.9 eV, respectively, were grown by molecular beam epitaxy on p-GaAs substrates using a Veeco GEN20 MBE system. Specific structural details and the performance of the reference cells are provided elsewhere.⁷ The wafers were diced into 6 mm × 6 mm SCs with an active area of 0.25 cm². Both the Ni/Au (10/100 nm) front contact grid on the n-side and Ti/Au (50/100 nm) planar back contact on the p-side were deposited using an electron beam (e-beam) evaporator. Prior to ARC deposition, the contact GaAs layer was removed with NH₃/H₂O₂/H₂O etchant solution.

The conventional planar double-layer ARC was grown by an e-beam, and the multilayer film for the nanostructured ARC (nano-ARC) was deposited by ion beam sputtering (IBS) using a Navigator 700 sputtering system from Cutting Edge Coatings GmbH. The nanostructuring of the amorphous alumina layer was achieved by treating the coating with heated deionized water (DIW). The method for nanostructuring the alumina surface is described in detail in reference.²¹ The nominal structure of the nano-ARC and its cross-sectional scanning electron microscope image are shown in Figure 1. The planar double-layer coating had the nominal structure of 50 nm TiO₂/89 nm SiO₂. The planar ARC has originally been optimized for the GaInP/GaAs/GaInNAsSb triple-junction MJSC,²⁸ so that the top-junction (GaInP) would not be the current-limiting junction. It exhibits relatively broadband low reflectivity at 400–1000 nm and with the given materials represents a robust and realistic optimal double-layer ARC for these III–V MJSCs. This makes it a suitable comparison structure for the nano-ARC in question.

Scanning electron microscope (SEM) images were taken with a SIGMA FESEM operated with SmartSEM software, both products of Carl Zeiss NTS Ltd. The acceleration voltage was 1 kV, and the aperture size was 10 μm. The dielectric nature of the coating causes charging of the scanned area, which can cause image distortions. The imaged samples were tilted ~10° in attempts to avoid areal charge accumulation.

A PerkinElmer Lambda 1050 UV/vis/NIR spectrophotometer equipped with either an integrating sphere or a Universal Reflectance Accessory (URA) module was used for the reflectance measurements. The URA measures reflectance at 8° angle of incidence and the integrating sphere at normal incidence. The URA module can measure only specular reflectance, whereas the integrating sphere

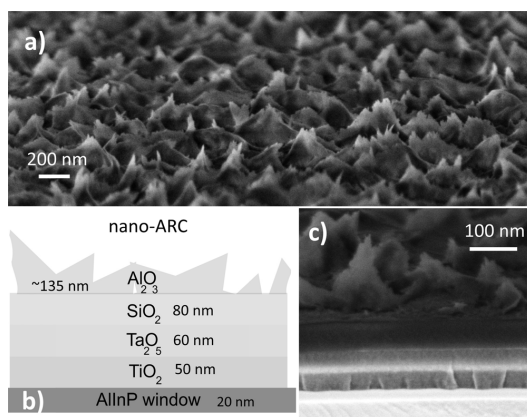


Figure 1. (a) Scanning electron microscope surface scan of the nano-ARC, (b) schematic illustration of its structure, and (c) cross-sectional scanning electron micrograph of the nanostructured coating.

nominally measures also all the scattered light. No notable difference in sample performance was observed between the modules, indicating negligible diffuse scattering from the nanostructure. For the spectrum-weighted average, the values were calculated as follows:

$$R_{\text{ave}} = \frac{\sum_i \Phi_i(\lambda) R_i(\lambda)}{\sum_i \Phi_i(\lambda)} \quad (1)$$

in which Φ_i is the incident photon flux and R_i is the measured reflectance at a given wavelength.

Light-biased current–voltage (LIV) characteristics of the SCs were measured with a 7 kW OAI Trisol solar simulator calibrated for AM1.5D (1000 W/m²) illumination. Evaluated properties include conversion efficiency η , open-circuit voltage V_{OC} , short-circuit current density J_{SC} , and fill factor FF. All the samples were measured at the same time, the measurements were repeated a number of times, and the average standard deviations for the quantities are 0.1 percentage points, 3 mV, 0.1 mA/cm², and 1 percentage points, respectively. In addition of the statistical uncertainties, the unideal spectrum of the used simulator lamp, which is known to be infrared-weighted, and temporal variations increase the error limits for drawing conclusions. The external quantum efficiency (EQE) measurements for the GaInP cells were performed with a monochromator-based measurement system, which was adjusted using a NIST (National Institute of Standards and Technology)-calibrated Si reference cell at room temperature (22 °C). An angle-selective stage (Thorlabs High-Precision Rotation Stage PR01/M) was used to accurately ($\pm 1^\circ$) align the incidence angle of the probe beam on the GaInP cells at variable angles from 0° to 45° and 60° to assess the oblique angle performance of the ARCs.

A python script based on May et al integration tools²⁹ was used to calculate the ideal and EQE-derived current densities of different subjunction bandwidths according to both AM0 (ASTM E-490) and AM1.5D (ASTM G-173-03) solar spectra.³⁰ In the calculations, the ARCs are assumed to be lossless ($T = 1 - R$) and the internal quantum efficiency (IQE) to be unity. The cases where IQE = 1 and EQE = 1 - R are labeled as ideal and represent the theoretical maximum when all the incident photons that are not reflected from the SC are absorbed and each generates a charge-carrier pair. This provides a comparable quantity representing the current-generation potential of different spectral bandwidths when assessing the differences of the ARCs. The most common applications of III–V multijunction SC materials are either in space or in terrestrial concentrator photovoltaics. AM0 spectra are the standard that is used for comparing space photovoltaic SCs used for instance in satellites. Similarly, AM1.5D is used for comparing the performance of III–V concentrator SC materials, as

only direct sunlight can be efficiently concentrated. Comparing both gives a realistic evaluation of the nano-ARC performance in the possible applications.

3. RESULTS AND DISCUSSION

The reflectance and LIV characteristics of the GaInP 1J cells with the nano-ARC and the planar double-layer ARC under AM1.5D (1000 W/m²) illumination are presented in Figure 2.

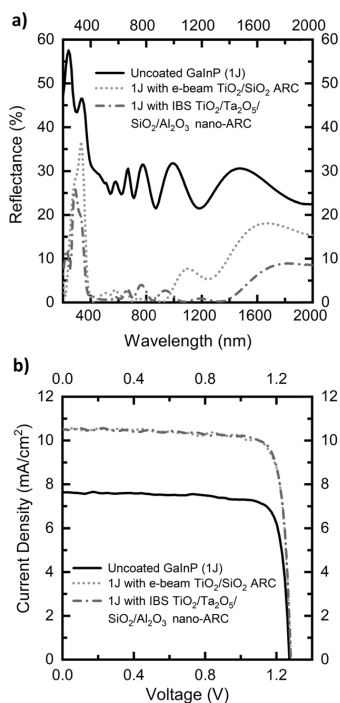


Figure 2. (a) URA-measured reflectance for uncoated GaInP 1J, with the conventional e-beam double-layer ARC and with the nano-ARC. (b) Measured LIV under AM1.5D (1000 W/m²) for the 1 J GaInP solar cells without a coating, with the e-beam double-layer ARC and with the nano-ARC.

Figure 2a clearly shows that the nano-ARC has lower reflectance over broader bandwidths than the double-layer ARC, as was expected. The spectrum-weighted average reflectance values (R_{AVE}) at the operative bandwidth of the GaInP SC are presented in Table 1. Based only on the

reflectance values, it is expected that the GaInP SC with the nano-ARC should have better LIV performance.

The modest performance of the GaInP SCs in terms of efficiency and current density is due to the fact that the SCs in question are designed to be current matched as a part of an MJSC and not to be standalone SCs, thus being thinner than conventional junctions. The reasoning and the effects of thinning are further discussed elsewhere.^{7,31} However, as a topmost junction in MJSC configuration, they suit very well as ARC reference samples when the coatings are evaluated against each other.

To see if nanostructuring has the expected^{20,32} angle-independent nature, the EQEs of the GaInP SC were measured at different angles of 0°, 45°, and 60°. The angle-dependent EQEs are shown in Figure 3, and the related calculational current densities under AM1.5D (1000 W/m²) are shown in inset tables for each subplot.

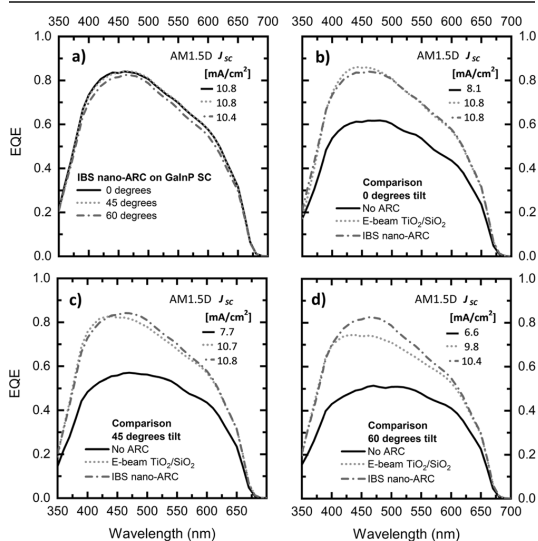


Figure 3. (a) Measured angle-dependent EQEs for the 1J GaInP solar cells coated with the nano-ARC at the angles of 0°, 45°, and 60°, demonstrating nearly unchanged performance as a function of the incidence angle. (b)–(d) Comparison of 1J GaInP solar cell EQEs without an ARC, with the e-beam ARC, and with the nano-ARC at the angles of 0°, 45°, and 60°, respectively. For each of the measured EQEs, the corresponding current density under the AM1.5D (1000 W/m²) spectrum has been calculated and is shown in the inset tables on the right upper corner of each subplot.

Table 1. Spectrum-Weighted R_{AVE} for the Coated GaInP 1J Solar Cells Presented at the Bandwidth of Operation Both with AM0 and AM1.5D Spectra, and the Measured LIV Characteristics under AM1.5D (1000 W/m²) Illumination, with Conversion Efficiency η , Open-Circuit Voltage V_{OC} , Short-Circuit Current Density J_{SC} , and Fill Factor FF for Bare SC, with Planar e-Beam ARC, and with Nano-ARC

		bandwidth (nm)	uncoated	e-beam TiO ₂ /SiO ₂	IBS TiO ₂ /Ta ₂ O ₅ /SiO ₂ /Al ₂ O ₃ nano-ARC
R_{AVE}	AM0	280–710	28.8%	3.6%	2.2%
	AM1.5D	280–710	27.8%	2.3%	1.5%
η (%)			8.4	11.1	11.4
V_{OC} (V)			1.3	1.3	1.3
J_{SC} (mA/cm ²)			8.0	10.9	10.8
FF [%]			81.7	79.2	82.6

At the normal incidence angle, the EQEs of the coated SCs are very similar, but near the peak wavelength (465 nm), the planar ARC performs slightly better (~ 0.02). At 45° , the difference between the two coatings favors the nano-ARC, as the planar ARC peak EQE drops by 0.04, whereas the nano-ARC EQE remains the same. The difference is even more evident at an angle of 60° , where the planar ARC peak EQE drops significantly by 0.12, but the nano-ARC EQE only drops by 0.01, demonstrating in practice the angle-independent operation. The numerical values for peak EQEs are shown in Table 2.

Table 2. Peak EQE Values at 465 nm for the GaInP Solar Cells with Different Coatings

angle of incidence	uncoated	e-Beam TiO ₂ /SiO ₂	IBS TiO ₂ /Ta ₂ O ₅ /SiO ₂ /Al ₂ O ₃ nano-ARC
0°	0.62	0.86	0.84
45°	0.57	0.82	0.84
60°	0.51	0.74	0.83

The drop in EQE corresponds to current density differences of 0.1 and 0.6 mA/cm² favoring the nano-ARC at the angles of 45° and 60° , respectively. Both the reflectance and EQE values of the nano-ARC indicate that it should perform almost identically to the planar ARC at a normal incidence angle for the GaInP SC, which is in line with the acquired LIV results. For longer wavelengths and oblique angle operation, the nano-ARC should function clearly better than the planar reference ARC.

Using the reflectance of the different coatings and a bandgap of 1.9 eV, the nominal current densities for the GaInP SC were calculated at AM0 and AM1.5D both in an ideal case ($I_{QE} = 1$; $EQE = 1 - R$) and with the measured EQE, as shown in Table 3.

The calculated values based on the measured EQE shown in Figure 3 and the LIV measurement results presented in Figure 2b and Table 1 are in close agreement; as for all cases, the calculated value and the measured value are within 0.1 mA/cm². The existing variations in results can be linked to differences between individual SCs used in the measurements, such as the active cell area that is affected both by the used shadow mask in the contact metal deposition and the dicing precision. Based on the spectral comparison in the ideal cases, both coatings perform within 1 mA/cm² of the theoretical maximum current density shown in the rightmost column of Table 3. At AM0, the nano-ARC should provide 0.4 mA/cm² higher current density than the planar ARC and similarly 0.2 mA/cm² higher current density at AM1.5D. Slight improvements are still possible, as the nano-ARC deviates from the ideal current density by ~ 0.2 mA/cm² at AM1.5D and ~ 0.5 mA/cm² at AM0. As the measured SCs are thinner than

standalone GaInP 1-junctions would optimally be, the transmission losses cause the main difference between the ideal current densities and the ones calculated with the real EQE. Part of the difference is due to recombination losses that are neglected in the ideal case.

The promising functionality on the 1J GaInP SC does not straightforwardly prove suitability for MJSCs as the current balancing, series resistance, and edge recombination scheme greatly differ between 1J and the MJSC. To this end, the ARCs were also deposited on GaInP/GaAs/GaInNAsSb/GaInNAsSb 4J. The reflectance of the MJSCs with the coatings are shown in Figure 4a. The effect of a more complex MJSC structure

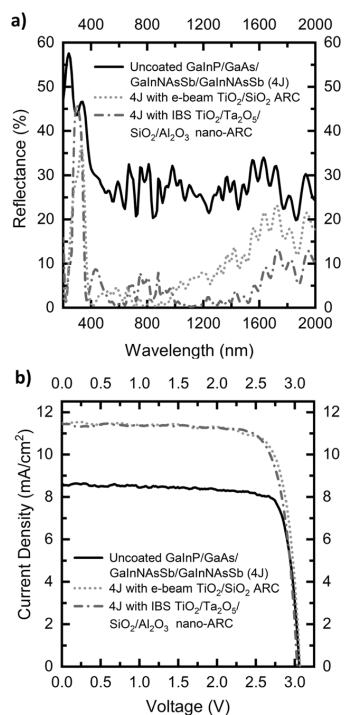


Figure 4. (a) URA-measured reflectance for an uncoated GaInP/GaAs/GaInNAsSb/GaInNAsSb solar cell (4J), with the conventional e-beam double-layer ARC and with the nano-ARC. (b) Measured LIV under AM1.5D (1000 W/m^2) for the 4J solar cells without a coating, with the e-beam double-layer ARC, and with the nano-ARC.

with additional junctions can be seen in the number of interference fringes in the reflectance measured from the bare MJSC. This complexity makes it challenging to design a

Table 3. Calculated Current Densities for Single-Junction GaInP Solar Cells with Compared ARCs Derived from the Ideal Case ($I_{QE} = 1$; $EQE = 1 - R$) and with Measured EQEs at Normal Incidence^a

J_{SC} (mA/cm ²)	uncoated	e-Beam TiO ₂ /SiO ₂	IBS TiO ₂ /Ta ₂ O ₅ /SiO ₂ /Al ₂ O ₃ nano-ARC	R = 0%
AM0/ideal	16.8	22.7	23.1	23.7
AM1.5D/ideal	11.2	15.2	15.4	15.6
AM0/EQE	10.9	14.6	14.6	
AM1.5D/EQE	8.1	10.8	10.8	

^aThe calculations use 1000 W/m^2 for current densities calculated with measured EQE under AM1.5D.

Table 4. Calculated Current Densities from the R_{AVE} and IQE = 1 for the ARC-Coated MJSCs Presented in Different Subcell Operation Bandwidths of the 4J and in the Remaining Bandwidth that Could be Utilized with $E_g \sim 0.7$ eV Subcell

J_{SC} (mA/cm ²)	bandwidth (nm)		uncoated	e-Beam TiO ₂ /SiO ₂	IBS TiO ₂ /Ta ₂ O ₅ /SiO ₂ /Al ₂ O ₃ nano-ARC	R = 0%
GaInP	280–650	AM0	15.7	20.9	20.9	22.0
		AM1.5D	10.4	13.8	13.8	14.3
GaAs	650–880	AM0	12.5	17.0	16.4	17.2
		AM1.5D	10.4	14.1	13.6	14.3
GaInNAsSb (1)	880–1030	AM0	6.7	9.1	9.0	9.3
		AM1.5D	4.8	6.6	6.5	6.7
GaInNAsSb (2)	1030–1380	AM0	11.9	15.8	16.5	16.7
		AM1.5D	8.7	10.9	11.5	11.6
5th junction	1380–1800	AM0	9.6	11.3	12.6	13.4
		AM1.5D	6.2	7.2	8.2	8.7

balanced broadband ARC to spectrally fit the subcell current-matching requirements,^{6,33} as the average reflectance plays a smaller role than the subcell bandwidths or the MJSC overall design. Therefore, the nano-ARC structure was kept the same as for the GaInP SC, to give more comparable results.

The overall reflectance of the nano-ARC is lower than that of the planar ARC, especially at wavelengths above 1000 nm. However, the performance of the nano-ARC does not look optimal at the GaInP and GaAs bandwidths as there are several >5% interference peaks. In a case of either of the top subcells being slightly too thin and having such a high reflectance at its bandwidth, the possibility of the top cell becoming the current-limiting junction in the structure increases. To better evaluate the effects of the ARCs on the MJSC, the subcell current densities were calculated with the measured reflectance values and ideal IQE at their operation bandwidths, which are shown in Table 4.

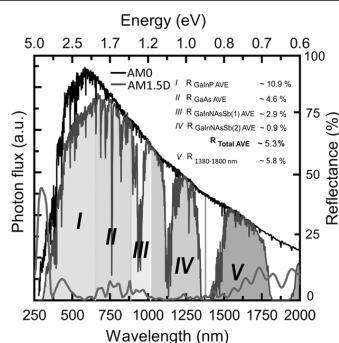
The values in Table 4 show that the nano-ARC provides a larger current density, due to the better average reflectance than the planar ARC, only for the bottom dilute nitride junction. The reflectance of other bandwidths is of a similar scale between the nano-ARC and the planar reference, as the calculated current densities indicate, but for GaInP and GaAs junctions, it is too high and in need of optimization. This can also be seen in Table 5 as LIV values are slightly lower for the nano-ARC-coated 4J than the planar counterpart.

Table 5. Measured LIV Characteristics as Conversion Efficiency η , Open-Circuit Voltage V_{OC} , Short-Circuit Current Density J_{SC} , and Fill Factor FF under AM1.5D (1000 W/m²) for the 4J MJSCs as Bare, with the Planar e-Beam ARC and with the Nano-ARC

	uncoated	e-Beam TiO ₂ /SiO ₂	IBS TiO ₂ /Ta ₂ O ₅ /SiO ₂ /Al ₂ O ₃ nano-ARC
η (%)	21.2	27.6	27.4
V_{OC} (V)	3.1	3.1	3.0
J_{SC} (mA/cm ²)	8.6	11.5	11.4
FF (%)	81.0	78.4	79.2

Despite the nonoptimal subcell reflectance, the nano-ARC-coated MJSC is still a functional device and no significant difference, given the statistical variations of individual cells, the limited number of samples, and the unideal spectrum of the simulator, in the electrical performance compared to the planar-coated MJSC can be observed, as is shown in Figure 4b. This would suggest that the method is suitable for MJSC ARC applications.

The 4J GaInP/GaAs/GaInNAsSb/GaInNAsSb MJSC used in the comparison utilizes photons at the wavelengths of 280–1380 nm, which still leaves a substantial number of photons available at a bandwidth of 1380–1800 nm, as illustrated in Figure 5. The average reflectance of the nano-ARC in this fifth bandwidth is as low as 5.8%, which is 10 percentage points less than the average reflectance of the planar ARC.

**Figure 5.** AM0 and AM1.5D³⁰ spectra alongside with the measured reflectance of the nano-ARC-coated 4J GaInP/GaAs/GaInNAsSb/GaInNAsSb divided in the bandwidth of the subcells and in the bandwidth of a potential 5th junction subcell ($E_g \sim 0.7$ eV). $R_{\text{Total AVE}}$ shows the calculated average over a 4J bandwidth of 280–1380 nm.

With the nano-ARC, a great portion of the photons at a bandwidth of 1380–1800 nm could be utilized and at AM0 that corresponds to a current density of ~ 12.6 mA/cm². This is slightly lower than the current densities of the other junctions, so having an additional 0.7 eV subcell, i.e., third GaInNAsSb,³⁴ would require either altering the subcell bandgaps of the current design or adding a topmost junction, such as AlGaInP,³⁵ to provide nearly current-matched five or six junction SCs for space applications.

The limitations of the nano-ARC for the used MJSC subcell configuration can be overcome with structural optimization of the Al₂O₃ nanostructure by tuning the DIW process parameters, as done by Yin et al.²⁴ and by altering the planar layer thicknesses in the multilayer configuration. The tested nanostructure was not spectrally optimized, as mainly the suitability of the method for a real MJSC device was under inspection. Our results show that the nano-ARC works also for MJSCs and there are no significant additional losses involved due to the ARC fabrication process.

4. CONCLUSIONS


A comparison between a nanostructured alumina multilayer ARC and a conventional planar double-layer ARC was done on a single-junction GaInP SC and 4J MJSC to assess the possible improvements related to the use of surface texturing when applied to high-efficiency MJSCs. The 1J solar cell was used for assessing the angle-dependent characteristics of the nanostructured coating, while the realistic broadband operation for MJSCs is validated using the 4J SC.

On top of the GaInP SCs, the measured reflectance over a broadband spectrum shows that for longer wavelengths, the nano-ARC performs several percentage points better than the planar ARC and the total average reflectance from 280 to 1380 nm is 2.7 and 5.5% for the nano-ARC and the planar ARC, respectively. At shorter wavelengths, the reflectance of the ARCs is of a similar scale, but due to the inward scattering of the nanotextured surface, the amount of diffused light from oblique angles is larger for the nano-ARC. This is shown in the EQE results, where the GaInP SC with the nano-ARC practically retains the same EQE level for the incident angles from 0° to 60°, whereas there is a clear drop for the EQE of the GaInP SC with the planar ARC at the larger incident angles. Better diffusion properties of the nano-ARC near the ultraviolet bandwidth and low reflectance at the infrared region point to possible performance improvements for MJSCs as well.

To address the suitability and the actual broadband operation of the nanostructured ARC on an MJSC, the same coatings were also deposited on the MBE-grown lattice-matched 4-junction GaInP/GaAs/GaInNAsSb/GaInNAsSb MJSCs. At this point, no further optimization of the coating structure was done. The LIV measurements showed that there are no evident losses caused by the nano-ARC process for the MJSC when compared to the planar coating method. The performance with the nano-ARC is adequate, but closer examination in the subcell bandwidths indicates that there is still room for improvement. In fact, the reflectance is slightly increased for all but the bottom subcell, when compared to the planar double-layer ARC. The total average reflectance over the region of operation of the MJSC is lower for the nanostructured ARC, but as the current matching limits the operation of the whole stack by the least current-producing cell, the total gain is smaller than that with the double-layer ARC. However, we believe that these shortcomings can be overcome with structural and process optimization of the nano-ARC and aim to further improve the coating performance. Also, mechanical and long-term environmental stability needs to be evaluated. As the method is lithography-free and simple, we expect to see further utilization of the nano-ARC in future MJSC architectures.

■ AUTHOR INFORMATION


Corresponding Author


Jarno Reuna – Optoelectronics Research Centre, Physics Unit, Faculty of Engineering and Natural Sciences, Tampere University, FI-33014 Tampere, Finland;  orcid.org/0000-0003-0814-1740; Email: jarno.reuna@tuni.fi

Authors

Arttu Hietalahti – Optoelectronics Research Centre, Physics Unit, Faculty of Engineering and Natural Sciences, Tampere University, FI-33014 Tampere, Finland

Arto Aho – Optoelectronics Research Centre, Physics Unit, Faculty of Engineering and Natural Sciences, Tampere University, FI-33014 Tampere, Finland

Riku Isoaho – Optoelectronics Research Centre, Physics Unit, Faculty of Engineering and Natural Sciences, Tampere University, FI-33014 Tampere, Finland;  orcid.org/0000-0002-0582-3853

Timo Aho – Optoelectronics Research Centre, Physics Unit, Faculty of Engineering and Natural Sciences, Tampere University, FI-33014 Tampere, Finland;  orcid.org/0000-0001-5020-1415

Marianna Vuorinen – Optoelectronics Research Centre, Physics Unit, Faculty of Engineering and Natural Sciences, Tampere University, FI-33014 Tampere, Finland

Antti Tukiainen – Optoelectronics Research Centre, Physics Unit, Faculty of Engineering and Natural Sciences, Tampere University, FI-33014 Tampere, Finland

Elina Anttola – Optoelectronics Research Centre, Physics Unit, Faculty of Engineering and Natural Sciences, Tampere University, FI-33014 Tampere, Finland

Mircea Guina – Optoelectronics Research Centre, Physics Unit, Faculty of Engineering and Natural Sciences, Tampere University, FI-33014 Tampere, Finland

Complete contact information is available at: <https://pubs.acs.org/10.1021/acsaem.2c00133>

Notes

The authors declare no competing financial interest.

■ ACKNOWLEDGMENTS

This work made use of Tampere Microscopy Center facilities at Tampere University. The financial support provided by the European Research Council (ERC AdG AMETIST, #695116) is acknowledged. The work is also part of the Academy of Finland Flagship Program PREIN #320168.

■ REFERENCES

- (1) Geisz, J. F.; France, R. M.; Schulte, K. L.; Steiner, M. A.; Norman, A. G.; Guthrey, H. L.; Young, M. R.; Song, T.; Moriarty, T. Six-Junction III–V Solar Cells with 47.1% Conversion Efficiency under 143 Suns Concentration. *Nat. Energy* **2020**, *5*, 326–335.
- (2) Green, M. A.; Dunlop, E. D.; Hohl-Ebinger, J.; Yoshita, M.; Kopidakis, N.; Hao, X. Solar Cell Efficiency Tables (Version 58). *Progr. Photovolt.: Res. Appl.* **2021**, *29*, 657–667.
- (3) Henry, C. H. Limiting Efficiencies of Ideal Single and Multiple Energy Gap Terrestrial Solar Cells. *J. Appl. Phys.* **1980**, *51*, 4494–4500.
- (4) Warmann, E. C.; Leite, M. S.; Atwater, H. A. Photovoltaic Efficiencies in Lattice-Matched III–V Multijunction Solar Cells with Unconventional Lattice Parameters. In *2011 37th IEEE Photovoltaic Specialists Conference (PVSC)*; IEEE, 2011; pp 570–574. DOI: 10.1109/PVSC.2011.6186019.
- (5) Polman, A.; Atwater, H. A. Photonic Design Principles for Ultrahigh-Efficiency Photovoltaics. *Nat. Mater.* **2012**, *11*, 174–177.
- (6) Aiken, D. J. Antireflection Coating Design for Series Interconnected Multi-Junction Solar Cells. *Progr. Photovolt.: Res. Appl.* **2000**, *8*, 563–570.
- (7) Aho, A.; Isoaho, R.; Hytönen, L.; Aho, T.; Raappana, M.; Polojärvi, V.; Tukiainen, A.; Reuna, J.; Mäkelä, S.; Guina, M. Lattice-Matched Four-Junction Tandem Solar Cell Including Two Dilute Nitride Bottom Junctions. *Progr. Photovolt.: Res. Appl.* **2019**, *27*, 299–305.
- (8) Musalinov, S. B.; Anzulevich, A. P.; Bychkov, I. V.; Gudovskikh, A. S.; Shvarts, M. Z. Influence of Double- and Triple-Layer

Antireflection Coatings on the Formation of Photocurrents in Multijunction III–V Solar Cells. *Semiconductors* **2017**, *51*, 88–92.

(9) Perl, E. E.; McMahon, W. E.; Bowers, J. E.; Friedman, D. J. Design of Antireflective Nanostructures and Optical Coatings for Next-Generation Multijunction Photovoltaic Devices. *Opt. Express* **2014**, *22*, A1243.

(10) King, R. R.; Colter, P. C.; Joslin, D. E.; Edmondson, K. M.; Krut, D. D.; Karam, N. H.; Kurtz, S. *High-Voltage, Low-Current GaInP/GaInP/GaAs/GaInNAs/Ge Solar Cells*; IEEE, 2002.

(11) Ochoa, M.; García, I.; Lombardero, I.; Ayllón, L.; Rey-Stolle, I.; Algora, C.; Johnson, A.; Davies, J. I.; Tan, K. H.; Loke, W. K.; Wicaksono, S.; Yoon, S. F.; Ochoa-Martínez, E.; Gabás, M. Modelling of Lattice Matched Dilute Nitride 4-Junction Concentrator Solar Cells on Ge Substrates. *AIP Conf. Proc.* **2016**, *1766*, No. 4962101.

(12) King, R. R.; Law, D. C.; Edmondson, K. M.; Fetzer, C. M.; Kinsey, G. S.; Yoon, H.; Sherif, R. A.; Karam, N. H. 40% Efficient Metamorphic GaInP/GaInAs/Ge Multijunction Solar Cells. *Appl. Phys. Lett.* **2007**, *90*, 183516.

(13) Sun, C.-H.; Ho, B. J.; Jiang, B.; Jiang, P. Biomimetic Subwavelength Antireflective Gratings on GaAs. *Opt. Lett.* **2008**, *33*, 2224.

(14) Leem, J. W.; Su, Y. J.; Jun, D. H.; Heo, J.; Park, W. K. Efficiency Improvement of III-V GaAs Solar Cells Using Biomimetic TiO₂ Subwavelength Structures with Wide-Angle and Broadband Antireflection Properties. *Sol. Energy Mater. Sol. Cells* **2014**, *127*, 43–49.

(15) Liang, D.; Kang, Y.; Huo, Y.; Chen, Y.; Cui, Y.; Harris, J. S. High-Efficiency Nanostructured Window GaAs Solar Cells. *Nano Lett.* **2013**, *13*, 4850–4856.

(16) Tommila, J.; Aho, A.; Tukiainen, A.; Polojärvi, V.; Salmi, J.; Niemi, T.; Guina, M. Moth-Eye Antireflection Coating Fabricated by Nanoimprint Lithography on 1 EV Dilute Nitride Solar Cell. *Prog. Photovolt.: Res. Appl.* **2013**, *21*, 1158–1162.

(17) Tommila, J.; Polojärvi, V.; Aho, A.; Tukiainen, A.; Viheriälä, J.; Salmi, J.; Schramm, A.; Kontio, J. M.; Turtiainen, A.; Niemi, T. Nanostructured Broadband Antireflection Coatings on AlInP Fabricated by Nanoimprint Lithography. *Sol. Energy Mater. Sol. Cells* **2010**, *94*, 1845–1848.

(18) Zhu, J.; Hsu, C. M.; Yu, Z.; Fan, S.; Cui, Y. Nanodome Solar Cells with Efficient Light Management and Self-Cleaning. *Nano Lett.* **2010**, *10*, 1979–1984.

(19) Perl, E. E.; Lin, C. T.; McMahon, W. E.; Friedman, D. J.; Bowers, J. E. Ultrabroadband and Wide-Angle Hybrid Antireflection Coatings with Nanostructures. *IEEE J. Photovolt.* **2014**, *4*, 962–967.

(20) Zhou, W.; Tao, M.; Chen, L.; Yang, H. Microstructured Surface Design for Omnidirectional Antireflection Coatings on Solar Cells. *J. Appl. Phys.* **2007**, *102*, 103105.

(21) Reuna, J.; Aho, A.; Isoaho, R.; Raappana, M.; Aho, T.; Anttola, E.; Hietalahti, A.; Tukiainen, A.; Guina, M. Use of Nanostructured Alumina Thin Films in Multilayer Anti-Reflective Coatings. *Nanotechnology* **2021**, *32*, 215602.

(22) Kauppinen, C.; Isakov, K.; Sopanen, M. Grass-like Alumina with Low Refractive Index for Scalable, Broadband, Omnidirectional Antireflection Coatings on Glass Using Atomic Layer Deposition. *ACS Appl. Mater. Interfaces* **2017**, *9*, 15038–15043.

(23) Dokmai, V.; Methaapanon, R.; Pavarajarn, V. Corrosion of Amorphous Alumina in Deionized Water under Mild Condition. *Appl. Surf. Sci.* **2019**, *499*, No. 143906.

(24) Yin, C.; Zhu, M.; Zeng, T.; Sun, J.; Zhang, R.; Zhao, J.; Wang, L.; Shao, J. Al₂O₃ Anti-Reflection Coatings with Graded-Refractive Index Profile for Laser Applications. *Opt. Mater. Express* **2021**, *11*, 875.

(25) Isakov, K.; Kauppinen, C.; Franssila, S.; Lipsanen, H. Superhydrophobic Antireflection Coating on Glass Using Grass-like Alumina and Fluoropolymer. *ACS Appl. Mater. Interfaces* **2020**, *12*, 49957–49962.

(26) Domínguez, C.; García-Linares, P. Characterization of Multijunction Concentrator Solar Cells. In *High Concentrator Photovoltaics: Fundamentals, Engineering and Power Plants*; Pérez-

Higuera, P.; Fernández, E. F., Eds.; Springer International Publishing: Cham, 2015; pp 39–84.

(27) García-Linares, P.; Domínguez, C.; Voarino, P.; Besson, P.; Baudrit, M. Advances on Multijunction Solar Cell Characterization Aimed at the Optimization of Real Concentrator Performance. *AIP Conf. Proc.* **2015**, *2014*, 110–113.

(28) Aho, A.; Tommila, J.; Tukiainen, A.; Polojärvi, V.; Niemi, T.; Guina, M. Moth Eye Antireflection Coated GaInP/GaAs/GaInNAs Solar Cell. *AIP Conf. Proc.* **2014**, *1616*, 33–36.

(29) May, M. M.; Lackner, D.; Ohlmann, J.; Dimroth, F.; van de Krol, R.; Hannappel, T.; Schwarzburg, K. On the Benchmarking of Multi-Junction Photoelectrochemical Fuel Generating Devices. *Sustainable Energy Fuels* **2017**, *1*, 492–503.

(30) ASTM G173–03 Reference Spectra <http://redc.nrel.gov/solar/spectra/am1.5/astmg173/astmg173.html>.

(31) Kirk, A. P. High Efficacy Thinned Four-Junction Solar Cell. *Semicond. Sci. Technol.* **2011**, *26*, No. 125013.

(32) Zhang, J.-C.; Xiong, L.-M.; Fang, M.; He, H.-B. Wide-Angle and Broadband Graded-Refractive-Index Antireflection Coatings. *Chin. Phys. B* **2013**, *22*, No. 044201.

(33) Guter, W.; Schöne, J.; Philipps, S. P.; Steiner, M.; Siefert, G.; Wekkeli, A.; Welser, E.; Oliva, E.; Bett, A. W.; Dimroth, F. Current-Matched Triple-Junction Solar Cell Reaching 41.1% Conversion Efficiency under Concentrated Sunlight. *Appl. Phys. Lett.* **2009**, *94*, 8–11.

(34) Aho, A.; Isoaho, R.; Raappana, M.; Aho, T.; Anttola, E.; Lyytikäinen, J.; Hietalahti, A.; Polojärvi, V.; Tukiainen, A.; Reuna, J.; Peltomaa, L.; Guina, M. Wide Spectral Coverage (0.7–2.2 EV) Lattice-Matched Multijunction Solar Cells Based on AlGaInP, AlGaAs and GaInNAsSb Materials. *Prog. Photovoltaics* **2021**, *29*, 869–875.

(35) King, R.; Fetzer, C.; Law, D.; Edmondson, K.; Yoon, H.; Kinsey, G.; Krut, D.; Ermer, J.; Hebert, P.; Cavicchi, B.; Karam, N. Advanced III-V Multijunction Cells for Space. In *IEEE 4th World Conference on Photovoltaic Energy Conference*; IEEE, 2006; Vol. 2, pp 1757–1762.

PUBLICATION

5

Ice Resistance of Hydrophobic Fluoropolymerized Nanostructured Alumina Films for Antireflective Coatings

J. Reuna, R. Kanter, N. Kandelin, K. Kiuru, H. Koivuluoto and M. Guina

(Submitted to *Nano Express*, focused issue “Nano-Enabled Anti-Icing”)

<https://doi.org/XXX>

Publication reprinted with the permission of the copyright holders.

